TUNING REACTION KINETICS AT THE CATALYST/ELECTROLYTE INTERFACE: A NEW DESIGN SPACE IN ELECTROCATALYSIS

by
Ellen E. Benn

A dissertation submitted to Johns Hopkins University in conformity with the requirements for the degree of Doctor of Philosophy

Baltimore, Maryland

September 2016

Abstract

Dealloying is a process that selectively dissolves one component from an alloy, which due to competing kinetics of dissolution and surface diffusion can lead to nanoporosity evolution with a characteristic ligament size. These materials have been studied in a variety of fields, but in this dissertation we focus specifically on the applications in electrocatalysis.

Nanoporous Ni-Pt (np-NiPt) is of use as a catalyst for the oxygen reduction reaction, the limiting reaction occurring at the cathode of a hydrogen fuel cell, due to its high surface area-to-volume ratio and ideal structural/compositional configuration. However, much of the catalyst's surface area is not electrochemically active due to transport limitation into the pores. Building off of prior research that employed an ionic liquid incorporated into the porosity to bias reactants to the surface, we determined the key properties of this secondary phase to improve the composite catalyst's overall activity, with specific interest on the transport phenomena occurring between the electrolyte/ionic liquid/catalyst surface.

Turning our attention to the role of proton transport in acidic electrolytes, we explored oxygen reduction over np-NiPt under the unusual conditions of protons being diffusion limited in the reaction. Because this is typically performed in highly acidic environments, this scenario is uncommon; however, it allows for analysis of transport kinetics with the ability to easily change reactant concentrations simply by varying pH. We can also control the reaction dominating at the geometric surface of the catalyst

versus that within the pores due to strong concentration gradients and relatively slow diffusion kinetics. Under these conditions we found that we could run the oxygen reduction reaction under extremely high overpotentials, suppressing the hydrogen evolution side reaction. This general concept may be extended to the electoreduction of other small molecules, where competition from side reactions such as hydrogen evolution become a major concern.

Lastly, we have developed a sequential electrode flow reactor in which we have the ability to control the reactant concentrations and independently manipulate the fluxes of reactants by applying set potentials at each electrode. Ultimately this design is intended for use with the electrochemical synthesis of ammonia, a challenging reaction due to competing water dissociation and hydrogen evolution. In this study, we oxidize and evolve hydrogen at successive electrodes in aqueous solutions and ionic liquids as a first step in validating our concept and design.

Advisor: Dr. Jonah Erlebacher

Readers: Dr. Timothy Mueller

Dr. Kenneth Karlin

Dr. Susanna Thon

Dr. Chao Wang

Acknowledgements

It would have been impossible to complete my PhD at Johns Hopkins University without the support and assistance of my advisors, fellow graduate students, friends and family. For that, I am incredibly grateful.

First and foremost, I'd like to acknowledge my advisor, Dr. Jonah Erlebacher. Your passion and love for science is contagious, and the value of your advice and experience is beyond measure. I cannot thank you enough for the supportive environment to allow our creativity and ideas to flourish. I approach problems with more critical thought, write more proficiently, and never forget to have fun in lab, thanks to your guidance and instruction.

My fellow graduate students deserve my sincerest gratitude, particular those past and present within my lab group: Joshua Snyder, Ian McCue, Bernard Gaskey, Hugo Uvegi, Gina Greenidge, and Luthfe Siddique. Thank you for all of your assistance and knowledge in the lab, as well as the entertaining discussions outside of it, however un-science related the tangents might become.

I would also like to thank the staff in the department: Jeanine Majewski, Ada Simari, Bryan Crawford, Amanda Gursky, Alex van Horn, and Chris Witczak, who managed to solve every problem thrown their way and seem happy to do so. There are numerous faculty members that have helped to make this time productive and rewarding, specifically those within the Materials Science and Engineering department. Thank you.

My stepmother's, Karen, constant pep talks and my brother's, James, never-ending support, alongside my close friends that kept me sane for the past few years, truly made this accomplishment possible. My fiancé, Brandon, genuinely deserves special recognition for all of his unwavering support, love, and understanding that has allowed me to focus on my ambitions without hesitation. I cannot thank you enough and I love you all.

Table of Contents

List of Figures

List of Tables

Chapter 1. Introduction

1.1 Motivation

The field of dealloying to form nanoporous metals has rapidly expanded in recent years, with focus on different aspects such as mechanisms and fundamentals, creating new porous metals, and studying properties for real world applications. With such high interfacial area and facile formation, nanoporous materials have found purposes in fields ranging from capacitors and sensing materials, to radiation damage-tolerant materials.

A clear application for nanoporous metals is their use in catalysis. Dealloying provides an easy, quick process for fabricating nanoscale materials possessing high surface area-to-volume ratios with a minimal waste of precious metals via a process that can readily be scaled up. It is the goal of the work presented here to focus on transport kinetics, specifically delving into the matter to gain a fundamental understanding and consequently engineer superior electrocatalysts. This dissertation is structured in the following manner:

The first couple of chapters will focus on using nanoporous NiPt as a catalyst for the oxygen reduction reaction (ORR), the limiting reaction in proton exchange membrane fuel cell catalysis. In Chapter 2, we will focus on ionic liquid impregnated nanoporous metals composite catalyst systems, deducing the best properties to increase activity for use with fuel cells in automotive applications. Previous research has shown adding a

material with a higher oxygen solubility to a porous catalyst boosts the aggregate composite's overall activity. A more comprehensive study we completed confirmed this, but also determined the water solubility in the ionic liquid played a crucial role in determining the kinetics of the reaction.

Chapter 3 deviates from practical applications slightly while still analyzing ORR, but now using the reaction as a model system to understand the importance of proton transport to the nanoporous catalyst. We find we are able to form a diffusion selective catalyst, where we can suppress side reactions and tune the mechanism by which we can reduce oxygen simply by varying the electrolyte and pH of the solution.

In Chapter 4, we are no longer focused on ORR kinetics, but using the previous knowledge of proton transport and ionic liquid properties. We discuss a novel flow system developed for the electrochemical synthesis of ammonia, engineered and tested using subsequent hydrogen oxidation/hydrogen evolution reactions, where we are able to control the reactant flows by electrochemically creating a source of protons as needed.

The remainder of this introductory chapter will focus on dealloying, its mechanisms, and the resulting structures; the use of nanoporous metals as successful catalysts; before summarizing the fundamental aspects of fuel cells and the electrochemical reactions necessary. Lastly, we will discuss typical oxygen reduction measurements and results, summarizing further advancements on catalytic activity being made with ionic liquid impregnation.

1.2 Dealloying

Dealloying is defined as the dissolution of a less noble component of an alloy while the more noble metal diffuses along the surface, rearranging to form a porous network. The structure exhibits bicontinuous open porosity with a ligament/pore length as small as several nanometers. By controlling the relative rate of dissolution compared to the rate of re-organization during processing, nanoporosity evolution in dealloyed materials as a general principle can be formed with a tunable length scale between of order 10 nm to 10 microns. An image of the characteristic morphology is shown in Figure 1.1 for nanoporous Au (np-Au) formed from AuAg precursor alloys.

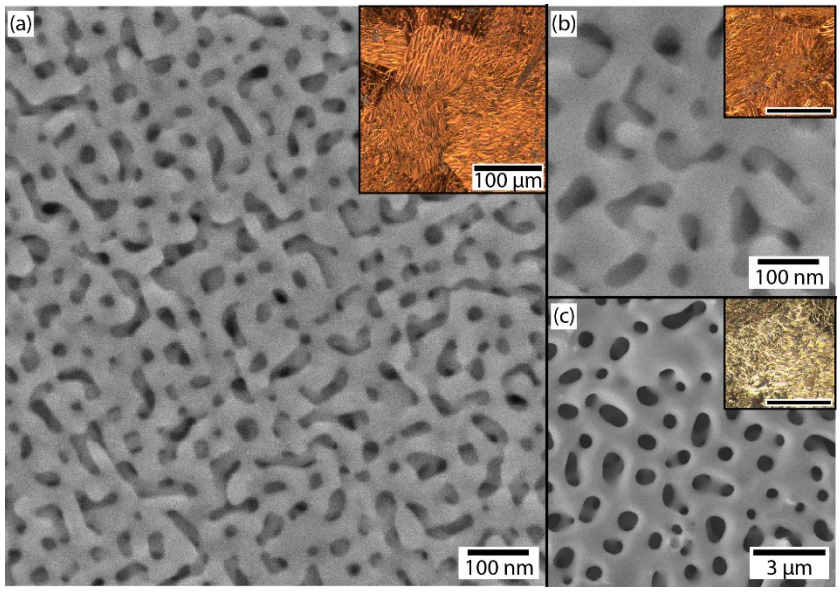

Figure 1.1. Scanning electron (SEM) and optical micrographs *(inset)* of nanoporous gold (np-Au) formed through dealloying via free corrosion of a $Ag_{65}Au_{35}$ precursor alloy in

concentrated nitric acid. Initially, feature size is ~ 30 nm after dealloying for 24 hours (a), before coarsening to ~60nm after an additional several days in nitric acid (b). After exposure to heating in air at 800C, the pores coarsen to several microns (c). *(Adapted from Ref [1])*

The working model for porosity evolution via dealloying was introduced by Erlebacher and Seshadri[2] for the prototypical system of Au-Ag alloys, shown schematically in Figure 1.2. To summarize, above a certain potential threshold referred to as the critical potential, the less noble atoms (Ag) can be dissolved and as such are easily removed from low coordination step edges. Meanwhile the surface becomes passivated with the remaining more noble species, in this case Au[3], until the removal of a Ag atom from a terrace or similar high-coordination site, representing the rate-determining step. As this vacancy grows laterally, the alloy is susceptible to layer by layer dissolution of Ag, with the remaining Au atoms rearranging on the surface to passivate the low-coordination sites on step edges. If there is not enough Au to fully cover all these edges, the dealloying process will result in undercutting and bifurcation of ligaments as porosity evolution proceeds. As an end result, we are left with a porous structure that has a Au rich skin passivating a Ag rich ligament core. Alternatively, if there is a sufficient amount of Au to fully passivate and cover the surface, the process would end after merely surface roughening, preventing any porosity from developing. Conversely, if there is an abundance of Ag, the resulting structure will collapse on itself without a sufficient proportion of Au atoms to support porosity formation. This composition bound of dealloyable alloys is known as the parting limit.

Over time, dealloyed materials coarsen, exposing residual Ag atoms that are subsequently dissolved. This increases the length scale associated with the pores and

ligaments in addition to leaving a final structure with significantly less residual Ag. This can be achieved by applying a potential or by increasing the temperature to which the dealloyed material is exposed, thus increasing the rate of surface diffusion. While the initial length scale is on order of several nanometers, with coarsening by either chemical or thermal means, can result in pores several microns across, illustrated in Figure 1.1.

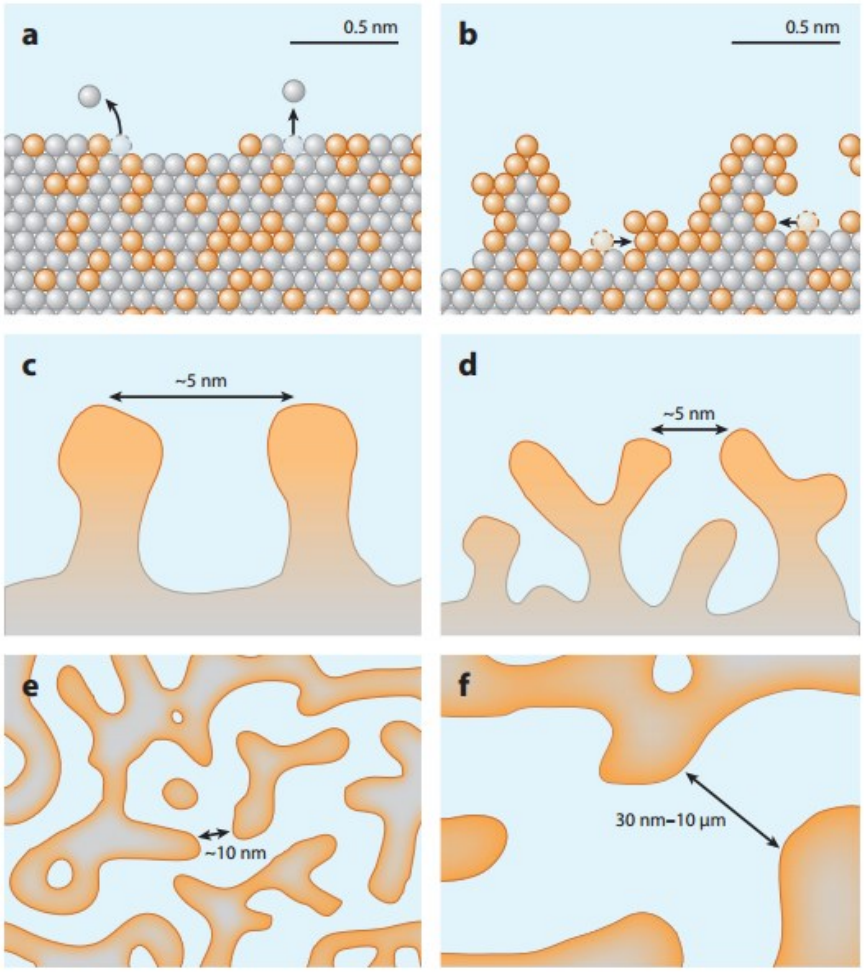

Figure 1.2. Schematic representation of porosity evolution during dealloying *(adapted from Ref [1]),* with Ag represented in gray and Au in orange. (a) Initial Ag atoms are removed from terrace sites as the rate-limiting step, which continues layer by layer (b). Without sufficient Au atoms to fully passivate low coordination sites, dealloying continues, resulting in undercutting (c) and bifurcation of ligaments (d). The resulting structure exhibits bicontinuous porosity (e) with Au-rich surfaces covering Ag-rich interiors (e), until ultimately coarsening to larger length scales (f).

There are several different processing techniques to yield nanoporous metals, the most common via free corrosion or electrochemical dealloying performed in an electrolyte. Both are similar in the fact that the starting alloy must be suitable, i.e. there must be a great enough distance in electrochemical reduction potentials (on order of a few hundred millivolts) to allow one component to dissolve but not the other[3].

These requirements of correct parting limit and difference in reduction potentials, coupled with the necessary rates of surface diffusion essential for surface reorganization seen in nanoporous metals, limit the number of porous metals that can be formed via electrochemical dealloying, exclusive to primarily noble metals. Adapting these same ideas of electrochemical processing, Kato et al.[4] use a liquid metal bath rather than using an aqueous electrolyte as the dealloying medium. In short, a parent alloy (where the components form a solid solution) is dipped into a molten metal, where one of the alloy's components is insoluble while the other readily dissolves. This acts in a similar fashion to the schematic representation in Figure 1.2, except it occurs at much higher temperatures and therefore increases the kinetics, making a whole range of metals now available for dealloying. Of particular interest is transition metals, specifically for their use as high surface area catalysts[5].

1.3 Applications for Dealloyed Materials in Catalysis

By creating dealloyed bicontinuous networks, the surface area greatly increases, making dealloyed metals promising as catalyst materials. In particular, they are especially useful as precious metal-based catalysts where optimizing surface area to volume is economically advantageous. Additionally, the continuity of the porosity means every surface of the catalyst is in electrical contact, unlike many nanoparticle-based methods where surface area is increased, but the use of support (i.e. Pt nanoparticles on carbon) means not every particle will be used if it does not adhere well to the support material[6].

Nanoporous-Au (np-Au) has been studied extensively for its use in catalysis of oxidation reactions. This is rather surprising since bulk Au surfaces are rather catalytically inert with the exception of when atomic oxygen adsorbed upon them. However, nanoparticles of Au, as well as np-Au, are remarkably catalytic towards low-temperature CO oxidation, converting poisonous CO to CO_2, a necessary step in the scrubbing of exhaust gases from combustion engines[7–9].

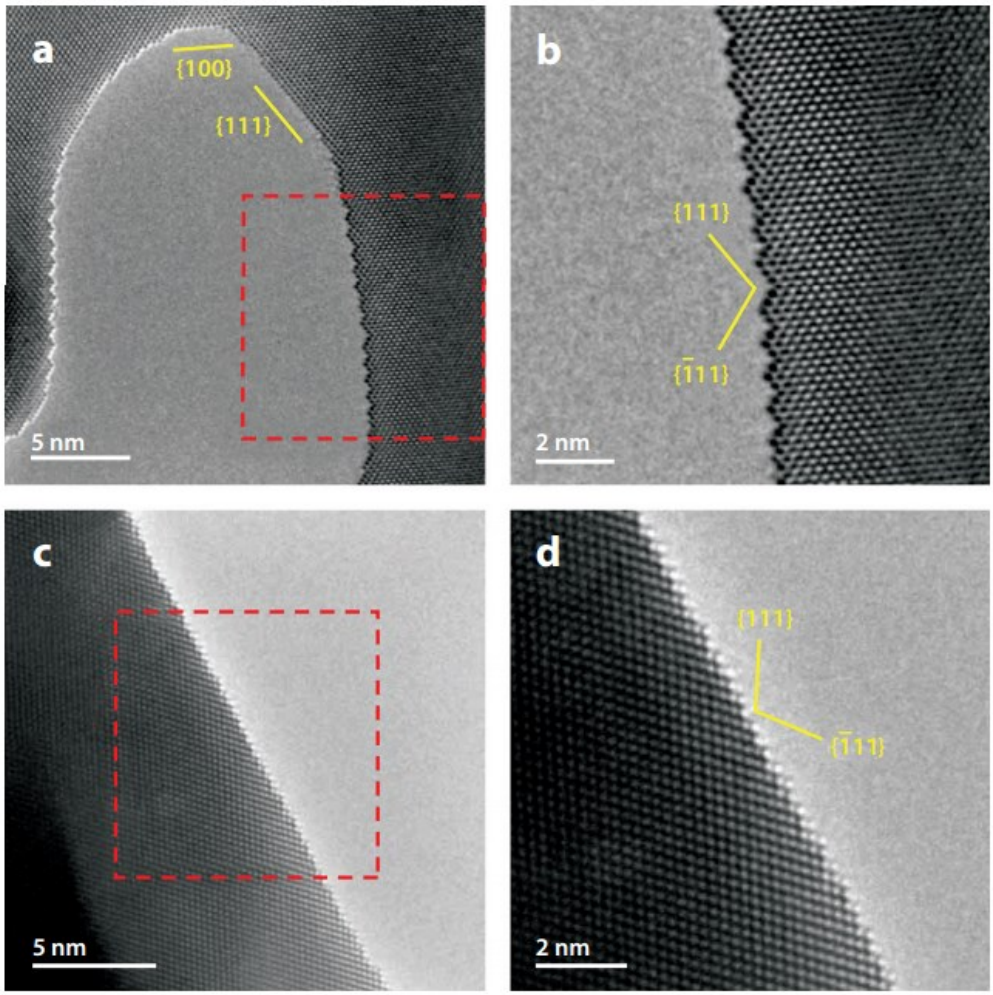

Figure 1. 3. HRTEM images showing details of the surface reconstruction of nanoporous (np)-Au ligaments in the presence of low CO partial pressure. (a) np-Au with 1.2-at% Ag reconstructed into relatively unreactive {111} microfacets. (b) Enlarged selected area of panel a. (c) np-Au with 20-at% Ag does not reconstruct and retains significant activity. (d) Enlarged selected area of panel c. *(Adapted from Ref [10], where additional details are provided.)*

While some residual Ag in the np-Au may explain part of the increased activity, the microstructure clearly is a dominant factor. DFT calculations of Au surfaces suggest that the coordination number of the atom dictates the binding energy of oxygen, a crucial indicator of activity for CO oxidation reactions. Less coordinated atoms, such as the

corners and steps found in a higher proportion in nanoparticles and np-Au, were determined to be more catalytically active[11]. While dealloying, np-Au is geometrically required to rearrange into regions of positive, negative and saddle-point curvature, resulting in an intrinsically high density of low coordination surface sites, similar to the structure of Au nanoparticles, explaining the increase in catalytic activity for oxidation reactions. This is evident looking at environmental atomic-resolution imaging of np-Au, using TEM and HAADF-STEM on samples with ligaments approximately 30 nm in diameter (Figure 1.3). However, the small quantity of residual Ag is crucial to preventing the surface faceting reconstruction that would break the surface into unreactive {111} microfacets, and instead maintaining the active low-coordinated sites[10].

Where oxidation reactions prefer a large density of low-coordinated atoms, many reduction reactions occur on planar, low index surfaces[6,12]. Of particular interest is the reduction of oxygen to water, the cathodic reaction occurring in a hydrogen fuel cell. The highest activity surface for this four-electron reduction is the (111) surface of Pt_3Ni, annealed to produce a Pt skin over a bulk alloy[13], a similar structure to that seen in dealloyed materials. Of particular interest are three systems: Cu-Pt, Co-Pt, and Ni-Pt[14–20], with the research we will be presenting focusing on the latter. Dealloying of NiPt systems with an initial composition of $Ni_{77}Pt_{23}$ leads to high surface area np-NiPt with a residual composition near the ideal Pt_3Ni and a Pt skin on the surface, making the material highly catalytic towards oxygen reduction due to this compositional variation causing strain and ligand effects that reduce the activation barrier for ORR, analogously to nickel platinum nanoparticles [[13,14,21–24]].

In an initial study we made of this material[25], the intrinsic specific activity toward oxygen reduction, benchmarked at 0.9 V vs. RHE, was found on the order of the activities expected for the low-index facets of single crystal Pt_3Ni, suggesting the microstructure is primarily comprised of low-index facets, in agreement with KMC simulations. Yet, the largest engineering challenge we faced was how to translate this material into operational fuel cells so that the full extent of the catalyst is used. This geometric effect might be alleviated in thin film catalysts (such as 3M's nanostructured thin film materials[26]) , or by producing nanoporous nanoparticles, as achieved by a number of groups[27–32], both of which are effective at producing highly mass-active catalysts.

1.4 Fuel Cell Background

The major reason for development of fuel cells is increasing concern over the use of fossil fuels, whose impact on the environment has becoming increasingly apparent. The desire for cleaner, more efficient energy sources has arisen as a result. Simply put, a fuel cell is a device that can convert a chemical reaction into electrical work, rather than heat as a combustion engine operates and hence allows a greater theoretical efficiency than that of the standard Carnot cycle. The basic structure of all fuel cells is the same: two electrodes connected to an external circuit and separated by an electrolyte with a flow to the system that provides the electrodes with fuel, this process is schematically shown in Figure 1.4. While the theoretical efficiency of is higher for fuel cells, there are still limitations and engineering challenges that hinder their performance which include, but not strictly limited to, losses due to mass transport through the cell, thermal losses

associated with energy being released as heat, electrode overpotentials necessary to drive the anode and cathode reactions, and resistances found in the electrolyte.

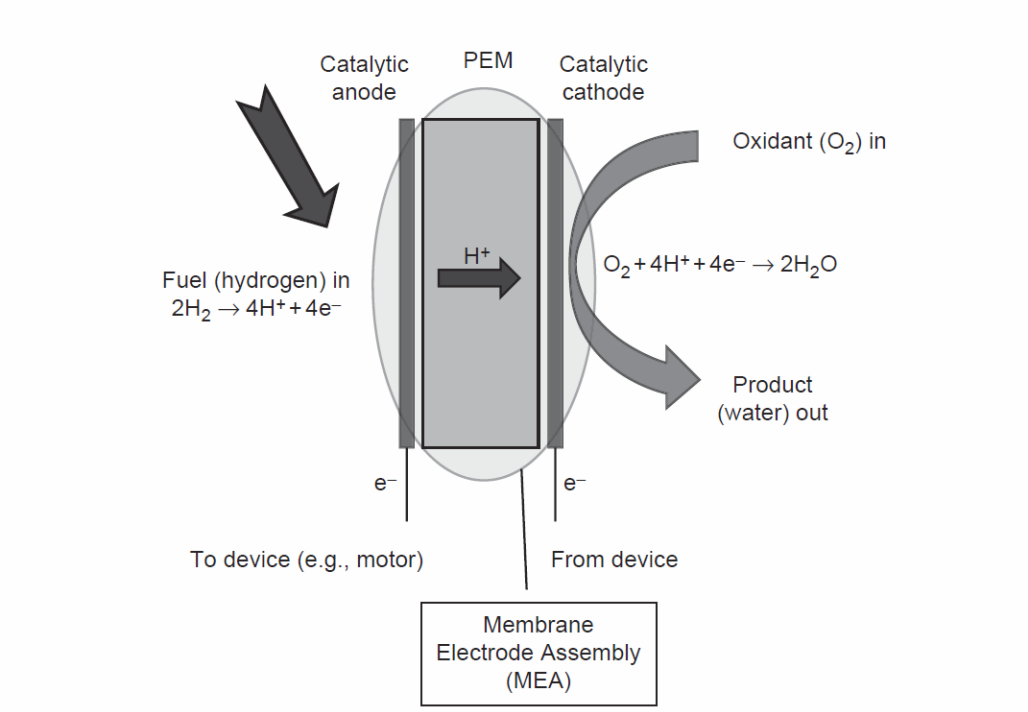

Figure 1.4. Schematic representation of a proton exchange membrane fuel assembly. *(Adapted from Ref [6])*

Fuel cells are often categorized by the type of electrolyte they employ and whether they operate at high or low temperatures. A summary of the main classifications of fuel cells and their properties is listed in Table 1.1. Briefly, they are as follows[33]:

1. *Alkaline Fuel Cell (AFC)* – Exhibits the highest electrical efficiency of all fuel cells currently employed, but only works well with high purity gases, limiting the applications for use and increasing operating costs.

2. *Polymer Electrolyte Fuel Cell (PEMFC)* – This cell uses proton exchange membrane as electrolyte that saw major breakthrough with the use of Nafion, developed by DuPont, which demonstrates a higher stability, conductivity and acidity compared to previous membranes.
3. *Direct Methanol Fuel Cell (DMFC)* – Based off of PEMFC technology, DMFCs use methanol as the fuel rather than hydrogen, skipping the added reforming step so that natural gas or biomass can be fed directly to the fuel cell, while operating at slightly higher temperatures so as to gain higher power densities. However, the methanol oxidation reaction occurring at the anode has relatively slow kinetics compared to hydrogen oxidation with the currently developed catalysts, making DMFCs less effective.
4. *Phosphoric Acid Fuel Cell (PAFC)* – Commercially, this class of fuel cell is the most advanced, primarily for use in power plants, due to its simplicity and stability.
5. *Molten Carbonate Fuel Cell (MCFC)* – Operating at the highest end of the temperature spectrum for the cells mentioned here, MCFCs have the advantage of allowing for internal reforming, as well as using the waste heat with combined cycle power plants. The elevated temperatures drastically improve the ORR kinetics, meaning that non-precious metal-based catalysts have activities that are significant enough for use.
6. *Solid Oxide Fuel Cell (SOFC)* – By using a solid rather than liquid electrolyte as the name implies, SOFCs are more stable and do not face any problems associated with leakage as some other cells experience. However, the largest

drawback is finding materials with sufficient properties to withstand the thermal constraints and thus far has proved challenging.

Table 1.1. Several types of fuel cells currently in use. *(Adapted from Ref [33])*

	Alkaline (AFC)	*Polymer Electrolyte Membrane (PEMFC)*	*Direct Methanol (DMFC)*	*Phosphoric Acid (PAFC)*	*Molten Carbonate (MCFC)*	*Solid Oxide (SOFC)*
Operating temp (˚C)	<100	60-120	60-120	160-220	600-800	800-1000 typically
Uses	Transportation Space Military Energy storage systems			Combined heat & power for stationary power systems	Combined heat & power for stationary power systems Transportation (trains, boats, etc.)	
Anode reaction	$H_2 + 2OH^- \rightarrow 2H_2O + 2e^-$	$H_2 \rightarrow 2H^+ + 2e^-$	$CH_3OH + H_2O \rightarrow CO_2 + 6H^+ + 6e^-$	$H_2 \rightarrow 2H^+ + 2e^-$	$H_2 + CO_3^{2-} \rightarrow H_2O + CO_2 + 2$	$H_2 + O^{2-} \rightarrow H_2O + 2e^-$
Cathode reaction	$1/2O_2 + 2H_2O + 2e^- \rightarrow 2OH^-$	$1/2O_2 + 2H^+ + 2e^- \rightarrow H_2O$	$3/2O_2 + 6H^+ + 6e^- \rightarrow 3H_2O$	$1/2O_2 + 2H^+ + 2e^- \rightarrow H_2O$	$1/2O_2 + CO_2 + 2e^- \rightarrow CO_3^{2-}$	$1/2O_2 + 2e^- \rightarrow O^{2-}$

Of specific interest is the hydrogen/oxygen proton exchange membrane fuel cell (PEMFC). In this method, hydrogen and oxygen are combined to yield water in a highly exothermic reaction. At the anode, hydrogen is supplied as fuel, where it is converted to protons and releases electrons in a process known as the hydrogen oxidation reaction (HOR). These protons travel through the membrane electrode assembly (MEA), while electrons perform work by passing through an external circuit. On the other side of the

MEA, the cathode catalyzes the reaction of oxygen with protons to form water, known as the oxygen reduction reaction (ORR)[6].

Theoretically, one should be able to maintain a voltage of 1.23 V using this device, assuming all reactions are completely reversible. However, as expected, the cell does not run perfectly and some losses are associated with it, a notable challenge involving water management within the cell. In order to increase conductivity, PEMFCs are often filled with water, however this creates a water drag through the cell and allows for back diffusion from the product water generated at the cathode flowing back through the cell. Humidifying the feed gases helps to improve this, but not entirely alleviate the issue[33].

Activation losses also greatly hinder PEMFCs efficiencies. When the cell voltage drops due to irreversibility of the electrode reactions, as seen at high current densities, excess energy is then released as heat rather than electrical work. While the anode contributes to these losses, it is primarily only when substantial amounts of impurities are present, otherwise being considered effectively reversible, requiring very slight overpotentials (less than 50 mV) to drive HOR. It is the cathodic ORR that accounts for the majority of the losses catalytically – low operating temperatures in PEMFCs, coupled with the feed to the cathode being air rather than pure oxygen, require higher loadings of catalyst to improve the reaction kinetics[33].

1.5 Oxygen Reduction Reaction

Since the cathodic oxygen reduction reaction (ORR) is the most inefficient component of hydrogen fuel cells, better catalysts for this reaction are required prior to implementation of this technology. As mentioned, at room temperature the theoretical potential for a PEM fuel cell is 1.23 V, though most catalysts report values closer to ~0.9 V.[34] Some of these losses are due to mass transport limitations that occur due to consumption of fuel at the catalyst surface leading to concentration variations. The largest contributor, however, is the sluggish reaction kinetics of ORR that limit the efficiency of the cell. This means that some of the voltage generated is lost in order to drive the reaction at each electrode. As temperatures and pressures increase, the required overpotential is less significant, but for low temperature fuel cells it becomes most crucial loss to consider[35].

1.5.1 Reaction Mechanisms

The most commonly and extensively studied mechanism of ORR (for use in PEMFCs) is the four-electron reduction in acid, as outlined in Equation 1.1. However, there are many alternative mechanisms to reduce oxygen, dependent upon the catalyst and electrolyte employed. Standard electrode potentials for several common oxygen reactions in aqueous solutions are summarized in Table 1.2, though these potentials are very difficult to accurately measure experimentally due to their irreversible nature. In

addition, there are numerous side reactions that may also occur within these potential regimes, further complicating the measurement[36].

Ample research has been devoted to understanding the reaction pathway by which oxygen reduces so as to engineer superior catalysts. The direct 4-electron pathway is ideal, seen in acidic solutions:

$$O_2 + 4H^+ + 4e^- \rightarrow 2H_2O \tag{1.1}$$

Or in alkaline environments:

$$O_2 + 2H_2O + 4e^- \rightarrow 4OH^- \tag{1.2}$$

While these are considered "direct" pathways, there are obviously numerous steps involved before reducing oxygen; determining which of these is rate-limiting has been the focus of many researchers[21,37–44]. Alternatively, peroxide can be formed in a 2-electron reduction of oxygen, for acids via the mechanism:

$$O_2 + 2H^+ + 2e^- \rightarrow H_2O_2 \tag{1.3}$$

And in alkaline solutions as:

$$O_2 + H_2O + 2e^- \rightarrow HO_2^- + OH^- \tag{1.4}$$

In either environment, peroxide is then either reduced further via another 2-electron process or decomposes in the aqueous electrolyte, releasing O_2 as a product. This indirect pathway is less efficient, so selectivity of the catalyst, in addition to activity, is a necessary consideration.

Table 1.2. Selected ORR mechanisms and corresponding standard electrode potentials at 25˚C. *(Adapted from Ref [36])*

Electrochemical Reaction	*E_0 (V vs. SHE)*
$O_2 + 4H^+ + 4e^- \rightarrow 2H_2O$	1.229
$O_2 + 2H^+ + 2e^- \rightarrow H_2O_2$	0.695
$O_2 + 2H_2O + 4e^- \rightarrow 4OH^-$	0.401
$O_2 + H^+ + e^- \rightarrow HO_2$	-0.053
$O_2 + H_2O + 2e^- \rightarrow HO_2^- + OH^-$	-0.065
$O_2 + 2H_2O + 2e^- \rightarrow H_2O_2 + 2OH^-$	-0.133
$O_2 + e^- \rightarrow O_2^-$	-0.284

1.5.2 Electrochemical Measurements

The vast majority of the work presented in this thesis uses np-NiPt as an electrocatalyst. We begin with an annealed Ni-rich alloy (specifically $Ni_{77}Pt_{23}$), and machined into a 5mm in diameter disk, which is then fitted into a Pine Instruments Rotating Disk Electrode holder. This allows only the top surface of the disk to be exposed to any electrolyte, enabling a fixed geometric surface area. While there are several methods to dealloy NiPt alloys, we have found the best results are gained by cycling the potential of the disk repeatedly between 0.0 – 1.2 V vs the reversible hydrogen electrode (RHE) in a 0.1 M sulfuric acid solution. By doing so, we repeatedly oxidize and strip the

Ni from the alloy, dealloying deeper into the bulk with each cycle, leaving behind a porous network with ligaments between 3-5 nm in diameter with a Pt rich skin.

After dealloying the sample, a characteristic cyclic voltammogram (CV) is measured, offering a means to easily tell the quality, structure, and active surface area of the catalyst surface, an example of such shown in Figure 1.5, plotting the measured current density normalized by the geometric surface area against the applied potential. These measurements are routinely taken in a deaerated solution (i.e. an inert gas, typically N_2 or Ar is bubbled into the electrolyte so as to remove any oxygen that may form a side reaction), cycling between a lower limit of 0.0 V vs RHE, below which hydrogen evolves, and an upper limit of 1.23 V vs RHE, the theoretical onset potential for oxygen reduction.

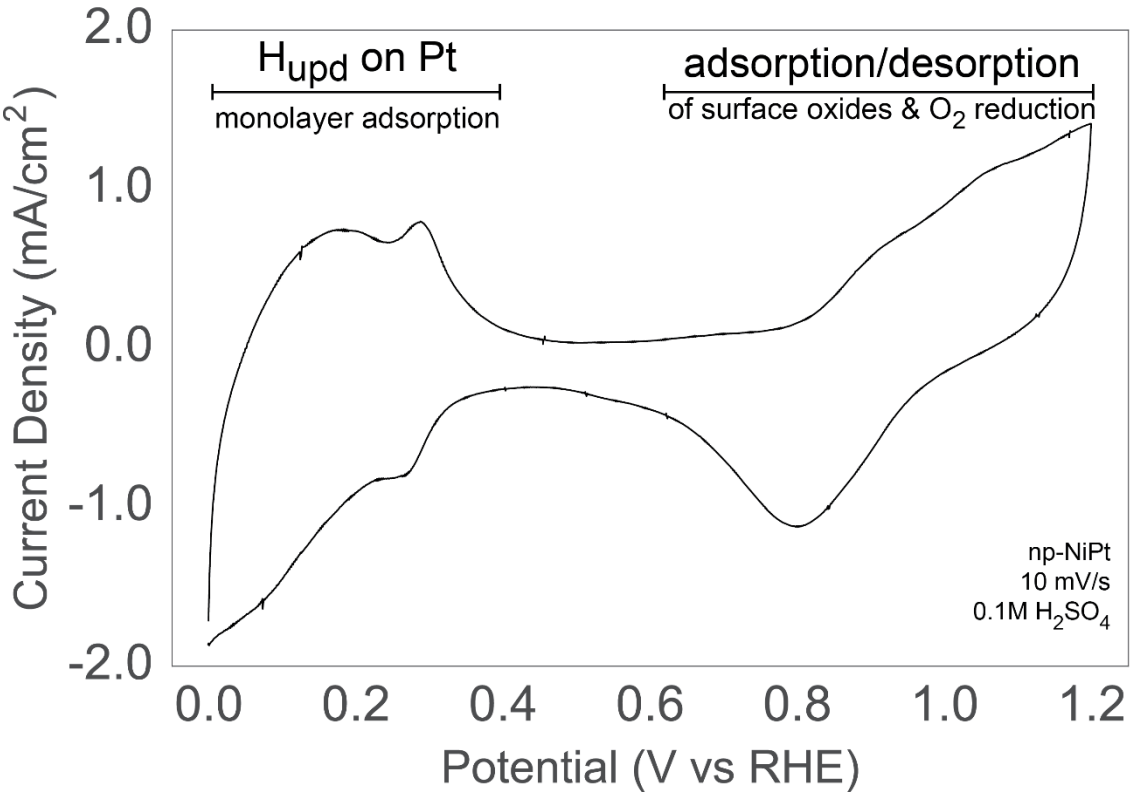

Figure 1.5. A characteristic cyclic voltammogram on np-NiPt, with an R_f ~ 150, measured in deaerated 0.1 M H_2SO_4 at a sweep rate of 10 mV/s.

Just above 0.0 V, hydrogen will underpotentially deposit (H_{UPD}) a monolayer onto the surface of Pt, with one electron transferred typically equivalent to one Pt atom. This ratio is not always exact, especially in many Pt alloys where it is slightly less than one electron per Pt, but is an adequate approximation[45]. From this current density, a subsequent charge and electrochemically active surface area can be determined by integrating the H_{UPD} area. Normalizing the calculated surface area by the geometric surface area results in the roughness factor, R_f, that estimates a dealloyed depth allowing all samples may be prepared uniformly and consistently.

The critical difference between nanoporous compared to planar or even nanoparticle electrocatalysts is that of electrochemically active surface area (EASA). For non-porous electrodes, the EASA usually corresponds to the true surface area of the electrodes, because reactant concentrations are always the same over any part of the catalyst surface. Consider instead a nanoporous catalyst with approximately 4 nm pores dealloyed to an arbitrary, but uniform depth. When there is less of a driving force for an electrochemical reaction to proceed (i.e. at a low overpotential), reactants can diffuse quite far into the pores before reduction because the reaction is under kinetic control. Therefore, in this case the EASA is close to the full surface area of the catalyst, using the bulk of the porous metal catalytically. In contrast, at high driving forces (high overpotentials) the reaction will proceed rapidly on the outer surface of the electrode without having the opportunity for reactants to travel into pores, i.e, the EASA is close to the projected geometric outer surface area of the catalyst. We can conclude that the active surface is itself a function of overpotential[20].

The residual Ni within the pores can be disregarded for most purposes due to the dealloying depth. By performing CVs in 0.1 M NaOH, one can measure the peak associated with the Ni oxidation at the surface near 0.8 V vs RHE. The ratio of NiOH relative to the non-Faradaic capacitive charging decreases substantially as the depth of dealloying increases, showing that the sample is dealloyed to significant depth so there is little to no residual electrochemically active surface Ni[25].

Often ORR behavior is determined using a Rotating Disk Electrode (RDE) apparatus, a schematic representation of which is shown in Figure 1.6, where the working electrode rotates at a fixed interval so as to control the thickness oxygen diffusion boundary layer.

Typically, this apparatus is then lowered into a dilute acidic electrolyte (often 0.1 M $HClO_4$) that has been saturated with oxygen, achieved by bubbling a high purity gas into the electrolyte. By sweeping the potential in an anodic direction, the current is measured, a characteristic result for np-NiPt plotted in Figure 1.7. A significant overpotential is required to drive the reduction, with the curve itself broken into two segments: (1) the diffusion limited regime, where the current density is dictated by how quickly the reactants can reach the catalyst surface and (2) the mixed diffusion limited and kinetically controlled region.

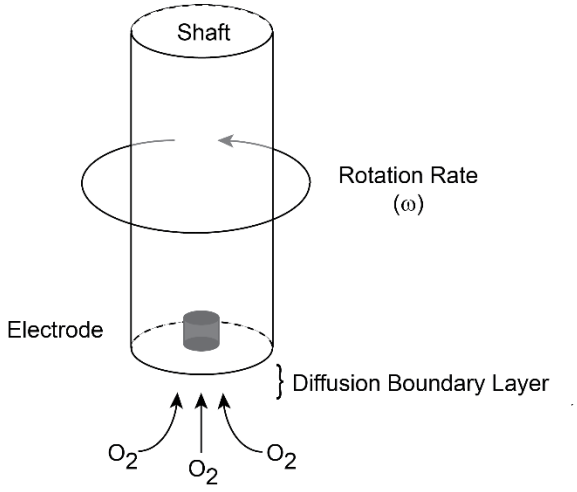

Figure 1.6. Schematic representation of a rotating disk electrode (RDE) apparatus, illustrating the rotation rate applied and subsequent diffusion boundary layer.

It is important to note, when measuring ORR activity, the standard protocol sweeps the potential slowly, but constantly, in the anodic direction. But, when using nanoporous metals as a catalyst, the surface area is drastically increased, so sweeping the potential

can lead to double-layer charging and non-Faradaic currents. In an effort to reduce this phenomenon, all measurements of ORR activity in this thesis, unless otherwise stated, have been recorded potentiostatically, i.e. the potential is fixed and held until the current reaches a steady state before stepping to the next set potential.

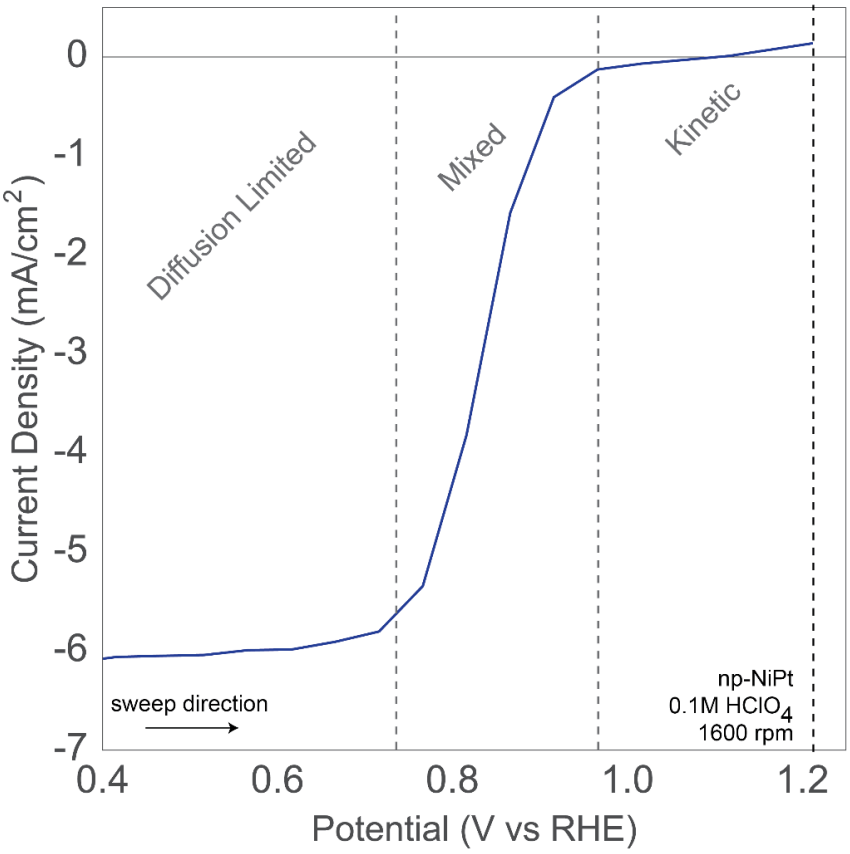

Figure 1.7. An example ORR curve measured for np-NiPt in oxygen-saturated 0.1 M $HClO_4$ at 25 °C, rotating at 1600 rpm, with points taken potentiostatically.

1.6 Further Increases in Activity

Both theoretical and experimental work has led to many improvements in Pt-based catalysts for the ORR, from geometric alterations of the catalyst increasing the active surface area through nanoparticle shape control[46], to porosity formation[47], to alloying Pt with transition metals[21]. While these adjustments have improved activity over commercially available catalysts, it still remains unclear whether these increases are sufficient for the adoption of fuel cells into mainstream automotive applications[48]. Dealloyed materials have the benefit of ease of processing, but otherwise the same gains in surface area to volume ratio can be achieved with nanoparticles, without the transport limitations that arise when using nanoporous metals, ultimately leading to the question: why even bother with nanoporosity?

The answer to this is simply that porosity can be filled with other materials. The activity for an electrocatalyst for ORR is most often assessed using bare metal electrodes in direct contact with an aqueous electrolyte. This architecture allows all reactants and products to have equivalent geometric access to the catalyst surface, but this does not always lead to an optimal reaction environment. By adding an intermediate phase into the pores of the metal as a layer between the catalyst and electrolyte, diffusive driving forces can be engineered into the system to force reactants to the catalyst and products away from it, increasing the overall system activity not available in other geometries.

Previous research explored np-NiPt electrodes encapsulated with the ionic liquid [MTBD][beti]. Ionic liquids are, as the name implies, salts with poorly-coordinated ions whose melting points are near room temperature. As the range of anions and cations to choose from is quite large, ILs have a wide variety of properties, and hence are being explored for applications in a variety of fields[49]. [MTBD][beti] has greater than twice the

oxygen solubility as aqueous acid, leading to a chemical potential bias for oxygen to diffuse into the IL, i.e., oxygen should be more concentrated near the catalyst surface compared to an aqueous solution when the reaction is under kinetic control. This is demonstrated in Figure 1.8, showing the improvement in activity by adding a small amount of [MTBD][beti] to a porous catalyst disk.

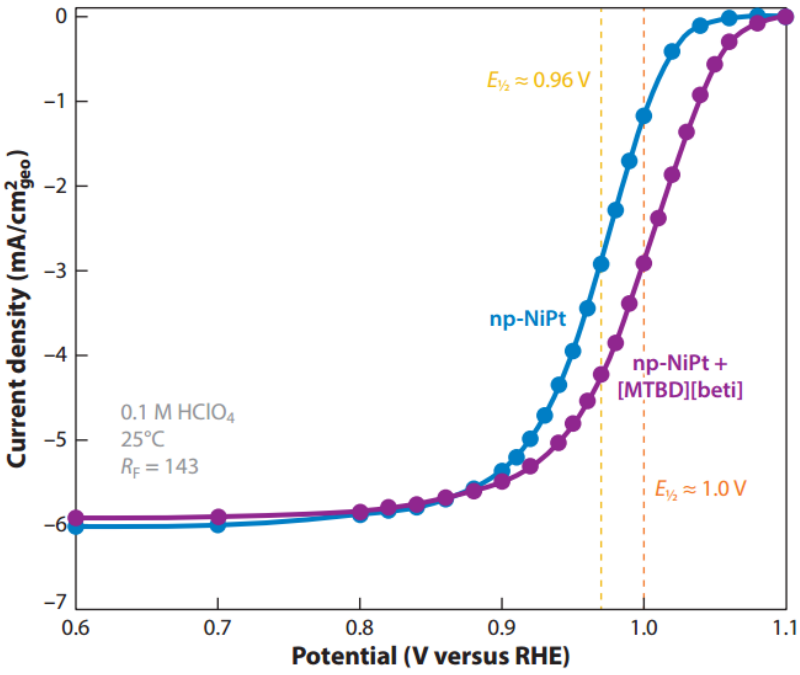

Figure 1.8. Improvements to ORR activity by the addition of IL to the pores, as shown by Snyder et al., specifically comparing np-NiPt *(blue)* with that on np-NiPt composite formed with the ionic liquid [MTBD][beti] *(purple)*, showing a 40mV decrease in overpotential require to drive ORR. *(Adapted from Ref [25])*

This strategy was recently used by Stamenkovic, et al. to make a composite Ni/Pt nanoframe + IL catalyst that has resulted in a 36-fold increase in activity for the ORR compared to neat Pt[50], the high oxygen solubility in this ionic liquid was thought to explain the drastic increase in the composite electrocatalyst activity, acting as a basis for exploring the effect of ILs on ORR activity.

References

1. Mccue, I., Benn, E., Gaskey, B. & Erlebacher, J. Dealloying and Dealloyed Materials. *Annu. Rev. Mater. Res.* **46,** 1–24 (2016).

2. Erlebacher, J. & Seshadri, R. Hard Materials with Tunable Porosity. *MRS Bull.* **34,** 561–568 (2009).

3. Erlebacher, J. An Atomistic Description of Dealloying. *J. Electrochem. Soc.* **151,** C614 (2004).

4. Wada, T., Yubuta, K., Inoue, A. & Kato, H. Dealloying by metallic melt. *Mater. Lett.* **65,** 1076–1078 (2011).

5. McCue, I., Gaskey, B., Geslin, P.-A., Karma, A. & Erlebacher, J. Kinetics and morphological evolution of liquid metal dealloying. *Acta Mater.* **115,** 10–23 (2016).

6. Erlebacher, J. Materials Science of Hydrogen/Oxygen Fuel Cell Catalysis. *Solid State Phys.* **61,** 77–141 (2009).

7. Zielasek, V. *et al.* Gold catalysts: Nanoporous gold foams. *Angew. Chemie - Int. Ed.* **45,** 8241–8244 (2006).

8. Wittstock, a, Zielasek, V., Biener, J., Friend, C. M. & Bäumer, M. Nanoporous Gold Catalysts for Selective Methanol at Low Temperature. *Science (80-.).* **327,** 319–322 (2010).

9. Biener, J. *et al.* Surface-chemistry-driven actuation in nanoporous gold. *Nat. Mater.* **8,** 47–51 (2009).

10. Fujita, T. *et al.* Atomic origins of the high catalytic activity of nanoporous gold. *Nat. Mater.* **11,** 775–780 (2012).

11. Hvolbæk, B. . *et al.* Catalytic activity of Au nanoparticles. *Nano Today* **2,** 14–18 (2007).

12. Marković, N. M., Grgur, B. N. & Ross, P. N. Temperature-Dependent Hydrogen Electrochemistry on Platinum Low-Index Single-Crystal Surfaces in Acid Solutions. *J. Phys. Chem. B* **101,** 5405–5413 (1997).

13. Stamenkovic, V. R. *et al.* Improved oxygen reduction activity on Pt3Ni(111) via increased surface site availability. *Science* **315,** 493–7 (2007).

14. Koh, S. & Strasser, P. Electrocatalysis on bimetallic surfaces: Modifying catalytic reactivity for oxygen reduction by voltammetric surface dealloying. *J. Am. Chem. Soc.* **129,** 12624–12625 (2007).

15. Lai, F. J. *et al.* Chemical dealloying mechanism of bimetallic pt-co nanoparticles and enhancement of catalytic activity toward oxygen reduction. *Chem. - A Eur. J.* **16,** 4602–4611 (2010).

16. Mani, P., Srivastava, R. & Strasser, P. Dealloyed Pt - Cu Core - Shell Nanoparticle Electrocatalysts for Use in PEM Fuel Cell Cathodes. **1,** 2770–2778 (2008).

17. Rudi, S., Gan, L., Cui, C. & Strasser, P. Dealloying of Pt Bimetallic Catalysts at Constant Electrode Potentials. *ECS Trans.* **58,** 581–586 (2013).

18. Wang, D. *et al.* Morphology and Activity Tuning of Cu_3Pt/C Ordered Intermetallic Nanoparticles by Selective Electrochemical Dealloying. *Nano Lett.* **15,** 1343–1348

(2015).

19. Chen, S. *et al.* Origin of oxygen reduction reaction activity on 'Pt_3Co' nanoparticles: Atomically resolved chemical compositions and structures. *J. Phys. Chem. C* **113,** 1109–1125 (2009).

20. Snyder, J. & Erlebacher, J. The Active Surface Area of Nanoporous Metals during Oxygen Reduction J. Snyder. *ECS Trans.* **41,** 1021–1030 (2011).

21. Greeley, J. *et al.* Alloys of platinum and early transition metals as oxygen reduction electrocatalysts. *Nat. Chem.* **1,** 552–556 (2009).

22. Xin, H., Holewinski, A. & Linic, S. Predictive structurereactivity models for rapid screening of pt-based multimetallic electrocatalysts for the oxygen reduction reaction. *ACS Catal.* **2,** 12–16 (2012).

23. Nørskov, J. K. *et al.* Origin of the overpotential for oxygen reduction at a fuel-cell cathode. *J. Phys. Chem. B* **108,** 17886–17892 (2004).

24. Stephens, I. E. L. *et al.* Tuning the activity of Pt(111) for oxygen electroreduction by subsurface alloying. *J. Am. Chem. Soc.* **133,** 5485–5491 (2011).

25. Snyder, J., Fujita, T., Chen, M. W. & Erlebacher, J. Oxygen reduction in nanoporous metal-ionic liquid composite electrocatalysts. *Nat. Mater.* **9,** 904–7 (2010).

26. Cullen, D. a. *et al.* Linking morphology with activity through the lifetime of pretreated PtNi nanostructured thin film catalysts. *J. Mater. Chem. A* **3,** 11660–11667 (2015).

27. McCue, I. *et al.* Apparent inverse Gibbs-Thomson effect in dealloyed nanoporous nanoparticles. *Phys. Rev. Lett.* **108,** 1–5 (2012).

28. Snyder, J., Mccue, I., Livi, K. J. & Erlebacher, J. D. Structure / Processing / Properties Relationships in Nanoporous Nanoparticles as Applied to Catalysis of the Cathodic Oxygen Reduction Reaction Structure / Processing / Properties Relationships in Nanoporous Nanoparticles as Applied to Catalysis of the Ca. (2012). doi:10.1021/ja3019498

29. Li, X. *et al.* Dealloying of noble-metal alloy nanoparticles. *Nano Lett.* **14,** 2569–2577 (2014).

30. Baldizzone, C. *et al.* Stability of Dealloyed Porous Pt/Ni Nanoparticles. *ACS Catal.* 5000–5007 (2015). doi:10.1021/acscatal.5b01151

31. Snyder, J., Livi, K. & Erlebacher, J. Oxygen reduction reaction performance of [MTBD][beti]-encapsulated nanoporous NiPt alloy nanoparticles. *Adv. Funct. Mater.* **23,** 5494–5501 (2013).

32. Wang, D., Zhao, P. & Li, Y. General preparation for Pt-based alloy nanoporous nanoparticles as potential nanocatalysts. *Sci. Rep.* **1,** 1–5 (2011).

33. Carrette, L., Friedrich, K. a & Stimming, U. Fuel Cells - Fundamentals and Applications. *Fuel Cells* **1,** 5–39 (2001).

34. *PEM Fuel Cell Electrocatalysts and Catalyst Layers: Fundamentals and Applications*. (Springer, 2008).

35. Laraminie, J. & Dicks, A. *Fuel Cell Systems Explained*. (John Wiley & Sons,

2003).

36. Hitchman, M. Electrochemical Oxygen Technology. *Analytica Chimica Acta* **285,** 403–404 (1994).

37. Ramaswamy, N. & Mukerjee, S. Fundamental Mechanistic Understanding of Electrocatalysis of Oxygen Reduction on Pt and Non-Pt Surfaces: Acid versus Alkaline Media. *Adv. Phys. Chem.* **2012,** 1–17 (2012).

38. Damjanovic, A., Genshaw, M. A. & Bockris, J. O. The Role of Hydrogen Peroxide in Oxygen Reduction at Platinum in H,SO, Solution. *J. Electrochem. Soc.* (1967).

39. Gasteiger, H. a & Ross, P. N. Oxygen Reduction on Platinum Low-Index Single-Crystal Surfaces in Alkaline Solution: Rotating Ring DiskPt(hkl) Studies. *J. Phys. Chem.* **100,** 6715–6721 (1996).

40. Sepa, D. B., Vojnovic, M. V. & Damjanovic, A. Reaction intermediates as a controlling factor in the kinetics and mechanism of oxygen reduction at platinum electrodes. *Electrochim. Acta* **26,** 781–793 (1981).

41. Nenad M. Markovic, Gasteiger, H. a. & Ross, P. N. Oxygen Reduction on Platinum Low-Index Single-Crystal Surfaces in Sulfuric Acid Solution: Rotating Ring-Pt(hkZ) Disk Studies. *J. Phys. Chem.* **99,** 3411 (1995).

42. Katsounaros, I. *et al.* Hydrogen peroxide electrochemistry on platinum: towards understanding the oxygen reduction reaction mechanism. *Phys. Chem. Chem. Phys.* **14,** 7384 (2012).

43. Wang, J. X., Zhang, J. & Adzic, R. R. Double-Trap Kinetic Equation for the

Oxygen Reduction Reaction on Pt (111) in Acidic. 12702–12710 (2007).

44. Ferreira de Morais, R., Franco, A. A., Sautet, P. & Loffreda, D. How Does the Surface Structure of Pt-Ni Alloys Control Water and Hydrogen Peroxide Formation? *ACS Catal.* acscatal.6b00842 (2016). doi:10.1021/acscatal.6b00842

45. Wang, C. *et al.* Design and synthesis of bimetallic electrocatalyst with multilayered Pt-skin surfaces. *J. Am. Chem. Soc.* **133,** 14396–14403 (2011).

46. Zhang, J., Yang, H., Fang, J. & Zou, S. Synthesis and oxygen reduction activity of shape-controlled Pt(3)Ni nanopolyhedra. *Nano Lett.* **10,** 638–644 (2010).

47. Wang, C., Markovic, N. M. & Stamenkovic, V. R. Advanced Platinum Alloy Electrocatalysts for the Oxygen Reduction Reaction. (2012).

48. Gasteiger, H. A., Kocha, S. S., Sompalli, B. & Wagner, F. T. Activity benchmarks and requirements for Pt, Pt-alloy, and non-Pt oxygen reduction catalysts for PEMFCs. *Appl. Catal. B Environ.* **56,** 9–35 (2005).

49. *Ionic Liquids in Synthesis*. (Wiley-VCH, 2008).

50. Chen, C. *et al.* Highly crystalline multimetallic nanoframes with three-dimensional electrocatalytic surfaces. *Science* **343,** 1339–43 (2014).

Chapter 2: Oxygen Reduction with np-NiPt+IL composites

2.1 Executive Summary

The activity of an ORR electrocatalyst is typically measured using metal electrodes in direct contact with an aqueous electrolyte, allowing all reactants and products to have equivalent geometric access to the catalyst surface. By adding an intermediate phase as a layer between the catalyst and the electrolyte, diffusive driving forces can be engineered within the catalyst itself in an effort to increase the composite's activity. Previous research explored this concept using np-NiPt encapsulated with the ionic liquid [MTBD][beti]. The high oxygen solubility in this ionic liquid was thought to explain the nearly doubled increase in the composite electrocatalyst activity, but it is possible that other ionic liquid properties (water solubility, oxygen diffusivity, ionic conductivity, viscosity) might also be affecting ORR activity. In this chapter, a number of ionic liquids in nanoporous NiPt/ionic liquid composite catalysts were surveyed with an eye toward clarifying to what extent the physical properties of the IL have on the activity of the composite ORR catalyst. Overall, we find the oxygen solubility and water solubility appear to most strongly affect the decrease in ORR overpotential for these nanoporous metal + IL composite catalysts.

2.2 Introduction and Literature Review

The benefit of nanoporous metals is the ability to fill the pores with a secondary material, thus tailoring the properties in direct contact with the catalyst surface as desired. Previous work in our group focused on using the ionic liquid [MTBD][beti] filling the pores of a np-NiPt disk, creating such a composite catalyst[1]. This IL has an increased oxygen solubility, more than twice that of the surrounding electrolyte, leading to a chemical potential bias for oxygen to diffuse into the IL, i.e., oxygen should be more concentrated near the catalyst surface compared to an aqueous solution when the reaction is under kinetic control.

More specifically, and assisted by the cartoon in Figure 2.1 showing an idealized electrolyte/IL/metal electrode configuration, ORR is well-known to be first-order in the oxygen concentration at the electrode surface[2]. Therefore, at equilibrium, the concentration of oxygen in the IL must be higher than in the aqueous electrolyte in order to satisfy the need for a uniform chemical potential. This discontinutity continues under kinetically limited conditions, so even as the concentration of oxygen in both the IL and electrolyte decreases, the local chemical equilibrium $\mu_{O_2}^{IL} = \mu_{O_2}^{electrolyte}$ is maintained. It follows that, as ORR is first order in the oxygen partial pressure (concentration), ORR activity should be increased by a factor equal to the ratio of oxygen solubilities. This increase was indeed seen in bulk np-NiPt[1], naoparticulate np-NiPt[3], and Ni/Pt nanoframes[4].

A very significant aspect of the IL-impregnated nanoporous catalyst concept is that the ORR activity increase is associated primarily with the properties of the ionic liquid, and not the properties of the catalyst itself. As such, there is significant room for improvement – for instance, if the ORR activity increase is truly correlated to the oxygen solubility, then there are indeed materials with much higher oxygen solubility than the [MTBD]-based ILs studied so far. As an example, perfluorodecalin has an oxygen solubility approximately 75 times higher than water, yet this organic molecule is not useful as np-metal composite catalyst material because of its high vapor pressure and other physical properties, but this still suggests that significant further improvements in composite catalyst activities are possible.

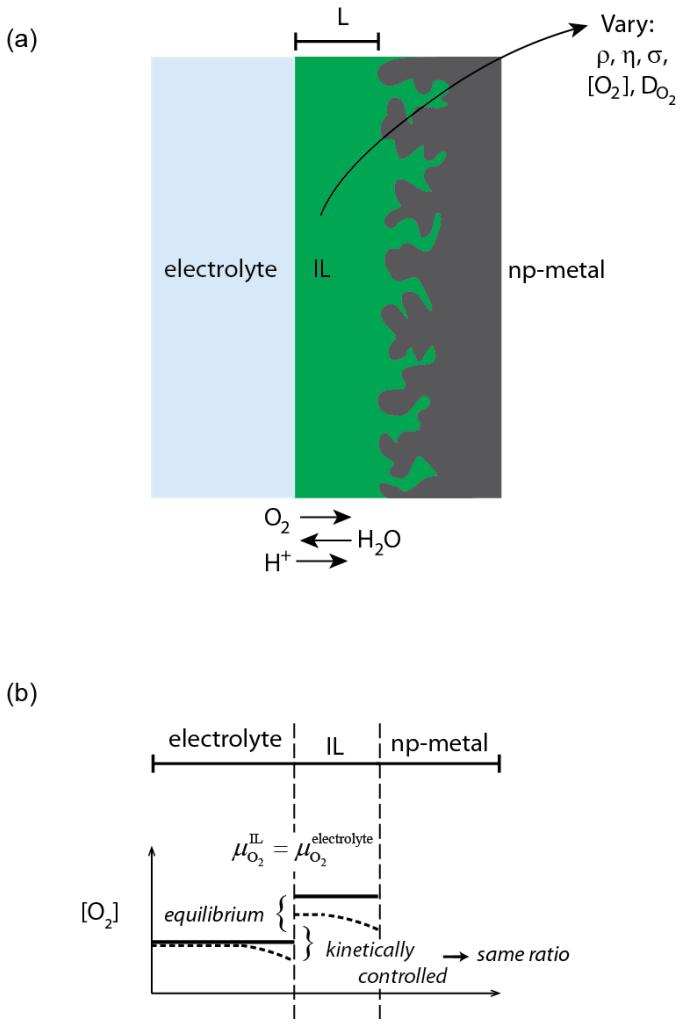

Figure 2.1. Schematic representation of (a) nanoporous metal + ionic liquid composite catalyst in contract with an aqueous electrolyte and (b) chemical equilibrium discontinuity due to differences in oxygen solubility between electrolyte and ionic liquid.

However, Figure 2.1 also shows that there are many other properties of the IL that may affect the overall activity and reaction kinetics. For instance, the material should possess a high enough conductivity so as not to create electrical resistance losses when used. Hydrophobicity is ideal in order to maintain a true layer between the catalyst and aqueous electrolyte without the IL simply washing away. Practical limitations such as viscosity of the substance are important to consider not from an activity standpoint, but for formation of the composite catalyst. It is yet unknown how much these factors affect

oxygen reduction relative to oxygen solubility. In this work, we explored a number of these different factors in IL-filled np-NiPt composite catalysts, specifically including geometric features such as IL thickness, IL physical properties such as viscosity and density, transport properties of protons within the IL (by varying IL proticity), and transport of water within the IL (by varying IL hydrophobicity).

2.3 Experimental Methods

The experimental plan was to vary the properties of the IL by varying its composition, keeping the catalyst (bulk np-NiPt) fixed. On one hand, our notion was to identify what properties of the IL are required to optimize ORR activity in the composite catalyst; on the other hand, our goal was to confirm (or not) that the primary physical property of the IL that controlled the increase in ORR activity was oxygen solubility.

Oxygen reduction activity was measured using a Gamry Interface 1000 Potentiostat and a solution of 0.25 M perchloric acid (Sigma Aldrich, 70%) using glassware cleaned by soaking in a solution of NoChromix (Godax Laboratories, Inc.) and sulfuric acid overnight. In an effort to limit non-faradaic currents commonly found with highly porous metals, ORR was measured potentiostatically. Data intervals were taken every 100 mV in the diffusion limited regime and 15 mV in the mixed kinetic-diffusion region, allowing the current to stabilize at each point.

2.3.1 Materials Preparation & Characterization

Combinations of anions and cations shown in Figure 2.2 were used to synthesize the ILs used in this study, rationally varying the physical properties of the IL layer. These anion and cations were chosen for the following reasons:

- [MTBD]: this protic cation was used in Refs. [1,3,4] and led to ILs with melting points below room temperature.
- [HNC(dma)]: this protic cation also led to ILs with low melting points. It is significantly less "bulky" than MTBD, suggesting higher proton conductivity.
- [M3BN]: this quaternary ammonium cation is one of the simplest aprotic cations.
- [bmim]: this aprotic cation contains a bulkier charge holding group, suggesting a significantly different proton conductivity compared to [M3BN].
- [beti]: This bis-perfluorethyl sulfonamide was used in Refs. [1,3,4], and with [MTBD] led to an IL with approximately two times higher oxygen solubility than the aqueous electrolyte.
- [bfpi]: Similar to [beti], this anion has slightly longer perfluorethyl sidechains. It was hoped that as a result, ILs based on [bfpi] would have higher oxygen solubility.

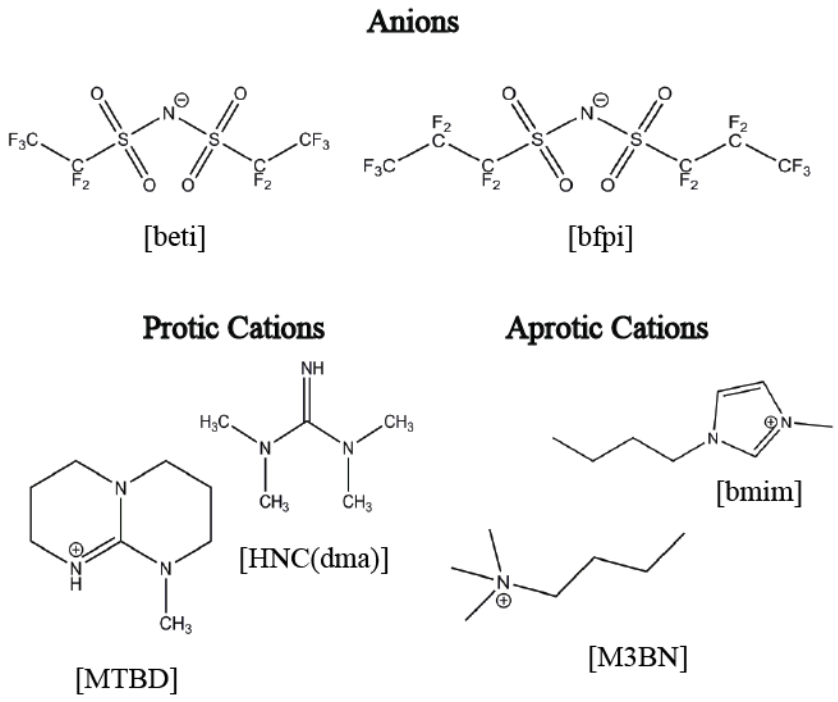

Figure 2.2. Chemical structure of IL anions and cations used in this study.

Nanoporous NiPt (np-NiPt) was formed through electrochemical dealloying of 77 at.% Ni/Pt precursor alloys by cycling the potential repeatedly from 0.0 - 1.2 V vs. RHE (reversible hydrogen electrode) in 0.1 M H_2SO_4 (J.T. Baker, 95-98%). For each IL composite tested, the surface of the NiPt disk was polished and dealloyed to approximately the same depth, measured using hydrogen under potential deposition (H_{UPD}) to the same effective surface area. This effective surface area was normalized by the geometric surface area, yielding the roughness factor R_f. In all examples here, the roughness factor was typically near $R_f \sim 120$, corresponding to a dealloyed depth of approximately 850 nm[5].

To synthesize aprotic ILs, aprotic cations (in their chloride salt form) [bmim] (1-Butyl-3-methyl-imidazolium chloride, Sigma Aldrich, 95%) and [M3BN]

(Methyltributylammonium chloride, Sigma Aldrich, 75 wt% solution in water) were added in an aqueous solution to an equimolar solution of Li [beti] (Lithium bis(pentafluoroethanesulfonyl)imide, Oakwood Chemical). This was rinsed several times with deionized water and allowed to fully dry under reduced pressure at 75 °C for 24 hours, to form ILs [bmim][beti] and [M3BN][beti].

To synthesize protic ILs, the method outlined by Luo et al.[6] was employed. Equimolar amounts of cation, [MTBD] (7-Methyl-1,5,7-triazabicylco[4.4.0]dec-5-ene, Sigma Aldrich, 98%) or [HNC(dma)] (1,1,3,3-Tetramethylguanidine, Sigma Aldrich, 99%) and anion, lithium salt of [beti] or [bfpi] (Lithium bis(1,1,2,2,3,3,3-heptafluoro-1-propanesulfonyl)imide, Wako Pure Chemicals Industries, Ltd.) were dissolved in deionized water and cooled in an ice bath. The cation solution was neutralized by adding concentrated nitric acid (BDH) dropwise and subsequently mixed with the anion solution. Similar protocols to the aprotic ILs were used to wash and dry the resulting IL.

The viscosity of each IL was measured using a capillary viscometer (Semi-Micro Extra Low Charge Viscometer, Cannon Instruments). Densities were determined using a Mettler Toledo Analytical Balance with a precision of ±0.01 mg to weigh a known volume of IL. Water content was measured using Karl Fischer Titration (Mettler Toledo C20 Coulometric KF Titrator) and determined to be less than 1000 ppm for each dry sample. Conductivity was calculated through potentiostatic electrical impedance spectroscopy measurements[7] using a Gamry Reference 3000 potentiostat and self-made conductivity cell, calibrated using NaCl solutions (Sigma Aldrich).

Oxygen solubility and diffusivity were measured using a Pt microdisc electrode, following the procedure outlined in Evans et al.[8]. Briefly, a small drop of IL (10 µl) is

placed in contact with a working electrode composed of an encapsulated 10 μm Pt wire, the area of which is calibrated using ferrocene redox couple. The IL is fully saturated with oxygen and held at a potential of zero current, relative to an Ag silver wire reference electrode. The potential is then stepped to one where oxygen is fully reduced with no kinetic limitations, and the current decays as oxygen gets reduced. The resulting current versus time data is modeled by the equation

$$I = -4nFD_{O_2}\left[O_2\right]r_d f\left(\tau\right) \tag{1.1}$$

where

$$f\left(\tau\right) = 0.7854 + 0.88863\tau^{-1/2} + 0.2146e^{-0.7823\tau^{-1/2}} \tag{1.2}$$

and

$$\tau = \frac{4D_{O_2}t}{r_d^2} \tag{1.3}$$

The diffusivity and solubility of oxygen, D_{O_2} and $\left[O_2\right]$ respectively, are simultaneously fit to the potential decay versus time. A nuance to this measurement is that the fits are sensitive to the time offset, i.e., when one sets $t = 0$. There is a systematic error introduced due to the few milliseconds it takes to step to the desired potential. During this time period, some oxygen within the IL is being reduced while within the kinetically limited regime, so choosing a point for the onset time incorporating the entire potential ramp overestimates the oxygen solubility. Yet, waiting until the potential reaches the desired point results in some oxygen being prematurely reduced and hence

underestimates the quantity. For our reported values, we selected a midpoint offset time that minimizes these effects and is comparable to reported literature values.

2.3.2 Rotating Disk Electrode Experiments & Limitations

These measurements were initially carried out using the Rotating Disk Electrode apparatus previously described, as was used in Refs [1,3,4]. To form the composite system, a drop of IL is placed on the surface of the np-NiPt electrode, placed into a vacuum oven to further encourage the IL to penetrate into the pore. After, the excess IL was removed by spinning the holder in the RDE.

While this creates a thin uniform layer of IL over the np-NiPt, the thickness of that layer, in addition to the amount of IL that truly penetrates into the pore, is going to vary significantly when using different ILs, each with a distinct viscosity (some being orders of magnitude in difference). We noticed promptly that it was impossible to distinguish the behavior of the IL from the thickness of the layer used. These results are summarized in Figure 2.3, for 3 of the ILs tested. One can clearly tell the activity of the [MTBD][beti] composite aligns with previous research using this system, with a similar increase in halfwave relative to np-NiPt. Both of the other composites examined, [bmim][beti] and [M3BN][beti], have noticeable differences in the diffusion limited currents (0.4 – 0.7 V vs RHE), but is this due to the aprotic nature of the cations or their reduced oxygen solubility? Or is it a result of the considerably different viscosities of each? Upon visual inspection of the samples, it was apparent the [M3BN][beti] composite had a more noticeable IL layer (and also the highest viscosity) than the protic counterpart [MTBD][beti].

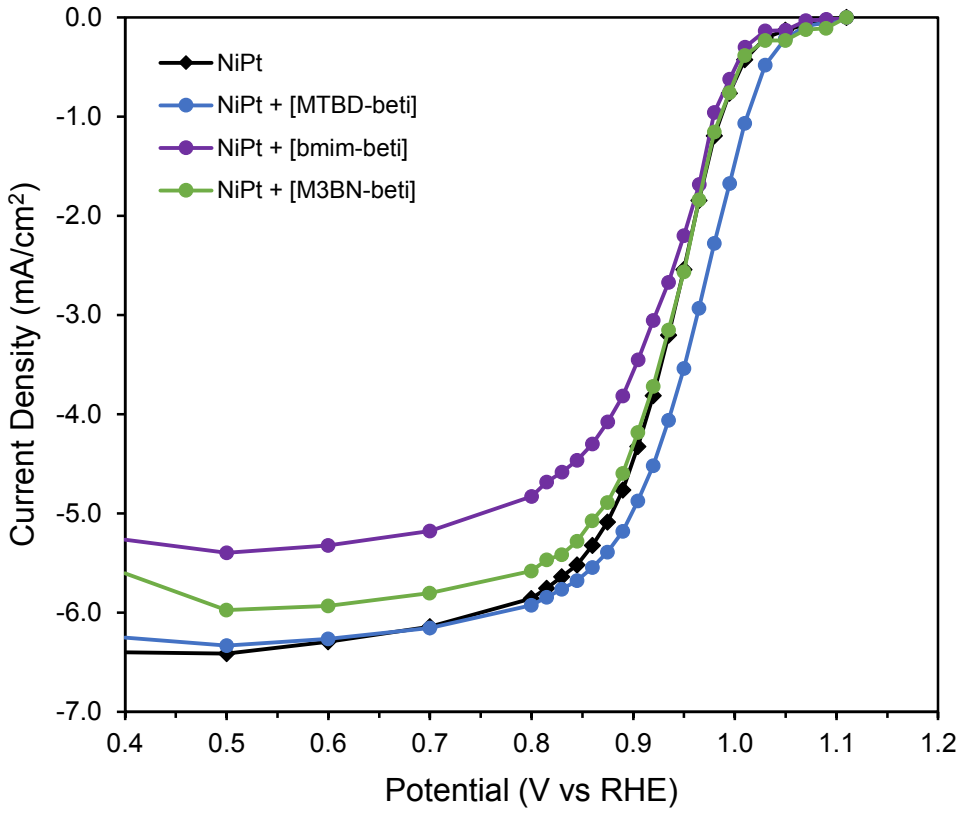

Figure 2.3. Potentiostatic ORR current density versus potential for np-NiPt+IL composites using a Rotating Disk Electrode apparatus at 1600 rpm in 0.1 M H_2SO_4.

After numerous attempts to replicate data and minimize variations in IL thickness/incorporation, it became evident employing an RDE to measure ORR activity in various np-metal+IL composites would not be an ideal geometry to deconvolute these results.

2.3.3 Flow Cell Design

In order to maintain a planar electrolyte/IL interface, and an IL with controlled volume, a channel flow cell was fabricated similar to that outlined by Heller-Ling et al.[9],

using a Pine Instruments RDE sample holder for the working electrode, pressure fitted into the channel; a Pt wire as a counter electrode; and a secondary beaker housing a mercurous sulfate (Hach) reference electrode. The channel has a height of 1 mm, width of 30 mm, and is 100 mm in length. A variable flow rate peristaltic pump (Fisher-Scientific) allowed a range of flow rates, from 5 – 75 ml/min, monitored by a flow meter (Gilmont). A schematic of the flow cell is shown in Figure 2.4.

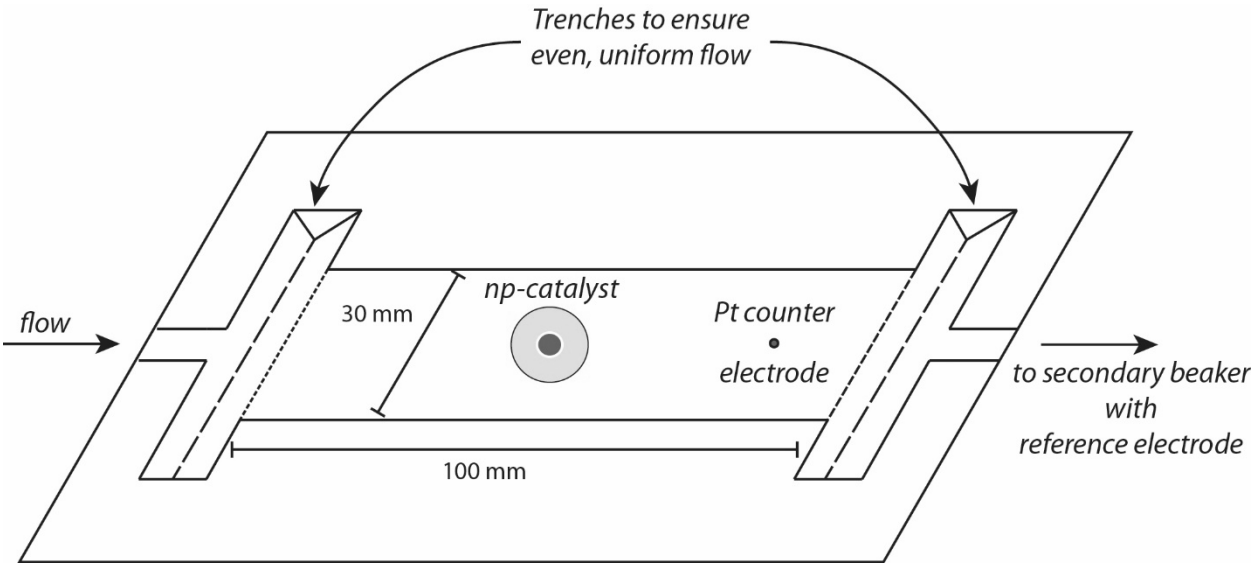

Figure 2.4. Schematic of flow cell developed for this study to maintain a planar electrode geometry with control over the thickness of IL layer in the composite.

To ensure that there was laminar flow over the electrodes, the Reynolds number (*Re*) was calculated. This dimensionless number is defined as,

$$\mathrm{Re} = \rho VL / \mu \tag{1.4}$$

where ρ is the density of the fluid, V is the velocity (found by dividing the volumetric flow rate by the cross-sectional area the fluid is flowing through), L is the characteristic length, and μ is viscosity. For the flow cell employed, the width of the channel is significantly wider than the height (30 mm versus 1 mm respectively), meaning the system can be approximated as flow between two parallel plates and as such L can be characterized by the height of the channel (1 mm). Substituting the values of water for density and viscosity in an approximation yields a $Re \sim 1$, significantly below the value of 1,400 that dictates the flow is laminar for this geometry. In addition, the uniform distribution of a dye fed into the input electrolyte stream as it flowed over the catalyst electrode visually confirmed even flow over the electrodes.

A fixed volume of IL (2.5 -10 µl) was added to the porous metal sample to form the composite catalyst – any smaller volume is difficult to accurately measure and be uniformly distributed. Geometrically, the volume of IL can be used to estimate the thickness of the layer, presuming no volume penetrates into the porous metal. Under this assumption, a 5 µl volume corresponds to a thickness of 255 µm. To more exactly determine the thickness of IL above the np-NiPt electrode outer geometric surface, an IL that is solid at room temperature was added to the porous metal at a temperature above its melting point, allowed to penetrate into the porous structure and then cooled. The thickness was simply measured in cross-section using an optical scope (Olympus PMG 3), shown in Figure 2.5. This, combined with a SEM (JEOL JSM-6700F) cross section to determine the depth of porosity, allows a more precise measurement of the IL thickness. Typical IL thicknesses were employed ranged from 40 – 420 µm, the majority of experiments using a 250 µm layer. We note that these are significantly thicker IL layers

than those used in Refs. [1, 3, 4] which by design tends to exacerbate the effects of different IL properties on the ORR activity.

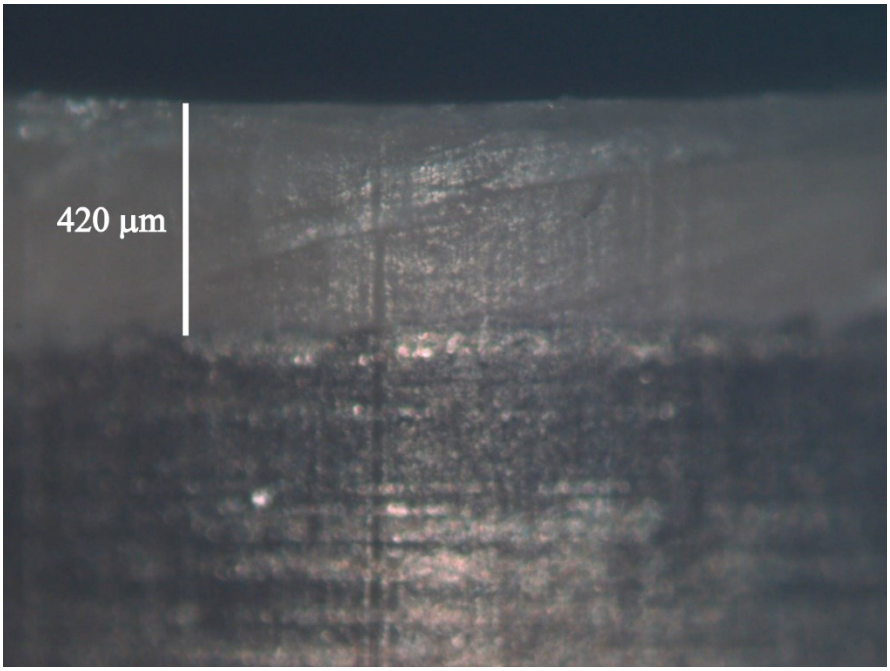

Figure 2.5. Optical micrograph of IL on np-NiPt to characterize the thickness of IL added to form the composite system. Image of 10 μl of [DBU][beti], an IL with a melting point near 50 °C. The IL was added to a porous disk above this temperature, following the same protocol as the other composites, before being cooled to room temperature and solidifying. The cross-section thickness of this IL layer above the surface of a np-NiPt disk was measured using an Olympus PMG 3 optical microscope.

Figure 2.6 displays the ORR curves obtained using the flow cell apparatus for np-NiPt at varying flow rates, from 10 – 50 ml/min. A monotonic increase in the diffusion-limited current density magnitude i_{DL} on volumetric flow rate v_f is observed, analogous to the diffusion-limited current density vs. rotation rate using an RDE. Similar behavior was also observed with IL-impregnated composites, albeit with lower magnitude diffusion-limited current densities. In all cases, the IL layer appeared undisturbed during flow of the electrolyte composite catalyst. In addition, the hydrophobic ILs used in this

study always balled up when directly dropped into aqueous solution, i.e., it is very easy to see them, and we observed no evidence of IL ever leaving electrode, with one caveat. When a planar, non-porous electrode was used, the IL tended to wash away, illustrating the importance of capillary forces within the porous network being important to keep the IL in place.

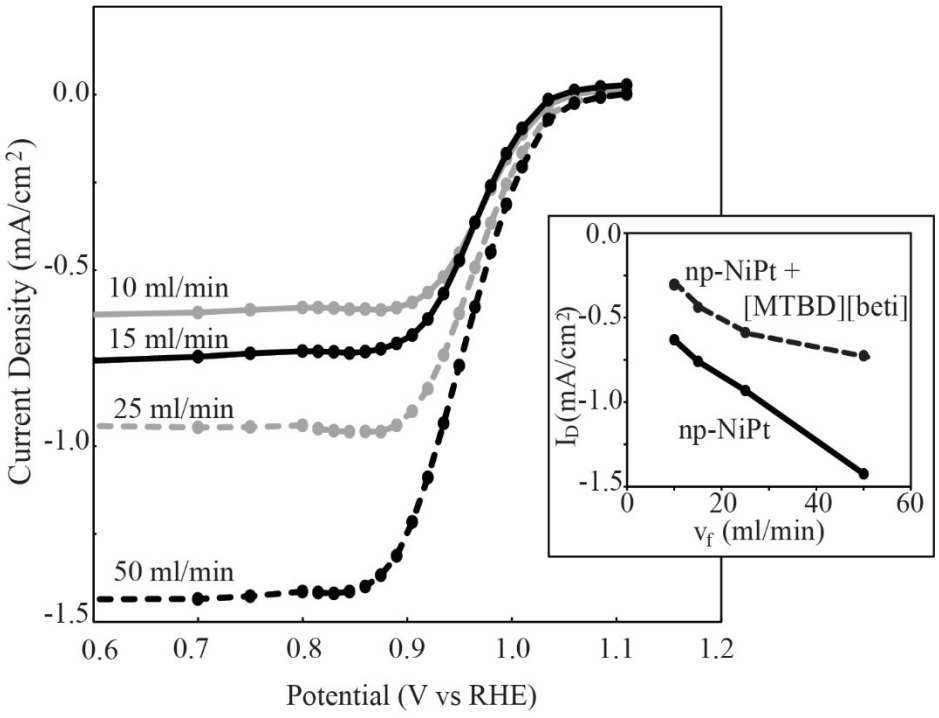

Figure 2.6. Potentiostatic ORR current on bare np-NiPt with varying flow rate. *Inset*: Diffusion-limited current density versus volumetric flow rate for np-NiPt and np-NiPt + [MTBD][beti].

Theoretical analysis of i_{DL} over a catalytic electrode in a flow cell predicts a dependence of the form

$$i_{DL} \propto v_f^{1/3} \tag{1.5}$$

The inset of Figure 2.6 shows that this dependence holds well for bare np-NiPt in our flow cell. The composite catalyst has an IL/metal interface nearly 0.25 mm below the IL/electrolyte interface. This secondary barrier makes for a significantly more complex analysis of i_{DL} vs. v_f. Nonetheless as shown in the inset for np-NiPt + [MTBD][beti] (5 µl), i_{DL} still increases with v_f.

2.4 Results

2.4.1 Physiochemical Properties of ILs

Measured properties of the ILs used in this study are listed in Table 2.1, along with oxygen solubility and diffusion coefficient measured for the electrolyte. There is an order of magnitude difference in the viscosities of ILs tested, although this did not correlate with either ionic conductivity or oxygen diffusivity. While viscosity played a role in experimental setup, i.e. measuring out a precise volume or forming the composite, little effect on ORR activity (half-wave position) was noticed.

Table 2.1. Physiochemical properties measured for each ionic liquid.

Ionic Liquid	ρ *(g/ml)*	η *(mPa·s)*	σ_C *(ms/cm)*	$[O_2]$ *(mM)*	D_{O2} *(10^{-6} cm^2/s)*	$[H_2O]$ *(M)*
[MTBD][beti]	1.54 ± 0.05	392.3 ± 1.4	1.96 ± 0.50	3.19 ± 0.01	4.84 ± 0.16	1.33 ± 0.01
[HNC(dma)][beti]	1.56 ± 0.02	232.7 ± 1.8	13.1 ± 2.15	1.91 ± 0.16	8.70 ± 0.92	3.53 ± 0.01
[HNC(dma)][bfpi]	1.51 ± 0.07	434.9 ± 1.6	7.35 ± 3.12	0.80 ± 0.03	40.3 ± 2.22	1.56 ± 0.01

[bmim][beti]	1.52 ± 0.03	112.0 ± 0.5	4.22 ± 1.11	1.50 ± 0.49	10.1 ± 4.38	0.62 ± 0.01
[M3BN][beti]	1.26 ± 0.05	1184.3 ± 9.4	2.77 ± 0.59	0.90 ± 0.37	6.72 ± 2.84	0.31 ± 0.01
0.25M $HClO_4$	--	--	--	1.55	13.9	--

The ionic conductivities for the [HNC]-based ILs are noticeably higher than the other ILs, and coincides with a significantly higher magnitude for the diffusion limited current in the ORR when using this cation.

Oxygen solubility is thought to be dictated by the anion[10], our data proving relatively consistent with this idea. The bulk of our composite systems employ the [beti] anion, so while different cations led to modest variations in oxygen solubility, there were no large orders of magnitude difference among our values.

2.4.2 Oxygen Reduction Reaction Activity

After an IL-dependent break-in period, potentiostatic ORR currents versus potential for each IL-composite at a constant IL volume of 5 µl and flow rate of 15 ml/min were measured. Results are shown in Figure 2.7, comparing each composite with the bare np-NiPt sample as a baseline. The diffusion limited current density and half-wave potentials for each IL are summarized in Table 2.2. All the composite catalysts here improved the half-wave relative to that of bare np-NiPt.

Furthermore, we confirmed that the shifts in half-wave are independent of the thickness of the IL layer, and that the diffusion-limited current density approaches the value for bare np-NiPt as the IL thickness decreased. However, reliably controlling the

IL volume between samples and composites is considerably more difficult from a practical standpoint for the smaller volumes of IL, because measuring such small volumes of highly viscous fluids is problematic. Our “standard” condition, 5 μl of IL, represents a compromise between the achieving the desired current density magnitudes and exact repeatability between composites.

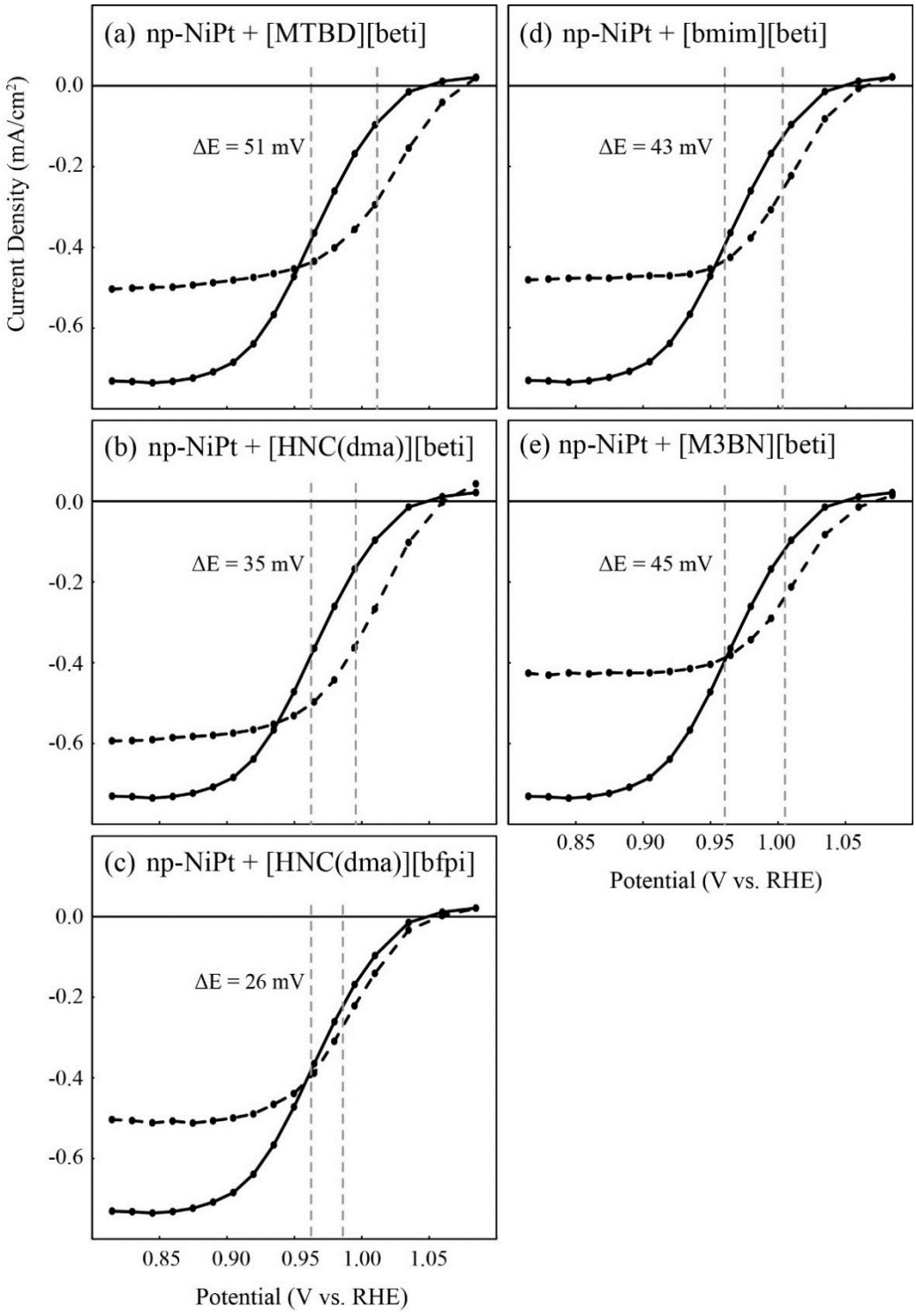

Figure 2.7. Potentiostatic ORR current density versus potential for np-NiPt *(solid line)* and (a) np-NiPt+[MTBD][beti], (b) np-NiPt+[HNC(dma)][beti], (c) np-NiPt+[HNC(dma)][bfpi], (d) np-NiPt+[bmim][beti], and (e) np-NiPt+[M3BN][beti].

Table 2.2. Electrochemical properties of ILs taken from Figure 2.7.

Sample	*Half-wave (V)*	I_D *(mA/cm²)*
np-NiPt	0.96	-0.76
np-NiPt + [MTBD][beti]	1.01	-0.52
np-NiPt + [HNC(dma)][beti]	1.00	-0.65
np-NiPt + [HNC(dma)][bfpi]	0.99	-0.51
np-NiPt + [bmim][beti]	1.00	-0.49
np-NiPt + [M3BN][beti]	1.00	-0.45

2.5 Discussion

2.5.1 Oxygen Reduction in the Diffusion Limited Regime

In the diffusion limited regime (0.6-0.8 V in Figure 2.7), there is no obvious correlation between i_{DL} and oxygen solubility. In order to explore our system in greater detail, consider the hydrodynamic equation governing the flow cell geometry[9]

$$i_{DL} = 0.925nF\left[\mathrm{O_2}\right]D_{\mathrm{O_2}}^{2/3}\left(\frac{v_f}{h^2 d}\right)^{1/3} wx^{2/3} \tag{1.6}$$

where *n* is the number of electrons, *F* is Faraday's constant, *h, d, w,* and *x* are geometric parameters of the flow cell, assuming a planar geometry, and the other parameters are defined above. The interface between IL and metal catalyst is below the level of the IL/flowing electrolyte interface, so this equation doesn't exactly describe our situation. However, if the product $\left(\left[\mathrm{O_2}\right]D_{\mathrm{O_2}}^{2/3}\right)_{electrolyte}$ were greater than $\left(\left[\mathrm{O_2}\right]D_{\mathrm{O_2}}^{2/3}\right)_{IL}$, we would expect that oxygen be diffusion limited in the IL, and not the aqueous electrolyte,

considerably complicating any conclusions. In our case, the independent measurements of these parameters confirmed that in all cases this product is greater in the IL than in the aqueous electrolyte, so that the presence of the IL only affects ORR activity in the kinetically controlled potential regime.

2.5.2 Kinetically Controlled Regime

Our explanation that the increased activity in IL + np-NiPt composites is dependent upon the increased oxygen solubility is rooted in the extensive previous work to determine the reaction pathways and rates for oxygen reduction. The kinetic ORR current are generally described by an expression of the form[11,12].

$$i = nFK\left[\mathrm{O}_2\right]\left(1-\Theta_{ad}\right)^x \exp\left(-\beta FE/RT\right)\exp\left(-\gamma r\Theta_{ad}\right)/RT \tag{1.7}$$

where n is number of electrons transferred ($n = 4$ here), K is a chemical rate constant, Θ_{ad} is the surface coverage of adsorbed species, x depends on site requirements of adsorbates (a value of 1 or 2), β and γ are symmetry factors, E is the applied potential, and $r\Theta_{ad}$ describes the rate of change of the free energy of adsorption with the surface coverage by adsorbing species. Details aside, Eq. 2.7 indicates that the ORR current is first order in the concentration of oxygen at the catalyst surface – doubling the concentration there via the IL intermediate phase should double the current.

All composites tested in this study improved the kinetic activity over that of neat np-NiPt, assessed by the shift in the half-wave potential. Comparing the ILs amongst themselves, [MTBD][beti] has the greatest increase in oxygen solubility, with a

concentration of 3.2 mM, while [HNC(dma)][bfpi] has the lowest of the ILs tested at 0.8 mM, corresponding to the highest and lowest shifts in the half-wave respectively. Both ILs are protic, in addition to having similar viscosities and densities, so our initial hypothesis regarding oxygen solubility dependence being the only vital factor seems accurate in this respect. However, we measured the oxygen solubility of the electrolyte, 0.25 M perchloric acid, to be 1.55 mM, a solubility higher than that of the majority of ILs we tested in our composites, requiring us to nuance our working model.

One factor that straightforwardly could be impacted by the addition of an IL is the adsorption behavior on the Pt surface. Assuming reaction intermediates have minimal coverage and there is no significant contamination of halides or sulfides within the electrolyte, the adsorbed species of interest is OH_{ad}. If the IL were to disrupt an ordered water or oxide layer forming at the surface of the metal interface, perhaps more open active sites would be available and thus increase activity[12]. To examine this, we examined the cyclic voltammetry of each composite, shown in Figure 2.8, specifically looking for a shift in the onset of Pt oxidation.

Examining the hydrogen adsorption/desorption region of the curves, between 0.0 – 0.4 V vs. RHE in Figure 2.8, it becomes apparent the magnitude of the currents for each composite compared to the bulk np-NiPt are reduced. However, when correlated to the double layer region (0.4 - 0.6 V vs. RHE), the currents scale accordingly, implying the area under the curve would remain fairly consistent between samples and is likely an effect due to the decreased proton mobility through the thick IL layer. For instance, np-NiPt + [M3BN][beti] appears the most diminished, but also has the highest viscosity. These transport issues are not as readily noticed in the ORR curves since those

measurements are steady state, as opposed to the sweep that is performed for cyclic voltammetry. Upon examining the Pt oxidation/reduction portion of the curve from 0.6 to 1.2 V vs. RHE, there is no significant change in the onset potential for Pt oxidation relative to the bulk np-NiPt, so it is unlikely we are disturbing any ordered layer at this interface.

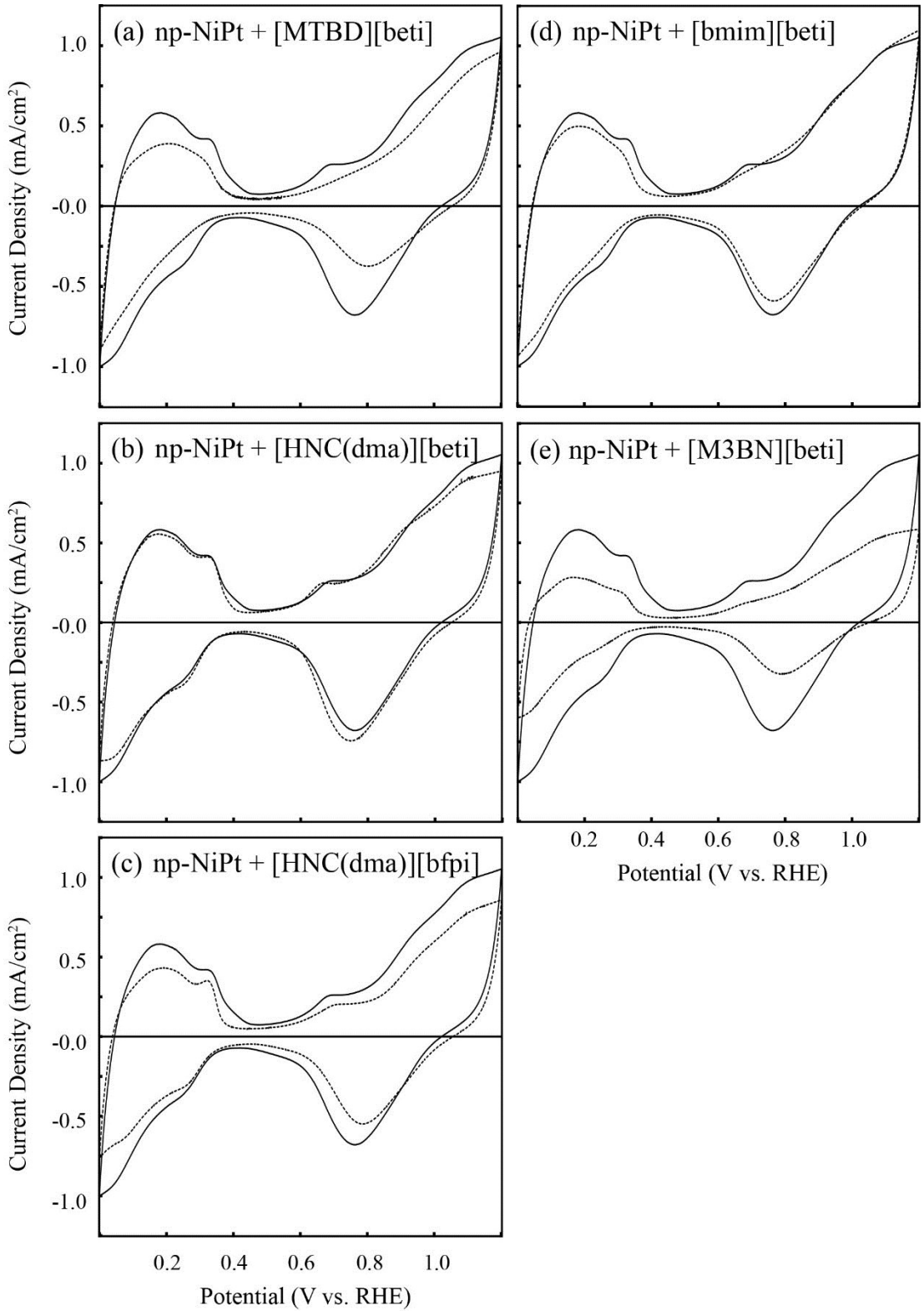

Figure 2.8. Cyclic voltammagrams of np-NiPt/IL composites, conducted in a deoxygenated solution of 0.25 M $HClO_4$ at a flow rate of 15 ml/min with a 5 mV/s sweep rate, after break-in for np-NiPt *(solid line)* and (a) np-NiPt+[MTBD][beti], (b) np-

NiPt+[HNC(dma)][beti], (c) np-NiPt+[HNC(dma)][bfpii], (d) np-NiPt+[bmim][beti], and (e) np-NiPt+[M3BN][beti].

A second factor that can impact the oxygen reduction reaction in our system, apart from oxygen solubility and adsorption behavior, is the water concentration at the metal/IL interface. This concept was not incorporated into any prior modeling because the metal electrode is typically in direct contact with an aqueous electrolyte so the activity of water is always unity. But when adding an intermediate IL layer, we control how much water is soluble in the layer and hence present at the metal/IL interface. While the ILs we used are "hydrophobic", they are known to have some degree of water solubility. As made, these ILs are fully dried to have a water content too low to be accurately measured. Yet, a notable feature of all the measurements performed in this study was that prior to the ability to take a potentiostatic ORR measurement, it was found that the IL layer must first be "broken in." This issue was noted for the thin IL layers used in Refs [1,3,4], but with the thicker IL layers used here, the "break-in" period was more pronounced. Furthermore, it was found here that there are two distinct ways to break-in the composite catalyst, each leading to the same reproducible potentiostatic ORR behavior. First, one can either cycle the potential multiple times in deaerated electrolyte, or run ORR cycles until the voltammetry becomes stable.

As there is clearly no removal of the IL nor any evidence that the IL itself is becoming chemically modified, the dynamic nature of the break-in period suggests that the IL layer and/or IL-metal interface is structurally of compositionally changing after initial catalyst impregnation. The two most plausible explanations are the IL is becoming saturated with water or the structure of the adsorbed water/oxide layer on the catalyst is

different here than in non-IL containing catalysts. We see no evidence of the latter, as described above, so we measured the water solubility in each IL using Karl Fischer titration, letting each equilibrate at room temperature for several days prior to measurement. Results (Table 2.1) show substantial water solubility in all the ILs, as well as a clear variation among them.

Our results suggest that reducing the water solubility also results in significant improvement in the half-wave. For instance, while the [M3BN][beti] composite has an oxygen solubility below that of the surrounding electrolyte, it still yielded the second greatest improvement in half-wave position due to an appreciably lower water solubility. The next greatest improvement is from the [bmim][beti] composite, which has a moderate oxygen solubility, but again a very low water solubility. [HNC(dma)][beti] increases the oxygen concentration relative to the electrolyte, yet absorbs water easily, thus reducing its kinetic control and improvement. We can understand these results from simple chemical kinetics arguments. Increasing the oxygen solubility at the interface pushes reactants into the interface, biasing the reaction to completion; similarly, pulling products away from the interface via hydrophobicity also biases the reaction to completion. Le Chatelier's Principle in action. Of the two primary effects – oxygen solubility and water solubility, oxygen solubility appears to be of greater influence on the kinetic control compared to that of the water solubility.

2.6 Conclusions

We have examined multiple np-NiPt/IL composite systems to determine the ideal properties for ILs that can be used to improve the catalytic activity for the oxygen reduction reaction. Analysis of various physical parameters such as oxygen and water solubility, viscosity, conductivity, and adsorption behavior showed that in the absence of any specific chemical interaction with the catalyst surface, the greatest reduction in ORR overpotential correlates to those materials that combine high oxygen solubility and low water solubility. To date, the IL leading to the greatest reduction in half-wave remains [MTBD][beti] in np-NiPt, because it has the best combination of high oxygen solubility and least water solubility.

References

1. Snyder, J., Fujita, T., Chen, M. W. & Erlebacher, J. Oxygen reduction in nanoporous metal-ionic liquid composite electrocatalysts. *Nat. Mater.* **9,** 904–7 (2010).

2. Damjanovic, a. & Brusic, V. Electrode kinetics of oxygen reduction on oxide-free platinum electrodes. *Electrochim. Acta* **12,** 615–628 (1967).

3. Snyder, J., Livi, K. & Erlebacher, J. Oxygen reduction reaction performance of [MTBD][beti]-encapsulated nanoporous NiPt alloy nanoparticles. *Adv. Funct. Mater.* **23,** 5494–5501 (2013).

4. Chen, C. *et al.* Highly crystalline multimetallic nanoframes with three-dimensional electrocatalytic surfaces. *Science* **343,** 1339–43 (2014).

5. Snyder, J. & Erlebacher, J. The Active Surface Area of Nanoporous Metals during Oxygen Reduction J. Snyder. *ECS Trans.* **41,** 1021–1030 (2011).

6. Luo, H., Baker, G. A., Lee, J. S., Pagni, R. M. & Dai, S. Ultrastable superbase-derived protic ionic liquids. *J. Phys. Chem. B* **113,** 4181–3 (2009).

7. Kissinger, P. T. & Heineman, W. R. *Laboratory Techniques in Electroanalytical Chemistry*. (Dekker, 1984).

8. Evans, R. G., Klymenko, O. V., Saddoughi, S. A., Hardacre, C. & Compton, R. G. Electroreduction of Oxygen in a Series of Room Temperature Ionic Liquids Composed of Group 15-Centered Cations and Anions. *J. Phys. Chem. B* **108,** 7878–7886 (2004).

9. Heller-Ling, N., Poilerat, G., Koenig, J. F., Gautier, J. L. & Chartier, P. DOUBLE CHANNEL ELECTRODE FLOW CELL (DCEFC): APPLICATION TO THE ELECTROCATALYSIS OF THE OXYGEN REDUCTION. *Electrochim. Acta* **39,** 1669–1674 (1994).

10. Anthony, J. L., Anderson, J. L., Maginn, E. J. & Brennecke, J. F. Anion effects on gas solubility in ionic liquids. *J. Phys. Chem. B* **109,** 6366–74 (2005).

11. Tarasevich, M. R., Sadkowski, A. & Yeager, E. *Comprehensive Treatise in Electrochemistry*. (Plenum Press, 1983).

12. Markovic, N. M., Schmidt, T. J., Stamenkovic, V. & Ross, P. N. Oxygen Reduction Reaction on Pt and Pt Bimetallic Surfaces: A Selective Review. *Fuel Cells* **1,** 105–116 (2001).

Chapter 3: Oxygen Reduction Under Proton Diffusion Limited Conditions

3.1 Executive Summary

Instead of varying the oxygen solubility to explore the effect of transport kinetics on the oxygen reduction reaction, alternatively one can vary the proton concentration more easily by tuning the pH of the electrolyte. Here, ORR was studied under proton diffusion-limited conditions in slightly acidic electrolytes - a model system to study the relative transport kinetics of protons and reactants to an electrocatalyst and the relationship between transport and catalytic performance. Electroreduction of small molecules in aqueous solution often competes with the hydrogen evolution reaction (HER), especially if the reaction is driven even moderately hard using a large overpotential.

Using dealloyed nanoporous nickel-platinum (np-NiPt) electrodes, we find the hydrogen evolution reaction can be completely suppressed even at high overpotentials (-400 mV vs. RHE). In addition, the mechanism of oxygen reduction can be changed by using buffered versus unbuffered solutions, suggesting the reaction selectivity is associated with a transient rise (or lack thereof) in the interface pH at the np-NiPt/electrolyte interface. Independently controlling reactant transport to electrocatalyst surfaces at high overpotentials exhibited a surprisingly rich phenomenology that might be

a generalizable strategy to increase activity and selectively during electroreduction reactions.

3.2 Introduction and Literature Review

Previous research, in addition to determining more precisely what factors are crucial in an IL so as to increase the ORR activity, also sought to see the impact transport effects could make on the composite catalyst's performance, specifically by comparing protic versus aprotic ILs[1]. However, because these experiments are performed in acidic aqueous electrolytes, protons are carried with the water through the IL layer in the form of H_3O^+ ions, negating any influence proticity might offer. Furthermore, it is difficult to alter oxygen solubility by a sizeable factor without also significantly changing other physiochemical properties of the IL, making the idea of an experimental control nearly impossible. To probe this question of reactant transport to the catalyst surface in more detail, it become clear employing ILs would cause as many problems as it would alleviate. Instead, we explored an alternative approach by controlling the proton concentration and diffusion necessary for ORR, rather than focusing on O_2 as the variable reactant. By adjusting the pH of the electrolyte, we are able to vary the proton concentration much more easily and by many orders of magnitude more than possible if attempting an allegory with oxygen solubility and various ILs.

ORR is often explored in acidic conditions, where the 4-electron reduction dominates, via the proton mediated mechanism as shown again in Equation 3.1.

$$O_2 + 4H^+ + 4e^- \rightarrow 2H_2O \tag{3.1}$$

At sufficient overpotentials in highly acidic solutions, this mechanism becomes rate-limited by diffusion of oxygen to the catalyst surface due to the abundance of protons. In this scenario, current densities are diffusion limited in the amount of oxygen that can reach the surface of the catalyst to reduce when surrounded by excess protons[2]. The transition between these regimes should take place around pH 3.0, where the concentration of protons is close to the solubility of oxygen in aqueous electrolytes[1,3,4], on order of 1 mM. If proton concentrations are sufficiently depleted oxygen might be reduced via the aprotic water mediated oxygen reduction mechanism often seen in alkaline environments[5],

$$O_2 + 2H_2O + 4e^- \rightarrow 4OH^- \tag{3.2}$$

The standard electrode potential for this reaction is +0.4 V vs. RHE, but it has been observed primarily in basic solutions where it does not compete with or the traditional proton-consuming ORR mechanism (3.1)[6,7]. Another possibility is a 2-electron reduction of oxygen to form peroxide.

$$O_2 + 2H^+ + 2e^- \rightarrow H_2O_2 \tag{3.3}$$

But, peroxide formation has been shown to not be catalyzed by Pt surfaces[8–10] nor Pt_3Ni alloys[11], except slightly at very high overpotentials, coinciding with the onset potential for hydrogen adsorption[9,12]. However np-NiPt is more catalytically active towards the disproportionation of H_2O_2 than its planar counterpart, similar to planar versus np-Au[13].

When using acidic aqueous electrolytes, one is limited to exploring only positive potential regimes due to the hydrogen evolution reaction (HER) occurring below 0.0 V vs RHE,

$$2H^+ + 2e^- \rightarrow H_2 \tag{3.4}$$

Here, the reverse reaction is known as hydrogen oxidation (HOR). These reactions form a basis for all fundamental electrocatalysis and are known to be reasonably active on numerous catalysts[14]. As such, this reaction competes with several electroreduction reactions and controlling the transport of protons would be highly advantageous for enhancing selectivity for each.

In a non-porous electrode at high overpotential, the expected plateau in the HER current has been observed by Auinger et al.[15,16] in deaerated electrolytes, with the associated expectation that the pH should become relatively neutral near the interface. They see reactions that either consume or produce protons or hydroxide can cause drastic changes in interfacial pH, particularly at moderate pH values between 4 to 10. This was determined via mathematical modelling of the Nernst-Planck Equation incorporating a generalized term for the reaction rate for HER/HOR to address the consumption/production of a species at the interface. However, in an electrolyte saturated with oxygen, one expects more complex behavior due to the several possible reactions, as well as multiple species for which to account. In particular, while mechanism 3.1 is expected to be facile, the protons in the pores of the material would become depleted, slowing both HER and ORR.

Further complicating the scenario, in a porous electrode in an intermediate pH environment, predicting catalytic selectivity rapidly becomes complex. There is the possibility of different reactions dominating at the outer surface of the catalytic layer and within the pores due to strong concentration gradients and relatively slow diffusion

kinetics. In this study, we attempt to elucidate the catalytic activity of np-NiPt in this regime, presenting this as a model system for a more general electroreduction scheme in aqueous media with a nanoporous metal catalyst with tunable selectivity. Using these reactions as a basis, if we deplete the proton concentration at the catalyst surface, oxygen should have the opportunity to diffuse into the entirety of the porous electrode, increasing the truly active surface area of the material.

In typical ORR in acidic electrolytes, the mass activity of bulk np-NiPt drops as porosity extends into the bulk. This is because, even at kinetically controlled potentials, oxygen does not diffuse very far into the porous structure before it gets reduced, i.e., the active surface area is itself a function of potential[17]. To develop this concept further, consider a highly active surface (at a highly reducing potential). Oxygen molecules that hit the outer geometric surface get immediately reduced to water. In contrast, at lower overpotentials, oxygen molecules may reflect off the catalyst surface and into the pores many times, sampling a larger "active" surface area before getting reduced (or diffusing back into solution). This geometric effect limits the practical applications for porous electrocatalysts unless the porosity is able to be exploited for a benefit above improving surface area.

Here we show that np-NiPt can also be used to create a "diffusion selective electrocatalyst," whose selectivity can be tuned by controlling the relative diffusional fluxes of reactants to the catalytic surface. We observe apparent suppression of hydrogen evolution via such a mechanism in a potential regime where the competition of hydrogen evolution traditionally precludes the study of many electroreductions. We employ this novel catalysis scheme to study the electroreduction of molecular oxygen at greater than

1.5 V overpotentials (-0.4 V vs. RHE) in aqueous media for the first time. Other small molecules, namely carbon dioxide and nitrogen, could be selectively reduced by similar methods employing a corresponding nanoporous metal catalyst and proper understanding of the diffusion of reactants to the surface and within the porous catalyst layer.

3.3 Experimental Methods

Nanoporous NiPt was formed through electrochemical dealloying as previously described[1]. Briefly, a precursor alloy of $Ni_{77}Pt_{23}$ is dealloyed by repeated cycling of the potential from 0.0 – 1.2 V vs. RHE in 0.1 M sulfuric acid. The depth of dealloying was measured using hydrogen under potential deposition (H_{UPD}) to determine the effective surface area, which was then normalized by the geometric surface area, yielding the roughness factor, $R_f \sim 150$.

Solutions of 0.1 M sodium sulfate (Sigma Aldrich, ACS reagent ≥ 99.0%, anhydrous) were buffered to the appropriate pH with 0.1 M sulfuric acid (J.T. Baker, 95-98%) and 0.1 M sodium hydroxide (Fisher Scientific, 98.7%), measured with a Mettler-Toledo SevenExcellence pH meter. Solutions of 0.1 M potassium perchlorate (Acros Organics, 99+%) were buffered in a similar manner using 0.1 M perchloric acid (Sigma Aldrich, 70%) and 0.1 M potassium hydroxide (Fisher Scientific, Certified ACS). Electrolytes were prepared with Millipore Milli-Q water. Glassware was cleaned by soaking in a solution of NoChromix (Godax Laboratories, Inc.) and sulfuric acid overnight.

Oxygen reduction activity was measured using a Gamry Interface 1000 Potentiostat and a Pine Instruments Rotating Disk Electrode (RDE) apparatus. All measurements were made potentiostatically. That is, data points were taken every 50 mV by holding the samples at a fixed potential and then recording the steady state current, starting at higher potentials and stepping negatively, unless specifically stated otherwise.

A Pine Instruments Rotating Ring Disk Electrode (RRDE) assembly with platinum ring insert (99.99%) was used for all RRDE measurements. The Pt ring electrode was fixed at 1.1 V vs RHE, where the oxidation of H_2 is diffusion limited, but where O_2 in the electrolyte will not readily reduce. The np-NiPt disk is held at each potential for 16 min before stepping more negatively.

3.4 Results and Discussion

3.4.1 Suppression of HER

We begin by comparing catalysis behavior in deaerated and oxygen-saturated solutions to identify currents associated with HER and ORR. Figure 3.1 depicts potentiostatic (steady-state) HER and ORR currents using np-NiPt electrocatalysts in buffered sulfate solutions for pH ranging from 1.0 to 5.0.

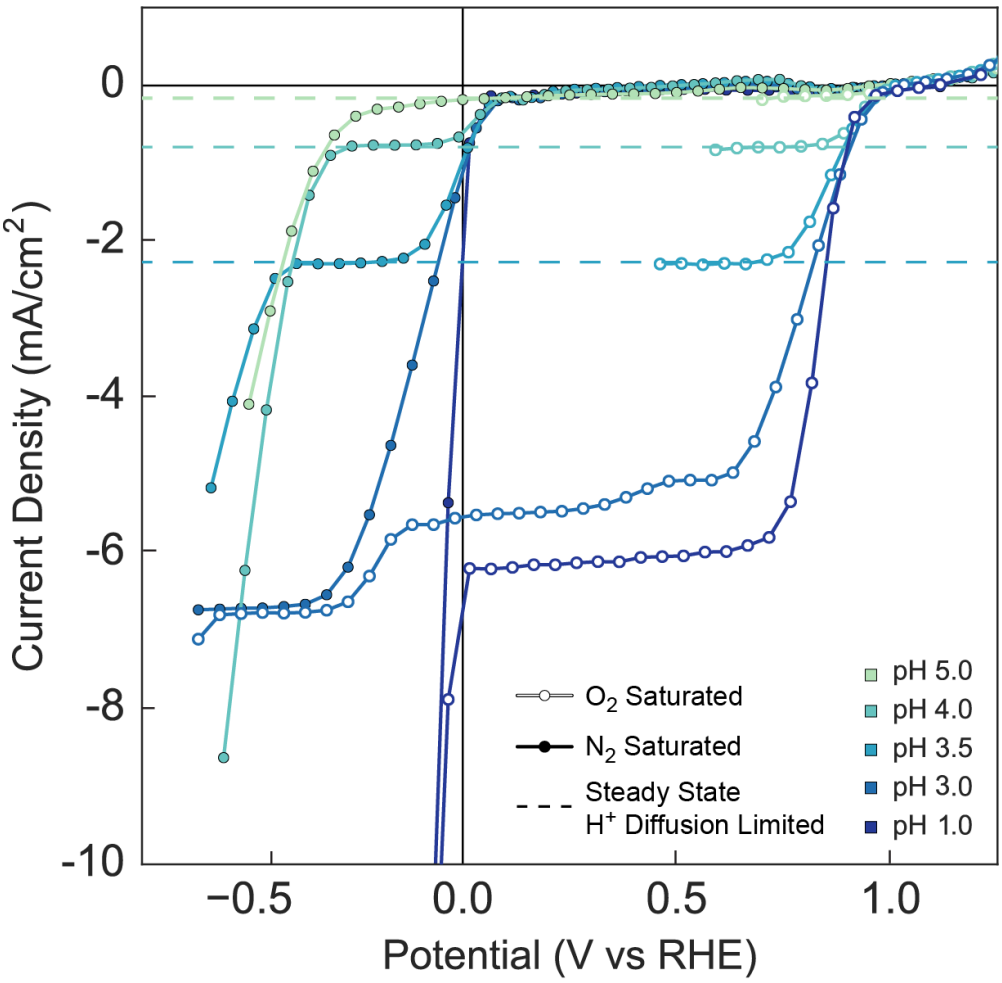

Figure 3.1. Differences in steady-state ORR and HER current densities as they vary with pH. *(closed circles)*: HER current density versus the reversible hydrogen electrode (RHE) potential in N_2 saturated 0.1 M Na_2SO_4 electrolyte; *(open circles)* ORR current density versus RHE in O_2 saturated 0.1 M Na_2SO_4 electrolyte. All data were taken at 1600 rpm, sweeping from positive to negative potentials. *(dashed lines)* proton-diffusion limited current densities for pH 3.5, 4.0, and 5.0.

For deaerated electrolytes, the high proton concentration results in rapid hydrogen evolution below 0.0 V vs RHE at pH 1.0. Yet, pH greater than 3.0 allow for quantifiable HER activity, resulting in plateaus of current density, limited by the rate of protons reaching the catalyst surface. This is consistent with prior research by Strmcnik et al.,

demonstrating these are pure diffusion limited currents at high overpotentials controlled by the transport of H_3O^+ ions to the catalyst surface[10,14], with an additional reduction seen below -1.0 V due to water dissociation.

The ORR currents are measured using the same parameters in an oxygen saturated solution. Snyder et al.[4] used a Pt microdisc protocol to determine the oxygen solubility in dilute perchloric acid and found for these electrolytes to have an oxygen solubility of approximately 1 mM. Assuming this value is comparable to the dilute electrolytes used here, a pH 3.0 solution will have the proton and oxygen concentrations nearly equal. Above pH 3.0, there is a transition from oxygen flux to proton flux limiting the reaction rate, and it becomes evident from Fig. 3.1 that the current densities for ORR align perfectly with the HER currents measured in nitrogen-saturated environments for higher pH solutions, implying ORR is truly acting under proton diffusion limited circumstances.

Given the facility with which np-NiPt catalyzes HER, it is surprising that when examining potentiostatic ORR currents at moderate pH (pH 4.0) over np-NiPt we observed that ORR remains active via the proton diffusion limited acidic mechanism to potentials as low as -0.4 mV vs. RHE (shown explicitly in Figure 3.3). While it appears we are sustaining ORR activity at extreme overpotentials, and even into the HER regime, it is unclear if we are truly suppressing hydrogen evolution or rather seamlessly transitioning from ORR to HER below 0.0 V.

To explore this, we conducted rotating ring disk electrode (RRDE) experiments, with a ring of Pt surrounding the np-NiPt disk, forcing products being formed at the disk will react at the ring while rotating, a schematic shown in Figure 3.2. RRDE experiments allow for reversible reaction products to be swept away from the disk as it rotates, while

the ring is maintained at a potential that can provide some insight on the products being formed. As an example, in our case, if we are evolving hydrogen below 0.0 V at the disk, we can set the ring potential to a value where the reverse reaction would proceed.

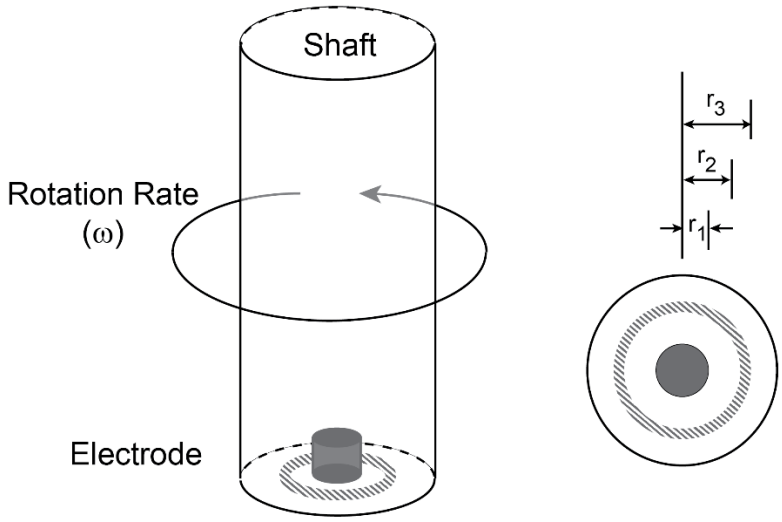

Figure 3.2. Schematic representation of a Rotating Ring Disk Electrode (RRDE) apparatus.

If below 0.0 V we are reducing oxygen, the product will simply be water, and therefore undetectable at the ring in an aqueous electrolyte. However, if we are evolving hydrogen, with the ring to 1.1 V vs RHE, then the Pt ring will oxidize the H_2 being produced, generating a positive current. This ring potential was chosen so that the hydrogen oxidation reaction (HOR) will be in the diffusion limited regime while set to a value where the oxygen dissolved in the electrolyte is not at risk of being reduced by the

Pt. Yet, there is a theoretical collection efficiency that can be calculated to determine how much of a product from the disk can be captured by the ring electrode. This value is dependent only upon the diameters of the ring and disk electrodes, and for our system is equal to 25.5%, meaning only about a quarter of the H_2 being produced at the disk can be detected at the ring electrode. This does not account for any product that further reacts within the aqueous electrolyte, making the true efficiency even lower. Hence, since we are only producing about 1 mA/cm^2 of current due to hydrogen evolution in a pH 4.0 solution, the measured ring current will be small. As such, we performed a control in a deaerated solution to ensure these are measureable differences.

Figure 3.3 compares the disk current density to the ring current density, plotted in reference to the potential of the np-NiPt disk, conducted in oxygen-saturated electrolytes at pH 4.0, in addition to nitrogen-saturated electrolyte control. For nitrogen-saturated electrolytes, there is a distinct increase in the ring current below 0.0 V associated with HER occurring at the disk, illustrating this scheme will effectively measure any HER products. Alternatively, in an oxygen saturated sulfate solution, there is no hydrogen produced that could be detected via hydrogen oxidation observed below 0.0 V, nor hydrogen evolution was observed as bubbles during the course of the experiment, indicating that HER is being suppressed in favor of ORR. These are potentiostatic experiments, wherein current for each potential was measured after a suitable time for the current density to reach steady state. In this case some initial hydrogen evolution may occur in the transient regime, but it is fully suppressed once the current reaches a constant value.

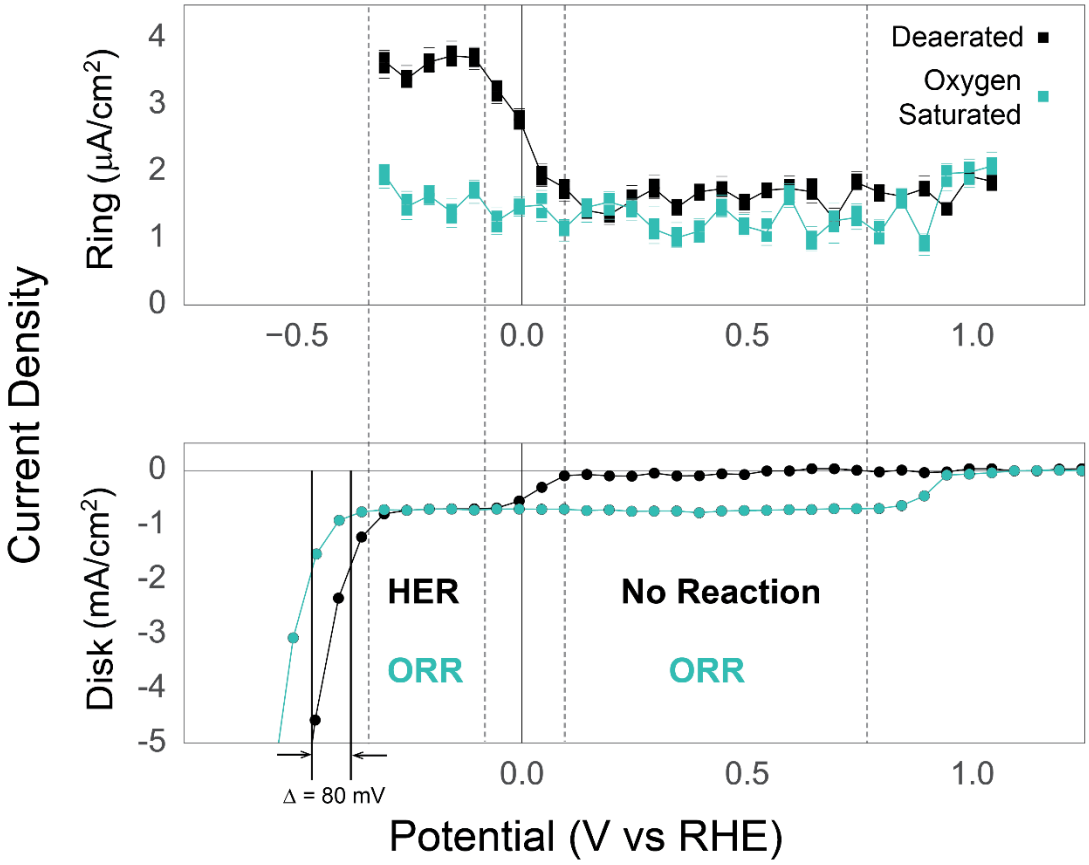

Figure 3.3. Potentiostatic ORR current densities and simultaneous ring current densities in 0.1 M Na_2SO_4 electrolytes at pH 4.0, in deaerated (N_2 saturated) and O_2 saturated conditions at 1600 rpm versus the disk potential. The Pt ring was held at a potential of 1.1 V vs RHE, while the np-NiPt disk was stepped the negatively in potential with 16 min step holds at each potential until the current reached a steady state. Note the rise in ring current below 0.0 V vs. RHE in deaerated electrolyte, indicating HOR at the ring, and that this is not observed in oxygen-saturated electrolyte. Notice also the shift in the onset of water reduction in oxygen-saturated electrolyte compared to oxygen-saturated electrolyte.

Upon further examination of the disk current densities measured in Fig. 3.3, it is apparent there is a shift in the onset potential for water reduction between the deaerated and oxygen saturated solutions occurring near -0.5 V. When oxygen is being reduced, there is a shift of 80 mV in this onset relative to the deaerated control, corresponding to a

shift in pH relative to RHE from 4.0 to 5.3. This alludes to some formation of hydroxide in the transient behavior that leads to a variation in the surface pH.

As a note, the catalyst surface was physically unchanged throughout the experiments in either electrolyte solution. Figure 3.4 shows a representative cyclic voltammogram of the np-NiPt surface before and after performing an extended ORR experiment with no significant differences.

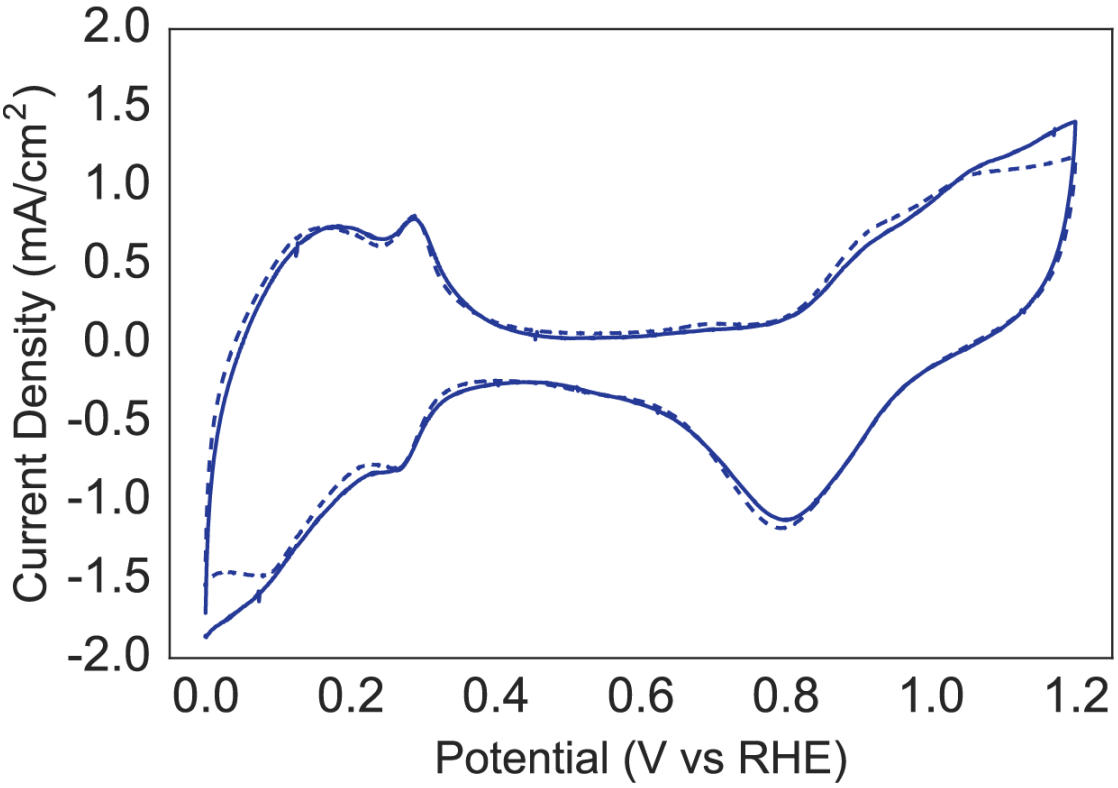

Figure 3.4. Cyclic voltammograms of np-NiPt before *(solid)* and after *(dashed)* ORR measurements in 0.1 M H_2SO_4 using a sweep rate of 5mV/s. (Approximately 72 hours of measurement).

3.4.2 Electrolyte Effects

Sodium sulfate acts as a buffer to minimize pH variations in the electrolyte, so to study whether buffering effects contribute to the suppression of hydrogen evolution we compare our results to experiments performed with a perchlorate-based electrolyte. Simply put, buffers resist a change in pH upon a small addition of acid or base in order to maintain a chemical equilibrium. Since perchloric acid is such a strong acid, it has relatively little buffering ability compared to sulfuric acid solutions. In perchlorate-based solution with pH 4.0, significantly different ORR behavior was observed compared to the corresponding experiment in sulfate solution, as shown in Figure 3.5.

At lower overpotentials, both electrolytes promote proton diffusion limited ORR via mechanism (3.1). This is because under proton diffusion control, mechanism 3.1 is rate limited by the 1-electron reduction of a proton. To determine the number of electrons transferred experimentally, one can use known convective diffusion equations. For an RDE apparatus, substituting the appropriate boundary conditions, this simplifies to the Levich equation, relating limiting current density $i_{\lim}$ to physical constants as follows,

$$i_{\lim} = (0.620)nFD^{2/3}\omega^{1/2}\nu^{-1/6}C \tag{3.5}$$

where ω is the rotation rate of the electrode, ν is the kinematic viscosity of the solution, F is Faraday's constant, D, C are the diffusion coefficient and concentration of species limiting the reaction, and n is the number of electrons transferred to the rate-limiting species. There are more evolved and improved forms available, but for most applications, Equation 3.5 is deemed appropriate[25].

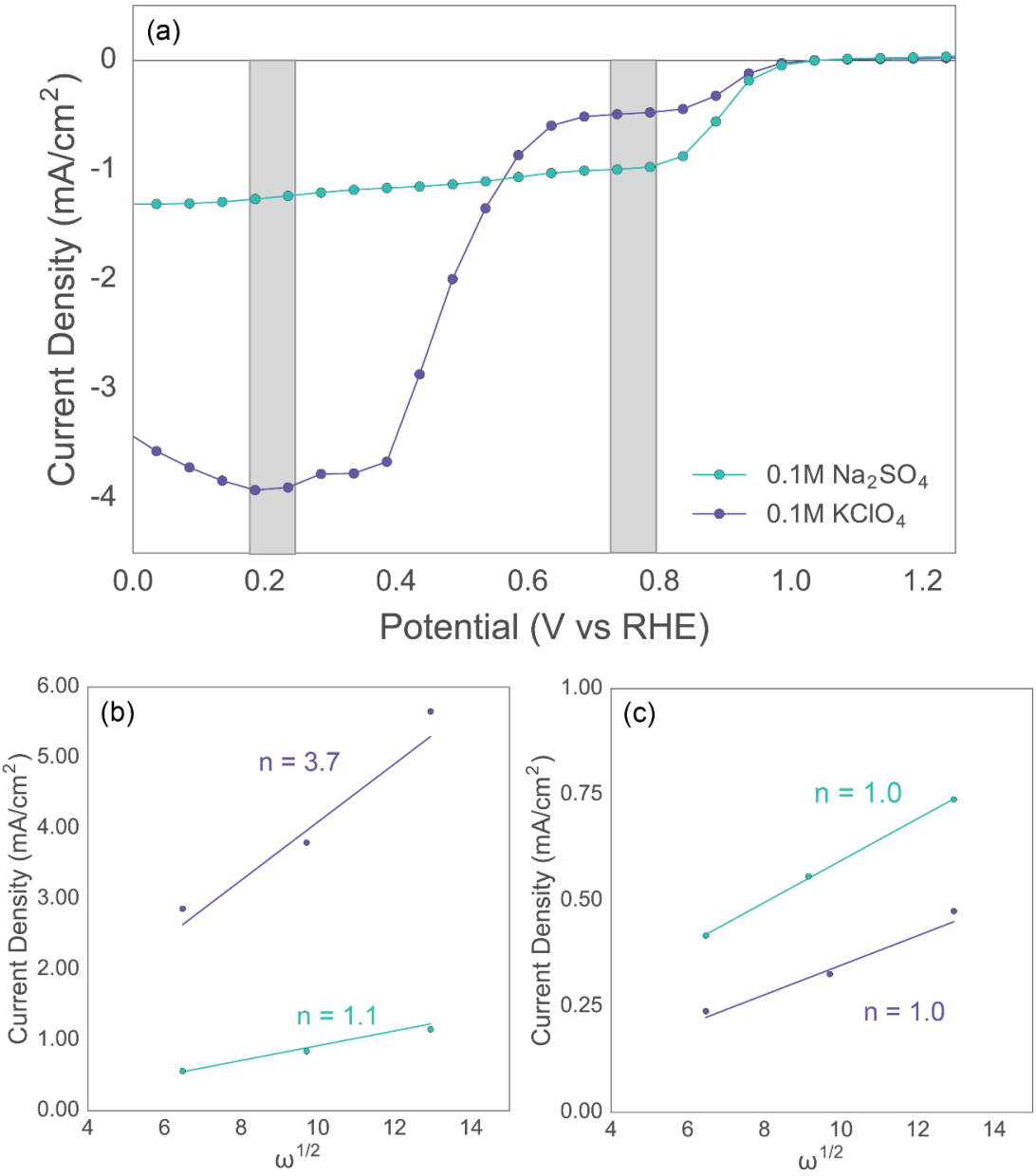

Figure 3.5. Comparison of electrolyte effects on ORR behavior at steady state (a). Below in (b) and (c) are Levich plots and calculated number of electrons transferred for each electrolyte at the potential ranges as marked in (a).

First performing these measurements in a deaerated solution at HER potentials for several rotation rates, we are able to determine the diffusion coefficient, D, for protons

in a moderate pH solution: for a pH 4.0 solution of 0.1 M sodium sulfate, D_{H^+} is equal to $3.65\text{x}10^{-4}$ cm^2/s. Using the same protocol, we determined D_{H^+} of perchlorate-based solutions to be $1.43\text{x}10^{-4}$ cm^2/s at pH 4.0, less than half that in sulfate solutions (values organized in Table 3.1). Using the calculated diffusion coefficient to analyze currents measured during ORR at the same pH, Levich analysis is consistent with one electron transfer for the diffusion limited reactant, confirming that both rates are controlled by the diffusion of protons. Small variations in pH may contribute to the slight discrepancies in current densities between 0.5 and 1.0 V, but they are primarily caused by different effective diffusivities of protons in buffered vs non-buffered electrolytes.

However, the different electrolytes show differing behavior at high overpotentials, where np-NiPt in perchlorate clearly exhibits a mechanism limited by 4-electron reduction of oxygen, as confirmed by the Levich equation (3.5). Using values of *C* and *D* for oxygen solubility and diffusivity respectively from Ref [4], the calculated number of electrons transferred, *n*, is about 4. Substituting *C* and *D* values for hydrogen as previously determined, yields *n* significantly greater than 1, which makes no physical sense for proton limited reactions. This implies that the ORR is no longer limited by the diffusion of protons to the catalyst, but since the solution concentration of protons remains relatively unchanged, mechanism 3.1 can no longer explain the current density observed. Thus the perchlorate-based solution appears to strongly favor the proton-free oxygen reduction mechanism in Eq. 3.2, while in sulfate-based media this mechanism is not observed in steady-state measurements. This mechanistic change indicates that while activity is a property largely dictated by the catalyst, the matters of selectivity and product formation are influenced by electrolyte choice. In fact, in this extreme case there

appears to be a total shift from one reaction to another caused exclusively by the electrolyte.

Table 3.1 Measured and calculated values used in the Levich analysis. * *denotes values assumed in Eq 3.5 calculations, + indicates literature values adapted from Ref [4].*

Sample	D_{H+} *(cm^2/s)*	C_{H+} *(mol/cm^3)*	D_{O2} *(cm^2/s)*	C_{O2} *(mol/cm^3)*	*n*
Sulfate					
N_2: HER	3.7×10^{-4}	1.0×10^{-7} *	--	--	1.0 *
O_2: 0.75V			--	--	1.04
O_2: 0.25V			--	--	1.11
Perchlorate					
N_2: HER	1.4×10^{-4}	1.0×10^{-7} *	--	--	1.0 *
O_2: 0.75V			--	--	1.00
O_2: 0.25V			1.9×10^{-5} +	1.2×10^{-6} +	3.70

3.4.3 Transient Behavior

To understand the behavior discussed above, it is necessary to address not only the steady-state results, but also the time-dependent evolution of the system to that steady state. At short times, perchlorate and sulfate solutions appear to have identical behaviors, but it is clear from the potentiostatic measurements that the two electrolytes behave differently over a longer time frame. The perchlorate-based system reaches steady state quite quickly with a simple exponential-type decay across the entire potential range as illustrated Figure 3.6, where the measured current is plotted versus time. In sulfate solution, the decay behavior is the same over the range where the ORR is dominated by the proton consuming mechanism, but in the range where ORR shifts reaction mechanism in the perchlorate solutions to a 4-electron reduction, there is a longer transient in sulfate solutions that cannot be explained by double layer charging, with the current decaying

slowly back to the proton-limited ORR current between several potential steps and over the course of more than an hour before reaching the final steady state behavior. Thus, when sufficient time is allowed for the transient currents to dissipate, the result is the same as shown in Figure 3.3 – proton diffusion limited reduction of oxygen suppressing hydrogen evolution at large overpotentials.

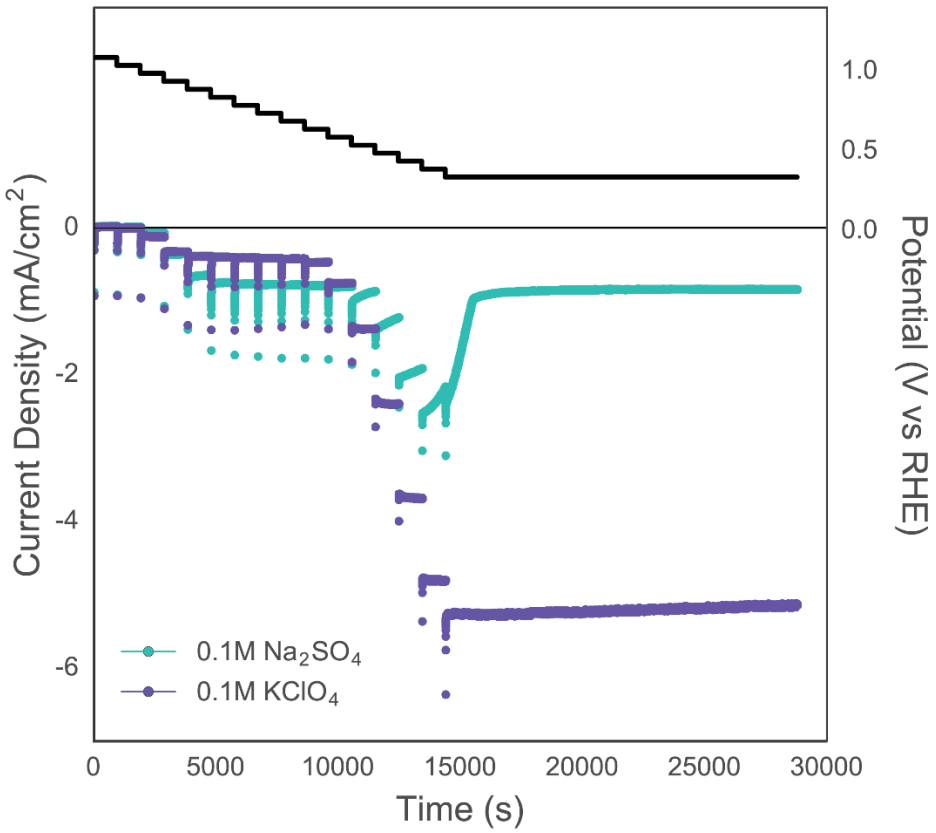

Figure 3.6. Potentiostatic ORR current densities in 0.1 M Na_2SO_4 *(green)* and 0.1 M $KClO_4$ *(purple)* electrolytes at pH 4.0 at 1600 rpm versus time. Shown in black is the potential versus the reversible hydrogen electrode (RHE) applied for at each time. Note, the final time step corresponds to a potential near 0.3 V vs RHE that was held for an extended time. This was done so as to ensure no complications associated with the competing HER below 0.0 V.

The onset of the transient period in sulfate matches the potential where the proton-free ORR mechanism becomes operational, but we see no evidence of this mechanism at steady state, suggesting that the transient current is associated with self-limiting hydroxide-evolving ORR. This mechanism drives a strong pH change at the catalyst surface which would work to hamper its kinetics, but if this is the method by which it shuts down, the mechanism would be expected to operate more robustly in a buffered solution where local pH changes are mitigated. The fact that the opposite behavior is observed suggests that the proton-free ORR mechanism is limited kinetically in sulfate-based media rather than strictly due to a solution buffering effect. The long duration of the transient could be associated with the porous nature of the catalyst providing a large surface area that requires passivation before the mechanistic change takes place.

In support of this hypothesis, the transient behavior shown in Figure 3.6 was observed only the first time a long-duration ORR experiment was run on the catalyst, with subsequent runs displaying a much shorter transient period, as shown in Figure 3.7. Operating the same catalyst in a strongly acidic electrolyte where the reaction is diffusion-limited by oxygen rather than protons can mitigate this behavior. After this "recovery" step, the transient behavior returned to that originally observed when the same catalyst was transferred back to mildly acidic sulfate solution. This suggests an additional control of the selectivity of the catalyst, as well as reversibility.

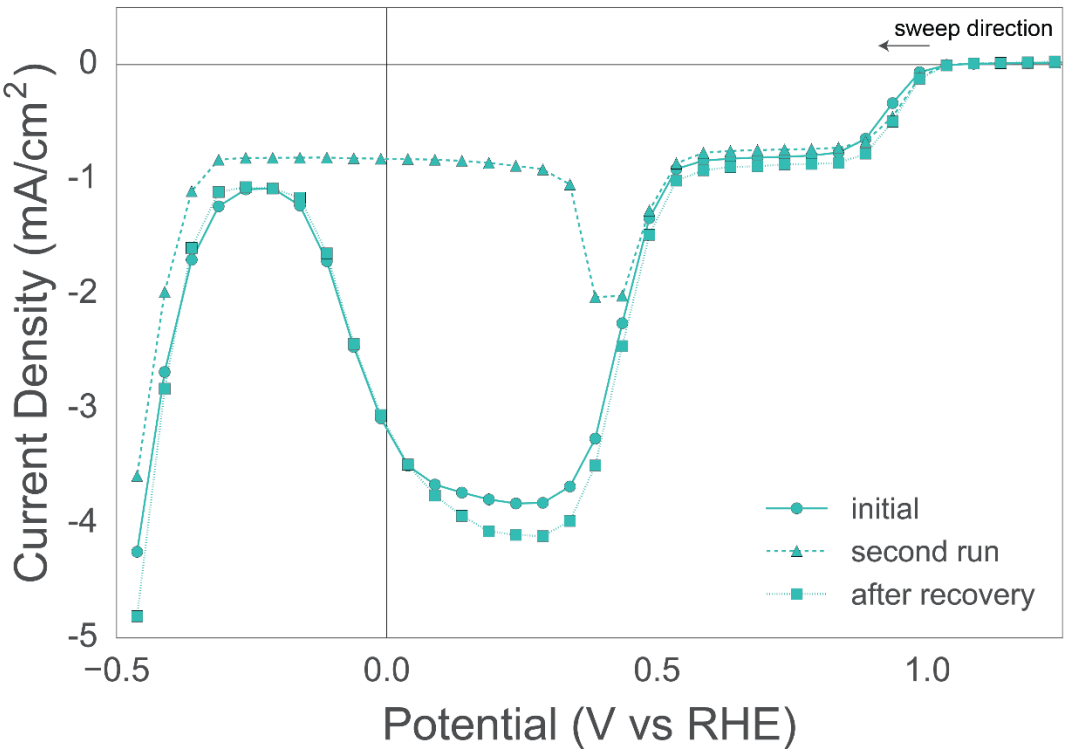

Figure 3.7. Transient behavior of oxygen reduction current vs. potential. When ORR is measured initially in 0.1 M Na_2SO_4 electrolytes *(solid line)*, there is a significant transient measured beginning near 0.5 V vs RHE, resulting in an apparent current wave seen until the potential drops below 0.0 V. After multiple sweeps, this transient becomes less severe and recovers to steady state much more rapidly *(dashed line);* eventually, this behavior is not seen at all (as in Figure 3.3). After holding the np-NiPt in a highly acidic 0.1 M H_2SO_4 solution at 0.25V vs RHE for several hours, the original behavior can be recovered after this "recovery" step as shown *(dotted line).*

3.5 Conclusions

This work presents an interesting advance in the application of nanoporous catalysts. While porous catalysts have been shown to have high activity for a variety of reactions similar to other metal-based electrocatalysts, the porous nature of the catalytic surface has

not been explicitly utilized. By careful control of diffusion rates to the catalytic surface, oxygen reduction has been carried out instead of hydrogen evolution in a potential regime where HER usually dominates, and on a catalyst that is shown to also be highly active for HER. Furthermore, by changing the electrolyte solution the dominant reaction was once again drastically changed and proton-free oxygen reduction appears to take place preferentially at steady state. The transient behavior observed provides another interesting potential application, because the duration of the transient combined with the ability to recondition the catalyst mean reactions that occur only transiently could be performed with acceptable efficiency by cycling the electrolyte environment of the catalyst.

This collection of results opens the door for a new generation of multifunctional electrocatalysts where multiple reactions can be performed with high selectivity and excellent catalytic activity over the same catalyst surface. Reactions could be cycled or performed alternately in the same electrochemical system and even at the same potential by controlling the electrolyte environment, the fluxes of reactant species to the interface and taking full advantage of the porous nature of the catalyst material.

References.

1. Benn, E., Uvegi, H. & Erlebacher, J. Characterization of Nanoporous Metal-Ionic Liquid Composites for the Electrochemical Oxygen Reduction Reaction. *J. Electrochem. Soc.* **162,** H759–H766 (2015).

2. Adzic, R. in *Electrocatalysis* 197–242 (1998).

3. Battino, R., Rettich, T. R. & Tominaga, T. The Solubility of Oxygen and Ozone in Liquids. *J. Phys. Chem. Ref. Data* **12,** 163–178 (1983).

4. Snyder, J., Fujita, T., Chen, M. W. & Erlebacher, J. Oxygen reduction in nanoporous metal-ionic liquid composite electrocatalysts. *Nat. Mater.* **9,** 904–7 (2010).

5. Kinoshita, K. in *Electrochemical Oxygen Technology* 19–107 (Wiley-Interscience, 1992).

6. Gasteiger, H. a & Ross, P. N. Oxygen Reduction on Platinum Low-Index Single-Crystal Surfaces in Alkaline Solution: Rotating Ring DiskPt(hkl) Studies. *J. Phys. Chem.* **100,** 6715–6721 (1996).

7. Ramaswamy, N. & Mukerjee, S. Fundamental Mechanistic Understanding of Electrocatalysis of Oxygen Reduction on Pt and Non-Pt Surfaces: Acid versus Alkaline Media. *Adv. Phys. Chem.* **2012,** 1–17 (2012).

8. Damjanovic, a. & Brusic, V. Electrode kinetics of oxygen reduction on oxide-free platinum electrodes. *Electrochim. Acta* **12,** 615–628 (1967).

9. Nenad M. Markovic, Gasteiger, H. a. & Ross, P. N. Oxygen Reduction on

Platinum Low-Index Single-Crystal Surfaces in Sulfuric Acid Solution: Rotating Ring-Pt(hkZ) Disk Studies. *J. Phys. Chem.* **99,** 3411 (1995).

10. Sepa, D. B., Vojnovic, M. V. & Damjanovic, A. Reaction intermediates as a controlling factor in the kinetics and mechanism of oxygen reduction at platinum electrodes. *Electrochim. Acta* **26,** 781–793 (1981).

11. Ferreira de Morais, R., Franco, A. A., Sautet, P. & Loffreda, D. How Does the Surface Structure of Pt-Ni Alloys Control Water and Hydrogen Peroxide Formation? *ACS Catal.* acscatal.6b00842 (2016). doi:10.1021/acscatal.6b00842

12. Katsounaros, I. *et al.* Hydrogen peroxide electrochemistry on platinum: towards understanding the oxygen reduction reaction mechanism. *Phys. Chem. Chem. Phys.* **14,** 7384 (2012).

13. Zeis, R., Lei, T., Sieradzki, K., Snyder, J. & Erlebacher, J. Catalytic reduction of oxygen and hydrogen peroxide by nanoporous gold. *J. Catal.* **253,** 132–138 (2008).

14. Strmcnik, D. *et al.* Improving the hydrogen oxidation reaction rate by promotion of hydroxyl adsorption. *Nat. Chem.* **5,** 300–306 (2013).

15. Auinger, M. *et al.* Near-surface ion distribution and buffer effects during electrochemical reactions. *Phys. Chem. Chem. Phys.* **13,** 16384–16394 (2011).

16. Katsounaros, I. *et al.* The effective surface pH during reactions at the solid-liquid interface. *Electrochem. commun.* **13,** 634–637 (2011).

17. Snyder, J. & Erlebacher, J. The Active Surface Area of Nanoporous Metals during

Oxygen Reduction J. Snyder. *ECS Trans.* **41,** 1021–1030 (2011).

18. Cullen, D. a. *et al.* Linking morphology with activity through the lifetime of pretreated PtNi nanostructured thin film catalysts. *J. Mater. Chem. A* **3,** 11660–11667 (2015).

19. McCue, I. *et al.* Apparent inverse Gibbs-Thomson effect in dealloyed nanoporous nanoparticles. *Phys. Rev. Lett.* **108,** 1–5 (2012).

20. Snyder, J., Mccue, I., Livi, K. J. & Erlebacher, J. D. Structure / Processing / Properties Relationships in Nanoporous Nanoparticles as Applied to Catalysis of the Cathodic Oxygen Reduction Reaction Structure / Processing / Properties Relationships in Nanoporous Nanoparticles as Applied to Catalysis of the Ca. (2012). doi:10.1021/ja3019498

21. Li, X. *et al.* Dealloying of noble-metal alloy nanoparticles. *Nano Lett.* **14,** 2569–2577 (2014).

22. Baldizzone, C. *et al.* Stability of Dealloyed Porous Pt/Ni Nanoparticles. *ACS Catal.* 5000–5007 (2015). doi:10.1021/acscatal.5b01151

23. Snyder, J., Livi, K. & Erlebacher, J. Oxygen reduction reaction performance of [MTBD][beti]-encapsulated nanoporous NiPt alloy nanoparticles. *Adv. Funct. Mater.* **23,** 5494–5501 (2013).

24. Wang, D., Zhao, P. & Li, Y. General preparation for Pt-based alloy nanoporous nanoparticles as potential nanocatalysts. *Sci. Rep.* **1,** 1–5 (2011).

25. Bard, A. J. & Faulkner, L. R. *Electrochemical Methods*. (John Wiley & Sons,

1980).

Chapter 4. Control of Reactivity with Sequential Electrocatalysts

4.1 Executive Summary

For over a century, ammonia has been produced industrially through the Haber-Bosch process, rapidly becoming one produced in some of the largest quantities in the chemical industry. While this process has been made more efficient through enhanced understanding of catalyst surface structure and better temperature and pressure control, it still consumes a great deal of energy.

Here, we discuss the design and results of a novel flow reactor which serves as a proof of concept for part of a proposed electrochemical ammonia synthesis reactor. In this study, we oxidize and evolve hydrogen at sequential electrodes of nanoporous nickel-platinum (np-NiPt) in aqueous solutions with varied proton concentrations in a flow cell geometry. Using aqueous electrolytes poses a problem at the negative potentials that will be required for the formation of ammonia due to decomposition of water at these same negative potentials. To avoid water reduction, an ionic liquid (IL) stable at extreme negative potentials was synthesized and used as an electrolyte for the successful sequential oxidation and evolution of hydrogen.

4.2 Introduction and Literature Review

4.2.1 Current Processing Techniques and Challenges

The United States alone generated $8.3x10^{12}$ g of ammonia fertilizer in 2010, the last year with reported statistics, signifying ammonia as a crucial chemical in today's world[1]. While 20% of industrially produced ammonia is used in a wide array of industries such as plastics, fibers, explosives, dyes, and pharmaceuticals, the remaining 80% is used in the production of fertilizer, which supports nearly half of the world's population[2,3]. Figure 4.1 illustrates this point, demonstrating the differences in population pre-and post-industrial synthesis of ammonia and its use as fertilizer.

The production of ammonia has changed very little since its discovery in the early twentieth century, by Fitz Haber, later scaled to industrial proportions by Carl Bosch, earning both a Nobel Prize. The approach, aptly named the Haber Bosch process, simply mixes nitrogen and hydrogen gases at high temperatures (~500 ˚C) and pressures (150-300 bar) using an iron based catalyst to drive the reaction[4]. A great deal of energy is necessary in order to break nitrogen apart to react and form ammonia, following the formula,

$$N_2 + H_2 \rightarrow NH_3 \tag{4.1}$$

A sizeable drawback to this process is the source of hydrogen, which is commonly derived from steam reforming of natural gas, resulting in large amounts of carbon dioxide released as a byproduct plus its reliance on nonrenewable resources[5]. By some estimates, 5% of the world's use of natural gas goes to the production of fertilizer[6], but is subject to

pricing in the natural gas market, which fluctuates significantly leading to instabilities in food costs[2]. There is thus both a strategic and a humanitarian incentive to reduce the quantity of natural gas in the synthesis of ammonia, in addition to the environmental need to reduce the carbon dioxide emissions created along the way[7].

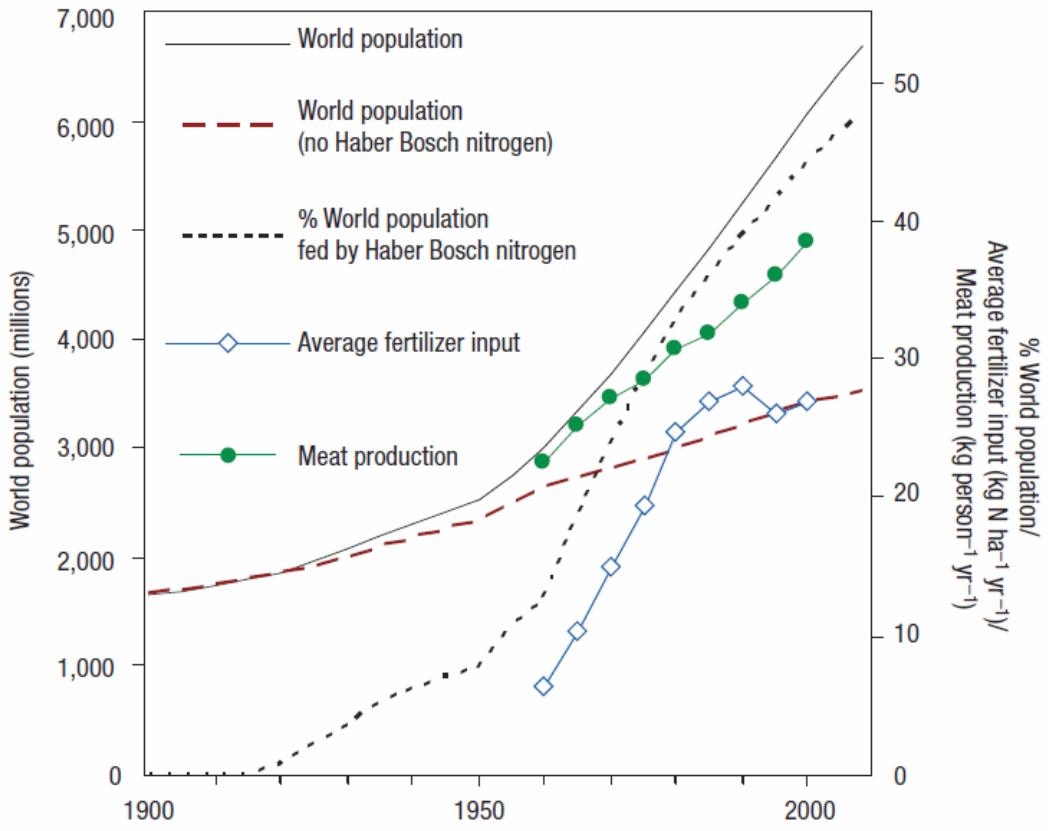

Figure 4.1. Trends in human population and nitrogen use over the last century. Of the total world population *(solid line)*, an estimate is made of the number of people that could be sustained without reactive nitrogen produced industrially *(long dashed line),* also expressed as a percentage *(short dashed line)*. Increase in average fertilizer use and increase in per capita meat production are also shown. *(Adapted from Ref [2])*

Yet, there is a reason very little progress has been made to this method with the exception of some minimal improvements in catalyst, since it was discovered a century

ago. It is very difficult to reduce nitrogen, and the Haber-Bosch process does so in a rather cost-effective manner. A different approach is to electrochemically synthesize ammonia, the limiting step still dependent upon reducing nitrogen, but with the ability to do so at lower temperatures and pressures than current technologies allow. However, attempts using this technique report minimal yields thus far, and even when higher temperatures and pressures are employed to improve reaction kinetics, nothing reaches the current efficiency of Haber-Bosch processing[8].

Rather than hydrogenating the nitrogen molecules (an associative mechanism), the Haber Bosch method uses a dissociative mechanism to form ammonia, i.e. the hydrogen and nitrogen bonds in each are broken prior to reacting with one another. While the overall reaction in Eq. 4.1 is exothermic, the kinetics are slow enough that high temperatures are required to achieve substantial yields. However, this results in lower conversion since the equilibrium is shifted towards the reactants, which can be remedied by increasing the pressure of the system. Theoretical calculations for electrochemical methods using this type of mechanism would require a negative potential bias near -1.0 to -1.5 V vs the standard hydrogen electrode, where competition with hydrogen evolution and water reduction reactions becomes a major concern[9–11].

Transition metal complexes have reduced nitrogen at ambient conditions, however for the catalysts employed thus far, the kinetics are too hindered for practical applications. Most results to date form hydrogen gas much more readily than ammonia[12–15], but additional insight into the mechanism of the process would likely result in superior catalysts and reaction schemes.

Our earlier scheme of using an ionic liquid as a barrier layer between an aqueous electrolyte and a catalytic electrode, which worked well for oxygen reduction, will probably not be sufficient for nitrogen reduction. By adjusting the pH of the electrolyte, one can observe diffusion-limited transport of protons - this strategy works because the proton concentration in aqueous electrolyte can be reduced to levels below the solubility limit of oxygen in either the same electrolyte. Yet, at such negative potentials we would also be competing with the reduction of water, making aqueous electrolytes impossible to work with due to the high solubility levels in most ILs. However, if we eliminate an aqueous electrolyte altogether and instead use the IL itself as the electrolyte, we will have the ability to control the reactant concentrations and independently manipulate the fluxes of nitrogen and protons, either from hydrogen gas or water.

4.2.2 Implementation of Flow Reactor

Figure 4.2 details a schematic of our proposed system for the reduction of nitrogen to ammonia. Simply, we have an electrochemical flow cell filled with IL electrolyte, where variable compositions of reactants will be added to the IL upstream from a series of sequential catalytic electrodes. Each electrode can be independently set to a determined potential that will be used to modify the relative concentrations of reactants in the IL. The hydrogen source can be either hydrogen gas (for simplicity) or water, but ultimately we will employ three working electrodes:

I. The first electrode the reactants pass is meant to dissociate water into hydrogen gas and hydroxide, the latter of which will be removed, but has no impact on the nitrogen gas passing through.

II. The nitrogen and hydrogen gases then travel to the second electrode that is set to a potential to split the hydrogen gas into protons.

III. The final electrode will be set to a highly negative potential and be a porous metal catalytic to the reduction of ammonia, such as molybdenum or iron. At this point, the nitrogen gas will be adsorbed to the surface of the metal, split and combined with three protons to form ammonia, then being collected downstream in a continuous flow.

The first two electrodes can be fashioned from np-NiPt, of which we have extensive knowledge. Considerable research has been devoted to these electrochemical reactions for other applications, leading to other more suitable catalysts that may be used in the future. The final electrode used to reduce nitrogen will be a transition metal, such as iron or molybdenum, which have been shown to display increased activities[10]. With the use of liquid metal dealloying, the ability to form nanoporous materials of these elements with the high surface area-to-volume ratio desired in catalysis is now possible.

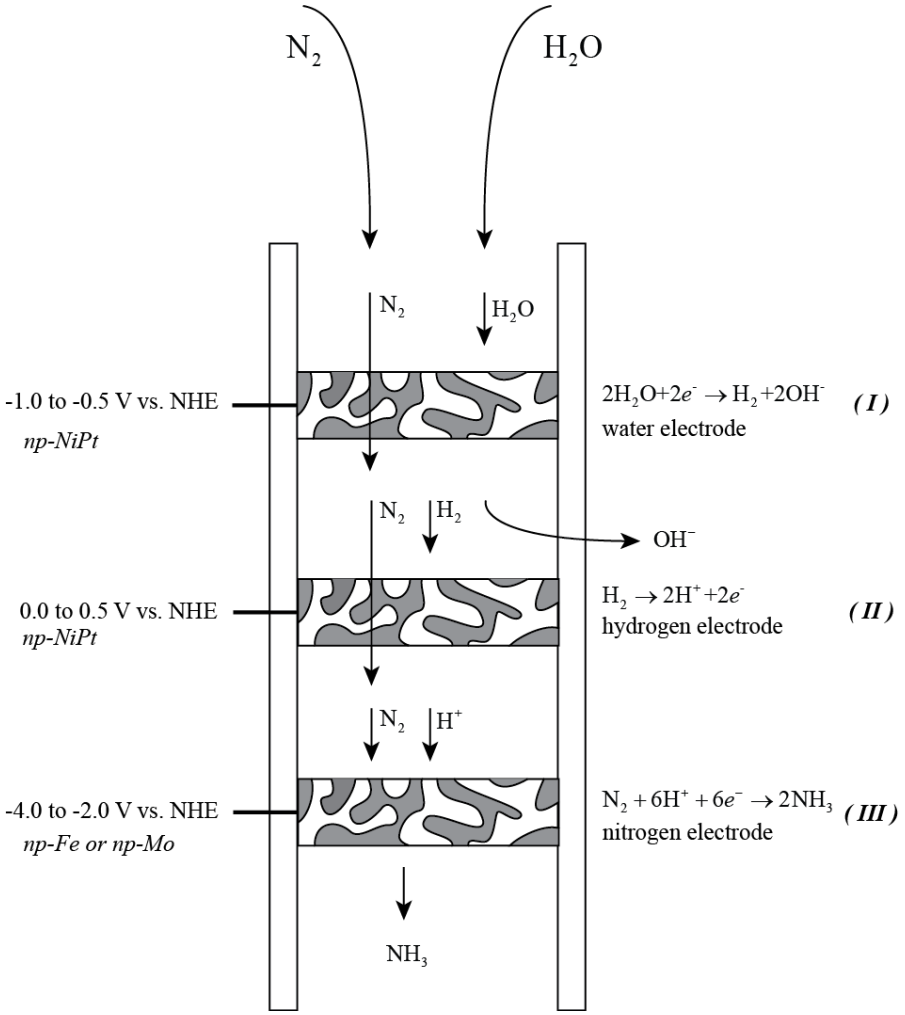

Figure 4.2. Generalized schematic detailing flow reactor for ammonia synthesis. Electrode I reduces water forming H_2 and OH^-, the latter of which is then removed. Electrode II oxidizes the H_2 product from Electrode I, resulting in H^+ which are subsequently reacted at Electrode III with N_2 to form NH_3 as the product.

This scheme has the advantage of operation at or close to ambient conditions. There is no need to apply significant pressures in excess of that require to flow the electrolyte, and temperatures may be raised slightly to increase the conductivity of the ionic liquid used, but should remain below 100 ˚C if using water as a reactant. This should greatly reduce the amount of energy required in the system, negating some of the losses due to overpotentials necessary to reduce nitrogen.

A fundamental study examining hydrogen oxidation (HOR) and hydrogen evolution (HER) in this system will be helpful to understand controlling the fluxes of protons, without the complication of nitrogen reduction. By feeding in hydrogen gas and then splitting the gas into protons (HOR) at the first electrode, such as,

$$H_2 \rightarrow 2H^+ + 2e^- \tag{4.2}$$

and then recombining them (HER) at the second,

$$2H^+ + 2e^- \rightarrow H_2 \tag{4.3}$$

. This also allows for understanding the impact of parameters such as flow rate, working distance between electrodes, temperature and so forth.

4.3 Experimental Methods

4.3.1 Electrolyte Selection

Using an ionic liquid as an electrolyte introduces a number of variables to consider (viscosity and flow behavior, conductivity and increased overall resistance, etc.). So as to more simply prove the concept using an HOR-HER sequential electrode couple, we first performed experiments in a simplified flow cell using aqueous solutions of varying pH to alter the background proton concentration. Two independent potentiostats were used for all electrochemical measurements (Gamry Reference 3000 and Gamry Interface 1000), using electrolytes of 0.25 M Na_2SO_4, buffered to the appropriate pH using 0.25 M H_2SO_4 and 0.25 M NaOH that were continuously recycled.

Ultimately, since an ionic liquid as an electrolyte will be necessary for nitrogen reduction, we explored the substantial list of criteria for any possible electrolyte, including the following:

1. *Large Electrochemical Stability Window* – Since we expect to apply significantly negative overpotentials to our catalysts in order to break nitrogen's triple bond, this means first and foremost any electrolyte must be stable at such potentials without breaking down. Fortunately, much research has been devoted to studying the electrochemical window of ILs, specifically for use with lithium ion batteries, which require stability conditions even greater than that expected for nitrogen reduction.
2. *Aprotic* – We believe by employing an aprotic IL, we can hopefully minimize the travel of protons within the electrolyte, in an effort to prevent any reactions from occurring in solution prior to reaching the next electrode.
3. *High conductivity* – In order to prevent resistance losses in electrolyte, any IL used must have an effective conductivity.
4. *Water solubility* – Eventually, we want some water solubility (for use as a reactant in the final scheme) but water content can complicate the issue when determining initial conditions/parameters. Ideally, we would use an IL that can be effectively dried during this initial stage of testing, before controlling the water content for later trials.

5. *Cost effective* – Many ILs are rather expensive, but often only used miniscule quantities (a few microliters at a time). However, for use as an electrolyte, even on a laboratory scale, we will require at least 100 ml of solution, and a considerable amount more for any industrial purposes. Even with recycling the electrolyte, a relatively inexpensive and simple synthesis is a must.

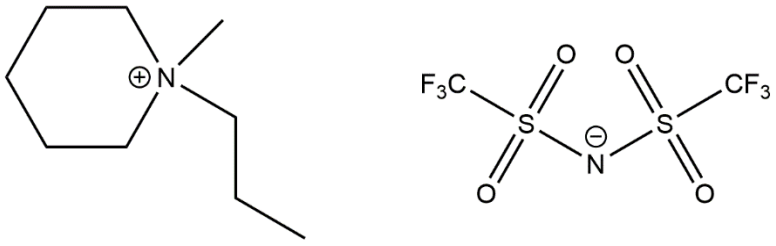

Figure 4.3. Schematic illustration of chemical structure of ionic liquid [PP13][Tf2N] (*N*-methyl-*N*-propylpiperidinium bis(trifluoromethanesulfonyl)imide).

Meeting all of these criteria, the ionic liquid [PP13][Tf2N] (full chemical name and structure shown in Figure 4.3) was chosen as an electrolyte. This has an electrochemical stability as low as -3.5 V vs the reversible hydrogen electrode (RHE), having one of the largest electrochemical windows relative to most ILs[16], as well as considered to be aprotic, helpful in limiting unwanted proton transport. By raising the temperature of

[PP13][Tf2N] slightly from room temperature, even just to 40 ˚C, there is a significant drop in the resistance as shown in Figure 4.4, theoretically making it suitable for use as an electrolyte.

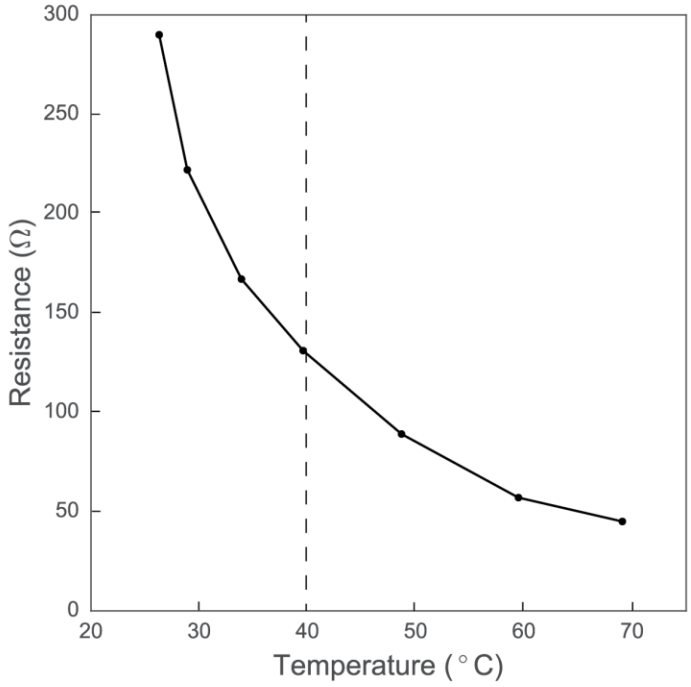

Figure 4.4. Resistance versus temperature for [PP13][Tf2N]. Measured using a Mettler Toledo SevenExcellence Conductivity Probe InLab731 ISM.

To synthesize [PP13][Tf2N], a procedure similar to that outlined by Xu et al.[16] was followed. Briefly, aqueous solutions of equimolar amounts of Li-[Tf2N] (bis(trifluoromethane)sulfonamide lithium salt, Sigma Aldrich, 99.95%) and [PP13]-Br were combined and stirred for a minimum of 12 hours, before the resulting IL was washed with DI water numerous times and dried under reduced atmosphere at 80 ˚C. [PP13]-Br was prepared using 243 ml of N-methylpiperidine (Sigma Aldrich, 99%) in

acetonitrile (Sigma Aldrich, 99.9%) at 70 ˚C. Slowly, 201 ml of 1-bromopropane (Sigma Aldrich, 99%), a slight molar excess, was added and allowed to stir for 24 hours. A resulting white powder precipitated from a yellow liquid that was washed with acetonitrile and crashed out of solution with ethyl acetate (Fisher Scientific, HPLC Grade). The white powder ([PP13]-Br) was dried under reduced pressure at 80 ˚C before use in synthesizing the IL. This reasonably simple procedure allowed large quantities (~300 ml) of [PP13][Tf2N] to be formed with comparatively inexpensive precursors.

Even after drying in a vacuum oven at elevated temperatures and reduced pressures for several days, there was a residual water content in the IL of approximately 250 ppm, measured using Karl Fisher Titration (Mettler Toledo Coulometric KF Titrator C20), as common with most ionic liquids. To further dry [PP13][Tf2N], we employed a protocol adapted from Islam et al.[17], to electrochemically reduce any residual water while under vacuum. Simply, using a power supply (GW Laboratory DC Power Supply) with a Pt wire and graphite rod, applying a potential of 2.0 V, any remaining water was electrolyzed. After ~12 hours, the water concentrations dropped below the sensitivity of our KF Titrator, suggesting we are well below 25 ppm of residual water in the IL, adequate for our purposes.

4.3.3 Flow Cell Designs

A simple channel flow cell was constructed from poly(methyl methacrylate) sheets with a polydimethylsiloxane (PDMS) spacer. Two working electrodes we constructed from NiPt foils (0.1 mm thick by 5 mm wide, spaced approximately 2 mm apart). The

foils had an initial composition of $Ni_{77}Pt_{23}$, that were dealloyed by the same protocols previously mentioned (i.e. cycling the potential in dilute sulfuric acid) prior to any electrochemical experiments. Downstream from the two working electrodes are two counter electrodes made from Pt wire, followed by two pseudo-reference electrodes constructed of Ag foils, a schematic of which is shown in Figure 4.5 (a). Flow in the cell was controlled with the use of a peristaltic pump (Fisher Scientific) an image detailing the experimental setup seen in Figure 4.5 (b).

(a)

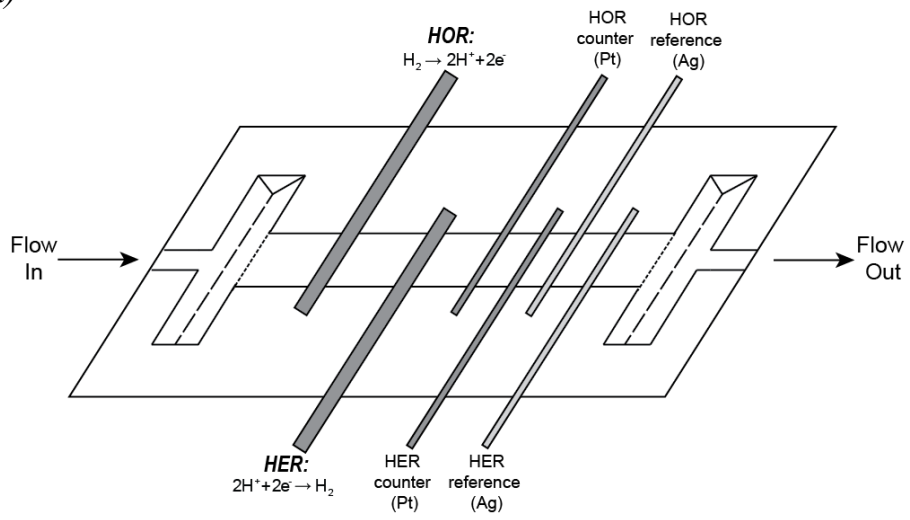

(b)

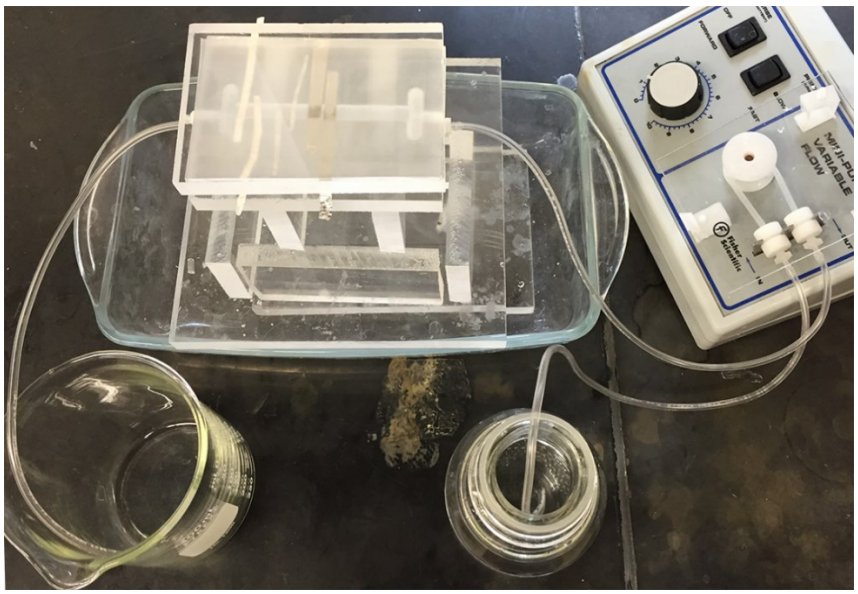

Figure 4.5. Flow cell employed for use with aqueous electrolytes. *(a)* Schematic representation of flow cell, detailing working electrodes constructed from np-NiPt foils, followed by their respective counter electrodes of Pt foils, and lastly the pseudo-reference electrodes of Ag foil. *(b)* Image of experimental setup with electrolyte being pumped through the cell by use of a peristaltic pump into a waste beaker.

While liquid was flowed through the cell, the second np-NiPt electrode was held at a constant -0.8 V vs. Ag (HER potential), while the first electrode was stepped sequentially from -1.0 V to 0.0 V vs. Ag (moving from HER to HOR potentials) to observe the current produced at the second electrode as a result of voltage applied to the first electrode.

However, when performing initial tests with this flow cell design, it was clear we were not effectively using the bulk of the catalyst. With flow perpendicular to the porosity, the increased surface area dealloying provided was not being used to its full advantage. To truly exploit these dealloyed electrodes offer, the ideal configuration would use the entire depth of the porosity, such as a filter where the electrolyte is forced to travel through the catalyst as it were a porous frit. Doing so would require much larger

pore sizes than the ~4 nm typically observed with np-NiPt, but these samples could be thermally coarsened to reach the desired pore size.

So as to test this configuration, we assembled a new flow through cell, substituting Pt meshes (52 mesh gauze, Sigma Aldrich, 99.9%) cut into 1.5 cm by 1.5 cm sections, attached with a Pt wire for electrical contact for the eventual porous metal electrodes for HOR and HER. A schematic rendering of the flow cell is shown in Figure 4.6 (a), with an image of the actual cell used in (b). A bi-potentiostat (Metrohm PGSTAT302N-BA) was used for all electrochemical measurements, negating the need for separate counter and reference electrodes for each working electrode. The counter electrode was a Pt mesh and the pseudo-reference constructed from a Ag mesh (50 mesh gauze, Alfa Aesar) in the same manner as both working electrodes.

When using the IL at elevated temperatures, a more complicated experimental setup is necessary to effectively heat the electrolyte, shown representatively in Figure 4.6 (c). First, we preheat the IL in a water bath set to 40 ˚C while saturating the electrolyte with nitrogen and/or hydrogen gas. Then, with the use of a peristaltic pump, the IL flows from the reservoir into an oven set to 40 ˚C, travelling in the tubing through a secondary water bath (for better heat transfer) before entering the flow cell. The IL exits the oven through a recycle stream, returning the electrolyte to the original reservoir.

(a)

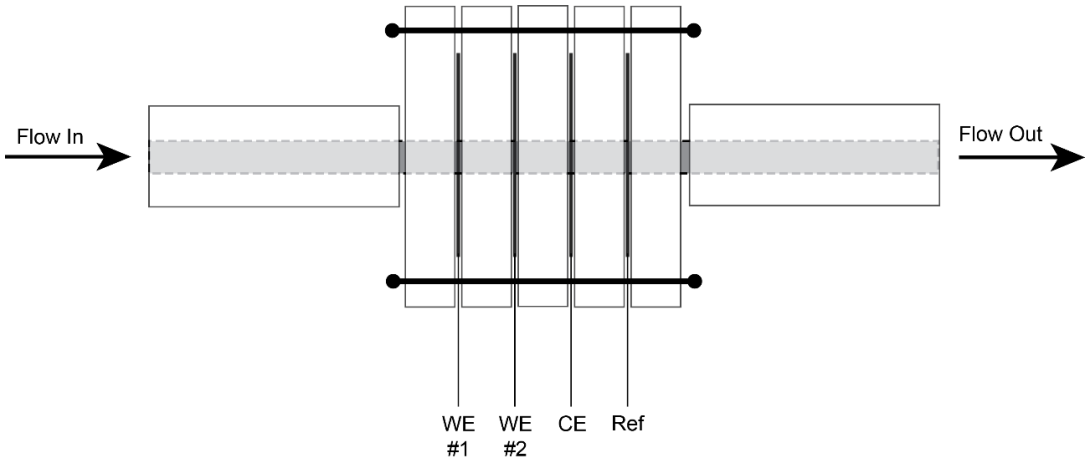

(b)

(c)

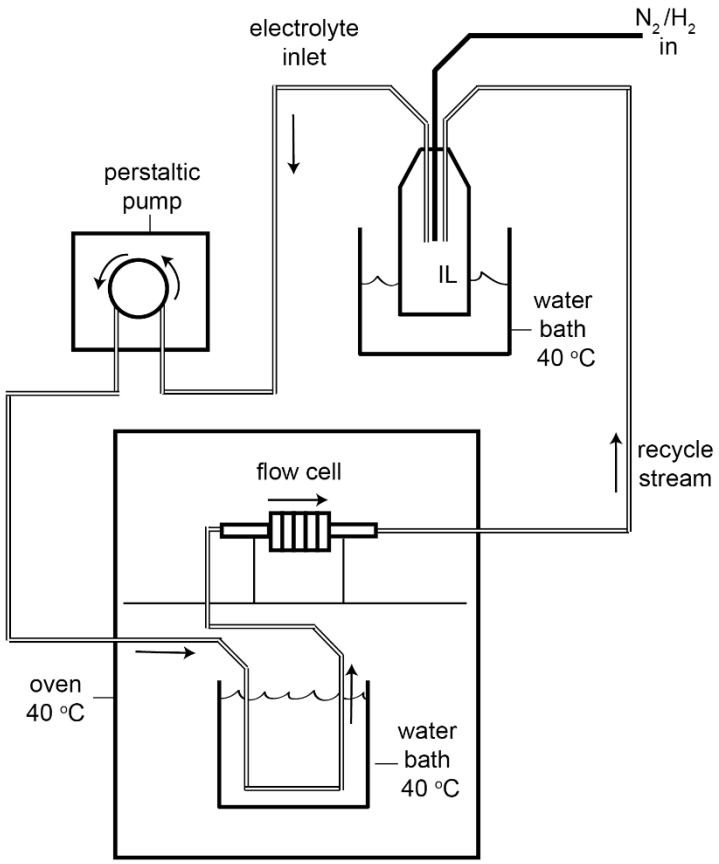

Figure 4.6. Design for flow through reactor. *(a)* Schematic cartoon of flow cell with an image *(b)* of the apparatus. *(c)* Schematic showing system designed to effectively heat IL throughout experiments.

4.4 Results and Discussion

4.4.1 Aqueous Solutions

Before any other experiments, we determined the potential regimes for HER and HOR by performing cyclic voltammetry (CV) on a np-NiPt disk in an RDE setup in pH 3 and pH 5 electrolytes, using a Ag wire as a pseudo-reference electrode, as shown in Figure 4.7. This allows us to determine the appropriate potentials to apply to each electrode to control the concentration of products. From Fig. 4.7, we can see hydrogen oxidation turns on just above -0.75 V vs Ag, dictated by the sharp rise in the current for hydrogen saturated electrolytes. There is a noticeable increase in this regime in the deaerated electrolyte as well, due to H_{upd} on the high surface area np-NiPt catalyst. If we continue sweeping the potential above -0.25 V vs Ag, we will begin to oxidize the Pt surface. Below -0.75 V vs Ag, there is a plateau at very different magnitudes of the current density for pH 5 versus the pH 3 solution, due to the background concentration of protons in each. Between -1.0 V and -0.75 V vs Ag, we are within the HER regime, meaning any protons in solution will react to evolve hydrogen. A pH 5 electrolyte is effectively neutral so there will be little to no hydrogen evolution observed. When compared with a pH 3 solution, where the proton concentration is roughly 1 mM, the magnitude of this value is increased due to hydrogen evolving at a constant rate. Below -1.0 V vs Ag, there is a sharp decline in the current density indicating the reduction of water below his potential.

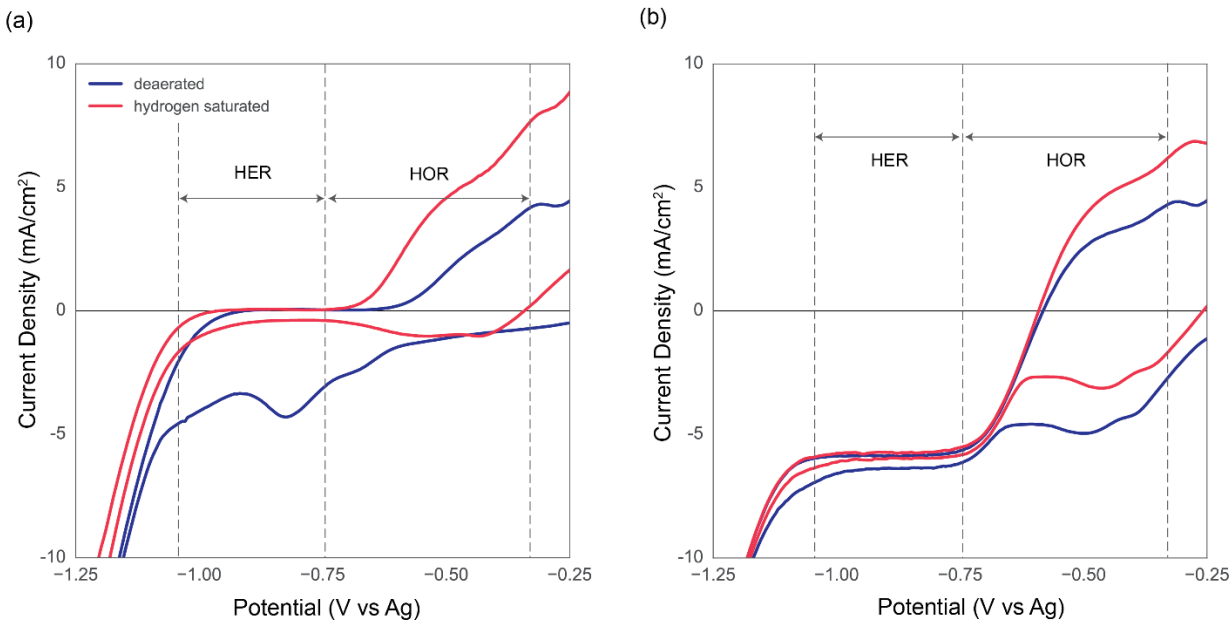

Figure 4.7. Cyclic voltammetry at sweep rate of 50 mV/s performed using a np-NiPt disk with a rotating disk electrode at 800 rpm using a Ag foil pseudo-reference electrode in deaerated *(blue)* or hydrogen saturated *(red)* electrolytes of 0.25 M Na_2SO_4 buffered with 0.25 M H_2SO_4 and 0.25 M NaOH to (a) pH 5 and (b) pH 3.

To test the HOR-HER electrode couple, we started by holding the second potential safely within the HER regime (-0.8 V vs Ag), so any protons will readily react, producing a negative current. Then we apply a potential at the first electrode below the onset of HOR (i.e. no protons are formed), therefore any current observed on the second electrode should be minimal and associated only with the background concentration of protons in solution due to the pH. As we sweep the potential more positively, H_2 that is added to the electrolyte upstream will begin to oxidize, generating protons which travel to the second electrode where they are reduced back to H_2. As the potential is increase further into the

HOR regime, the formation of protons becomes diffusion-limited, leading to a plateau in current seen for both working electrodes. The results of this are shown in Figure 4.8.

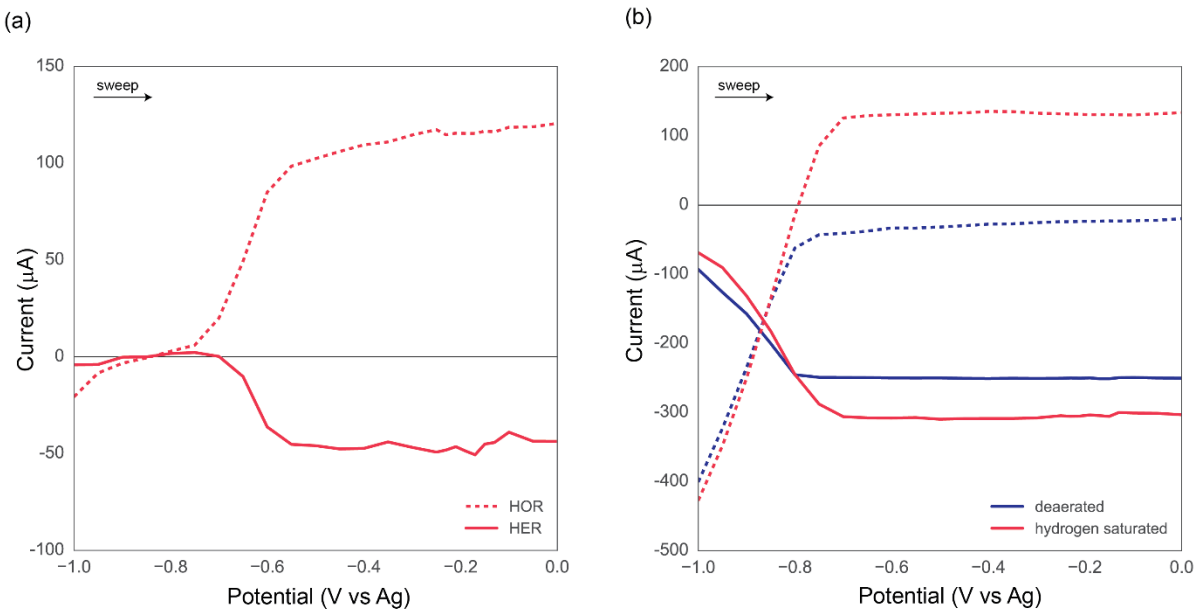

Figure 4.8. Sequential electrode HOR-HER in aqueous solutions of 0.25 M Na_2SO_4, buffered to desired pH using 0.25 M H_2SO_4 and 0.25 NaOH. Currents associated with the second electrode (HER) plotted versus potential applied to the first electrode (HOR) in (a) hydrogen saturated solution of pH 5 (b) deaerated *(blue)* and hydrogen saturated *(red)* solutions of pH 3. Experiments conducted in the channel flow cell, measured potentiostatically with intervals set 50 mV apart, holding each for 60 seconds.

When using pH 5 electrolyte, the deaerated solution was effectively zero and hence not plotted, but a clear diffusion-limited plateau appears for hydrogen saturated solutions at approximately -50 μA. This is the same value seen in pH 3 after subtracting the background concentration of protons (seen in the deaerated sample) from the hydrogen saturated sample. These results definitively show the concept of sequential electrodes to

generate reactants as desired is effective for simple oxidation/reduction reactions in aqueous solutions.

4.4.2 Ionic Liquid Electrolyte

Upon switching to the IL [PP13][Tf2N] as our electrolyte, similar tests to determine potential limits for the varying hydrogen regimes using a Ag reference were necessary, as illustrated in Figure 4.9. At this point, the flow cell used was also changed to incorporate the flow through model described in Figure 4.6. In hydrogen saturated [PP13][Tf2N], above approximately 0.2 V vs Ag, there is a very clear positive oxidation current measured associated with HOR, below this value, HER is expected.

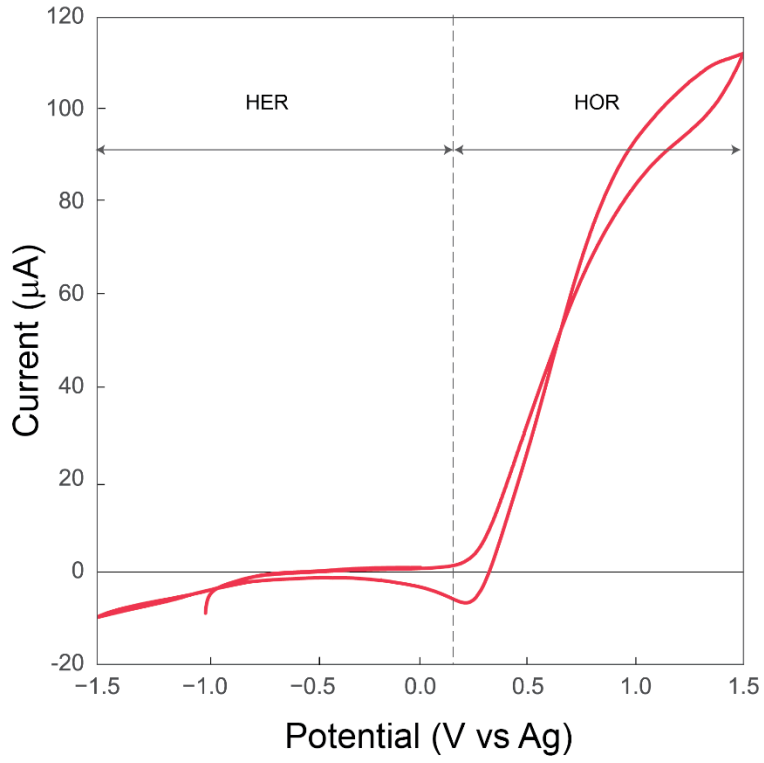

Figure 4.9. Cyclic voltammetry performed in the ionic liquid [PP13][Tf2N], saturated with H_2 at a sweep rate of 5 mV/s, using a Pt mesh working electrode measured against a Ag mesh pseudo-reference electrode.

After establishing the potential regimes, similar experiments to those in aqueous solution were performed in the new flow cell, as depicted in Figure 4.10, for both hydrogen saturated and deaerated solutions. Current in the deaerated IL is effectively zero at all potentials, acting as the inert control. Upon sweeping the potential of the first electrode toward positive potentials, there is a clear and distinct turn-on for HOR at approximately 0.4 V vs Ag that is mirrored in the onset of HER at the second electrode.

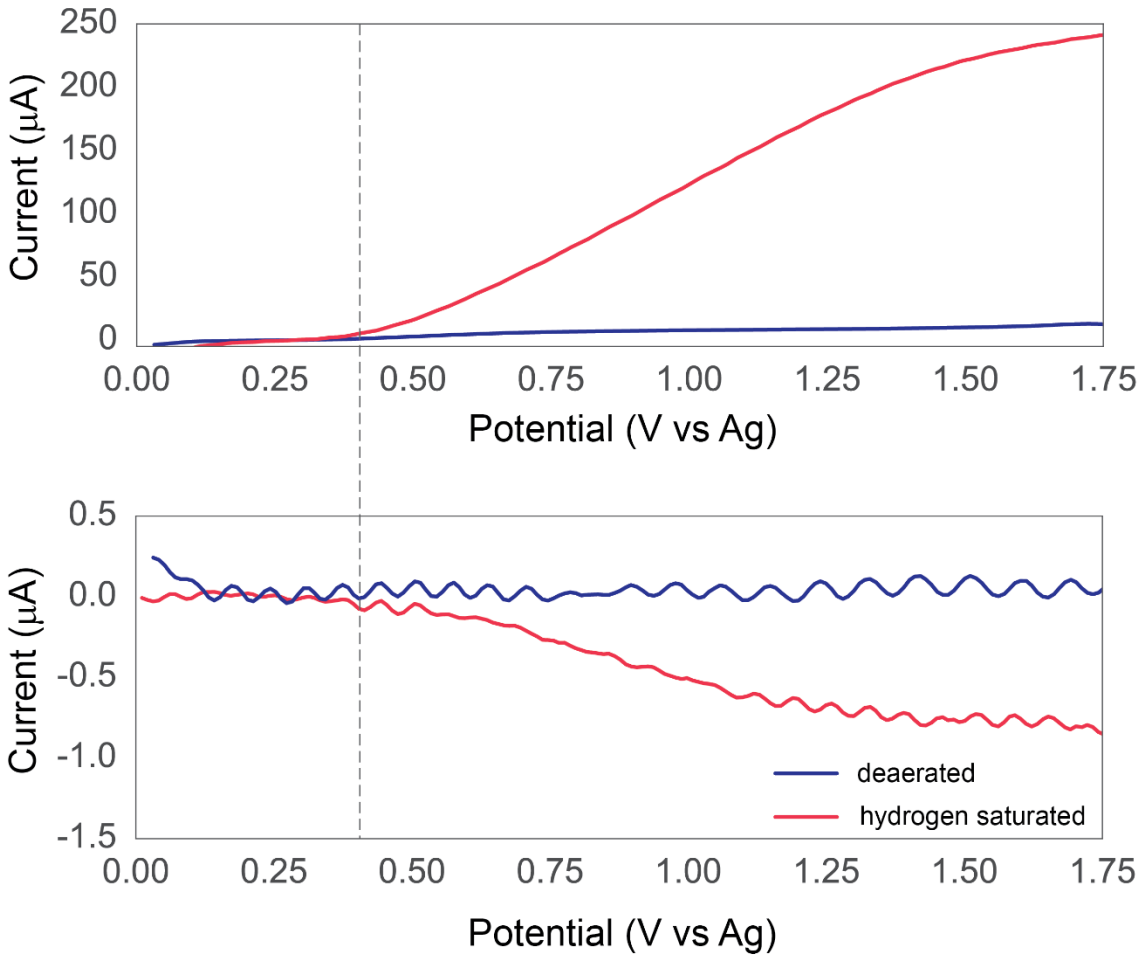

Figure 4.10. Sequential electrode HOR-HER in [PP13][Tf2N] at 40 ˚C under deaerated *(blue)* and hydrogen saturated *(red)* conditions using the flow through cell, taken at a sweep rate of 2.5 mV/s. The top graph depicts the current of the first electrode (HOR)

plotted against potential, while the bottom represents the current measured at the second electrode (HER) versus the potential applied to the first. The HER electrode is held at a constant potential of -1.0 V vs Ag during the entirety of the experiment.

Comparing the values measured in IL (Fig 4.10) versus those measured in aqueous electrolytes (Fig 4.8), it is apparent that the relatively magnitude of the current measured at the second electrode compared to the first is significantly reduced in the IL system. The HOR current for both electrolytes is approximately 200 μA, however the maximum HER current drops from 50 μA in aqueous solution to less than 1 μA in IL. It is unlikely due to hydrogen solubility differences, since that would be noticed in the value of the first electrode's current, nor the difference between sweeping the potential as opposed to potentiostatic measurements resulting in such a drastic discrepancy. While the use of meshes as electrode materials can be improved upon by incorporating porous metals with increased surface areas and catalytically active sites, it is our hypothesis that the aprotic nature of the IL is in fact limiting the transport of protons from one electrode to the next, ultimately suggesting we re-examine the criteria suggested for an ideal electrolyte. Instead of stymieing proton transport only between electrodes, it is possible the proticity of [PP13][Tf2N] disrupts transport altogether.

Another variable to consider is the difficulty associated with determining the true onset of the HER regime by with one electrode. Since there is no proton source like that seen in a pH 3 electrolyte, by measuring the CV of a hydrogen saturated electrolyte, there is no assurance of the true limits of the HER regime. Rather, the potential initially chosen for the second electrode may still be in a kinetically controlled portion of the curve, implying much larger overpotential may be required to drive the reaction. The second

potential was held to -1.5 V vs Ag (a 0.5 V increase in overpotential from the previous experiment) in an effort to further examine this parameter, plotted in Figure 4.11.

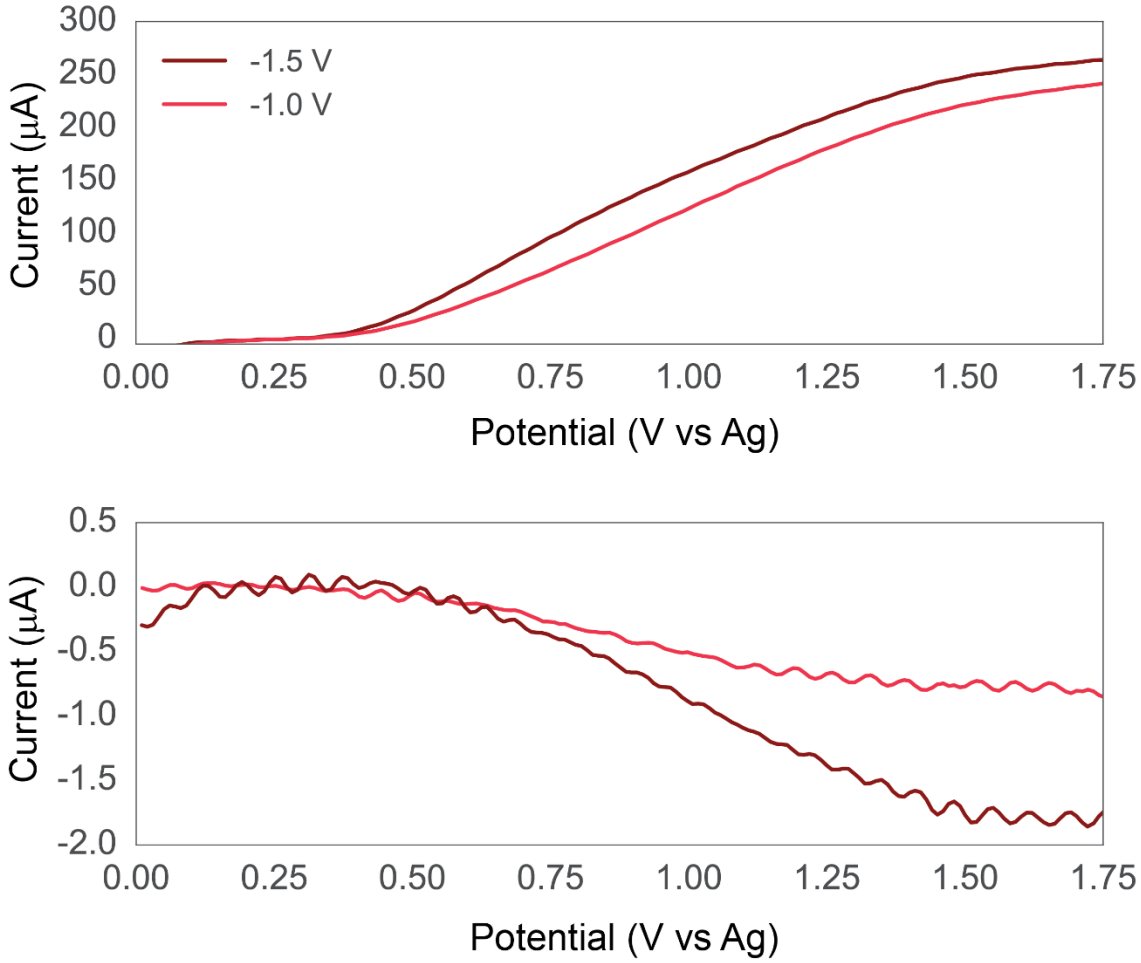

Figure 4.11. Sequential electrode HOR-HER in [PP13][Tf2N] at 40 ˚C under hydrogen saturated conditions using the flow through cell, taken at a sweep rate of 2.5 mV/s for an HER set potential of -1.0 V vs Ag *(red)* versus -1.5 V vs Ag *(dark red)*. The top graph depicts the current of the first electrode (HOR) plotted against potential, while the bottom represents the current measured at the second electrode (HER) versus the potential applied to the first.

As expected, a higher overpotential results in a higher magnitude current, but still significantly below the values obtained in aqueous solution. Other variables may improve the performance, one in particular that is considerably different relative to the aqueous

solution is the working distance between the two electrodes. In the flow cell model, the foils were placed as close together as possible without touching, approximately a millimeter or two apart. However, in the case of the flow through model, intrinsic with the design of the cell, the electrodes are spaced over 0.25 in apart, more than 5 times the distance than the foils. This increase in distance can drastically reduce the efficiency of the second electrode, analogous to the geometric constraints in a rotating ring disk electrode (RRDE) apparatus.

Additionally, the working temperature is a parameter that should be investigated in greater detail, attacking the problem by decreasing the resistance while simultaneously having the ability to improve the reaction kinetics. While 40 ˚C is sufficient to reduce the resistance to a degree, it is still orders of magnitude greater than most aqueous electrolytes[18]. There is still room to further increase the temperature, however there is a limitation of the materials currently used to construct the cell. Polycarbonate becomes very prone to cracking and fracture when the working temperature is above 40 ˚C, even though the reported stability is well above 100 ˚C[19]. There are many other plastics that have high thermal and chemical stability of which the cell could be constructed, and should be considered in future work.

4.4.3 Preliminary Results for Ammonia Synthesis

Although there is substantial optimization of the flow through cell still absent, preliminary nitrogen reduction was attempted, illustrated in Figure 4.12. The [PP13][Tf2N] electrolyte was simultaneously saturated with both nitrogen and hydrogen

gases, using Pt meshes for both working electrodes. Pt may act as a catalyst for nitrogen reduction, but possibly will require larger overpotentials than other materials such as molybdenum. The first electrode is held at 1.5 V vs Ag (in the HOR regime) for the entirety of the experiment, producing a constant stream of protons flowing to the second electrode, where the potential is swept negatively starting at 0.0 V vs Ag.

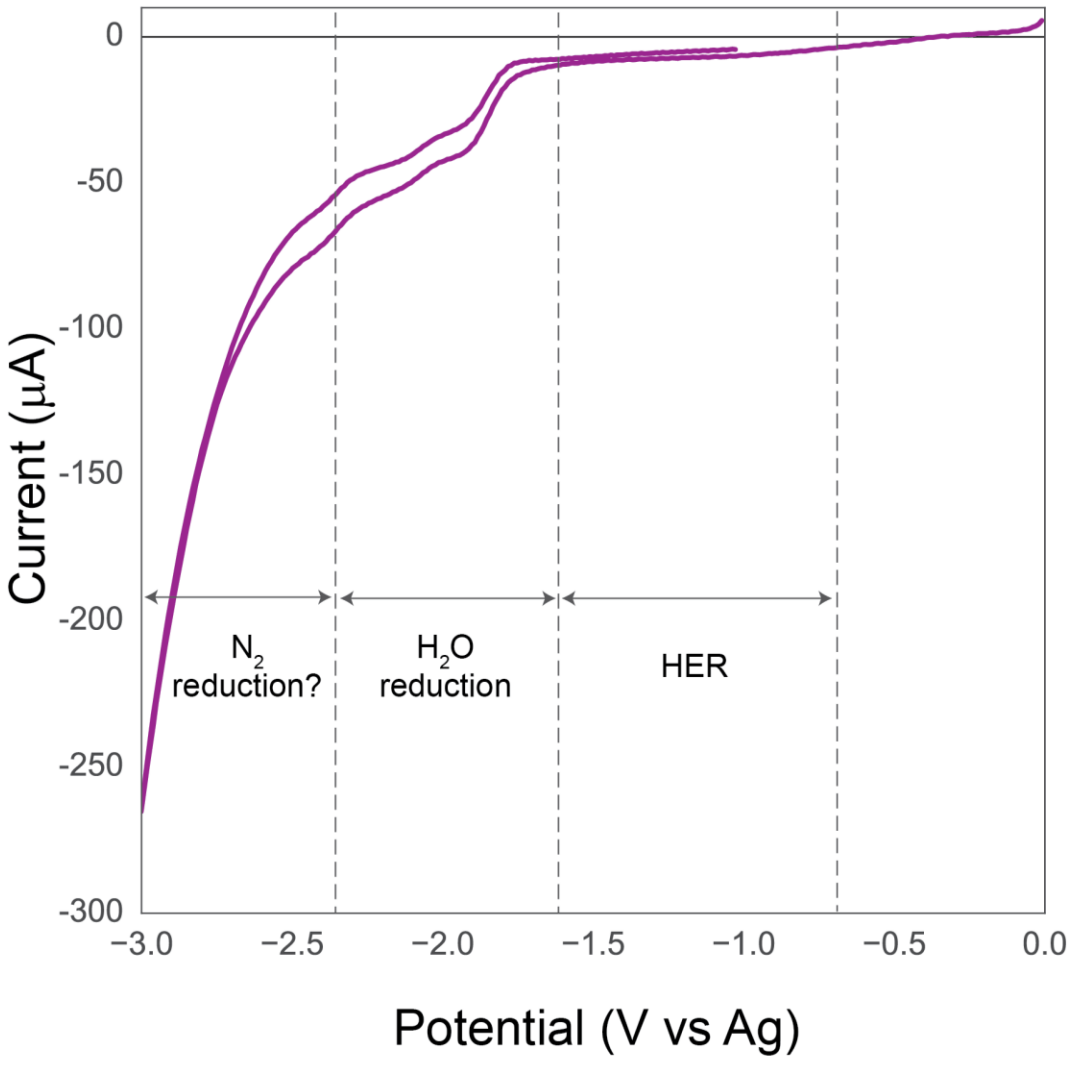

Figure 4.12. Preliminary current measured at second Pt electrode as its potential is swept more negatively at a rate of 2.5 mV/s in [PP13][Tf2N] saturated with both nitrogen and hydrogen gases. The first Pt electrode is held at a constant HOR potential of 1.5 V vs Ag for the entirety of the experiment.

There is a slight reductive current from -0.5 V to -1.6 V vs Ag, associated with HER, followed immediately by a steep reduction likely due to water dissociation. Since our water content is relatively low (below 50 ppm), this current should diminish over time without a source for it to be replenished. Below -2.0 V vs Ag, there is a more reductive curve at substantial currents considering the not optimized configuration employed, an encouraging result that is potentially due to the reduction of nitrogen. It appears distinct from peaks associated with water reduction. An alternative would be the degradation of the IL itself, however that would result in a distinct color change which was not observed, implying nitrogen reduction is a logical conclusion. Further tests to confirm the presence of ammonia would need to be performed to conclusively establish this outcome.

4.5 Conclusions

We successfully demonstrated the control of reactant concentrations using a novel flow cell geometry employing sequential electrodes, observing the behavior of hydrogen oxidation and evolution reactions. Initial designs performed these reactions in a channel flow cell in aqueous solutions, and then later adapted to using ionic liquids as the electrolyte to improve the electrochemical window necessary for nitrogen reduction. Preliminary results are optimistic that this scheme will allow for the electrochemical synthesis of ammonia.

References

1. Mineral Commodity Summaries. *U.S. Geol. Surv.*

2. Erisman, J. W., Sutton, M. a., Galloway, J., Klimont, Z. & Winiwarter, W. How a century of ammonia synthesis changed the world. *Nat. Geosci.* **1,** 636–639 (2008).

3. Stewart, W. M. & Roberts, T. L. Food security and the role of fertilizer in supporting it. *Procedia Eng.* **46,** 76–82 (2012).

4. Amar, I. a., Lan, R., Petit, C. T. G. & Tao, S. Solid-state electrochemical synthesis of ammonia: A review. *J. Solid State Electrochem.* **15,** 1845–1860 (2011).

5. Nice, K. How Fuel Processors Work. *How Stuff Works* (2000).

6. Smil, V. *Enriching the Earth: Fritz Haber, Carl Bosch, and the Transformation of World Food Production*. (The MIT Press, 2004).

7. Platt, K. Industrial Natural Gas Demand. in *Energy Information Administration - ASA Committee on Energy Statistics*

8. Matanović, I., Garzon, F. H. & Henson, N. J. Electro-reduction of nitrogen on molybdenum nitride: structure, energetics, and vibrational spectra from DFT. *Phys. Chem. Chem. Phys.* **16,** 3014–3026 (2014).

9. Rod, T. H., Logadottir, A. & Nørskov, J. K. Ammonia synthesis at low temperatures. *J. Chem. Phys.* **112,** 5343–5347 (2000).

10. Skúlason, E. *et al.* A theoretical evaluation of possible transition metal electro-catalysts for N2 reduction. *Phys. Chem. Chem. Phys.* **14,** 1235 (2012).

11. Honkala, K. *et al.* Ammonia Synthesis from First-Principles Calculations. *Science*

(80-.). **307,** 555–558 (2005).

12. Yandulov, D. V. & Schrock, R. R. Catalytic Reduction of Dinitrogen to Ammonia at a Single Molybdenum Center. *Science (80-.).* **301,** 76–78 (2003).

13. Marnellos, G. & Stoukides, M. Ammonia Synthesis at Atmospheric Pressure. *Science (80-.).* **282,** 98–100 (1998).

14. Kordali, V., Kyriacou, G. & Lambrou, C. Electrochemical synthesis of ammonia at atmospheric pressure and low temperature in a solid polymer electrolyte cell. *Chem. Commun.* 1673–1674 (2000). doi:10.1039/b004885m

15. Murakami, T., Nohira, T., Goto, T., Ogata, Y. H. & Ito, Y. Electrolytic ammonia synthesis from water and nitrogen gas in molten salt under atmospheric pressure. *Electrochim. Acta* **50,** 5423–5426 (2005).

16. Xu, J., Yang, J., NuLi, Y., Wang, J. & Zhang, Z. Additive-containing ionic liquid electrolytes for secondary lithium battery. *J. Power Sources* **160,** 621–626 (2006).

17. Islam, M. M., Okajima, T., Kojima, S. & Ohsaka, T. Water electrolysis: an excellent approach for the removal of water from ionic liquids. *Chem. Commun. (Camb).* 5330–5332 (2008). doi:10.1039/b811174j

18. *CRC Handbook of Chemistry and Physics*. (CRC Press, 1989).

19. Carraher, Jr., C. E. *Seymour/Carraher's Polymer Chemistry*. (CRC Press, 2008).

Chapter 5: Conclusions and Future Directions

By employing nanoporous metals, particularly np-NiPt, we have presented in this dissertation a variety of catalytic applications for dealloyed materials that actively use the porosity intrinsic to these metals. From understanding the fundamentals of porosity evolution and how best to exploit these properties for use as electrocatalysts for fuel cell applications, we have developed experimental procedures for their future application in the reduction of other small molecules, such as carbon dioxide and nitrogen.

Elaborating on prior research that employed ionic liquids, we determined the key the properties to further enhance oxygen reduction activity for use in PEM fuel cells. After the analysis of several physical properties of ILs, such as viscosity, oxygen and water solubility, and conductivity, we confirmed oxygen solubility is crucial in reducing the necessary overpotential to drive ORR, but the greatest reduction activity correlates to those materials that combine high oxygen solubility with low water solubility. By forcing reactants to the catalyst interface and products away, in accordance with Le Chatelier's principle, we drive the reaction in our favor, increasing overall activity. While all of the ILs we sampled saw no significant improvement over [MTBD][beti] in ORR activity, we clarified the parameters of interest when assaying potential new materials.

Building off the transport phenomena investigated with ILs, we investigated the oxygen reduction reaction under the unusual conditions of being proton diffusion-limited. By doing so, we are able to not only suppress hydrogen evolution by hundreds of

millivolts, but also produce diffusion selective catalysts. This impacts not only the activity of the catalyst but also its selectivity by varying electrolytes. However, there is more clarification that is necessary, primarily to answer the question: is it a factor of buffering capacity of the electrolyte or is adsorption kinetics that impact the selectivity? Our results were limited to the two most common electrolytes for acidic ORR measurements, where both perchloric and sulfuric acids are classified as strong acids. But these are not by any means, an exhaustive list. By comparing additional electrolytes, primarily investigating weak acids that by definition act as stronger buffers, as well as the impact of the concentration of the solution, should elucidate these details. An assessment of a planar versus nanoporous electrode would be desirable, but to be a direct comparison, one should use a NiPt sample with the same final composition as np-NiPt, ideally annealed under vacuum to segregate Pt to the surface, forming a skin similar to that found in a dealloyed sample.

While the technological impact for proton diffusion limited oxygen reduction is minimal, this technique holds great promise for other electroreduction reactions, of particular interest being CO_2 reduction. Implementation requires the selection of a proper nanoporous catalysts ideal for CO_2 reduction since the np-NiPt is far more active for hydrogen evolution in the necessary regime. Au and Ag are possible catalysts for reducing CO_2 to CO, which in the proper ratio with H_2 can form the useful product syngas. Perhaps most interesting would be to use nanoporous Cu due to its unique selectivity towards producing hydrocarbons. This one of the most desired products, but CO_2 reduction with Cu catalysts occurs at low rates, partially due to competition with HER[1,2].

As opposed to relying on secondary materials or pH variations to control transport phenomena, we developed and successfully demonstrated the concept of sequential electrodes to form reactants in the desired concentrations in both aqueous solutions and ionic liquid electrolytes. By switching from a channel flow cell configuration to a flow through variation, the entirety of the porosity can be exploited with minimal interior space wasted. This still requires the development of coarsened dealloyed materials with sufficient length scales to allow the electrolyte to flow through each electrode to replace the metal meshes used in this work.

Optimization of the flow through cell was started, but as with any novel system, more improvements are necessary. One obstacle is establishing the ideal working temperature so as to increase conductivity, but also accounting for the limitations of the construction materials. Continuing with obstacles of the IL employed, a comparison with a protic IL as a counterpart to the aprotic [PP13][Tf2N] is a necessary control. The initial hypothesis that limiting the transport of protons in the electrolyte would be ideal to prevent side reactions should be reevaluated, considering the reduced currents see at the second electrode.

The ideal parameters for the cell itself need to be evaluated. Of critical importance is the distance the working electrodes are spaced apart. Compared to the previous model of the channel flow cell, this distance increased by a factor of five, which could account for some of the issues with diminished current values. Related to this variable is the flow rate of the electrolyte, which is much more difficult to control and accurately measure when using an IL over an aqueous solution. Normal flow meters are not calibrated for the

increased viscosity of ILs and as working temperature varies, so promptly does the viscosity making it difficult to manage with a peristaltic pump.

Lastly, we sought to eliminate water as effectively as possible from the reactant stream for simplicity, but the largest benefit would come from incorporating water as our proton source over hydrogen gas, eliminating the need for steam reforming. However, this requires an additional electrode to first reduce water to hydrogen and hydroxide prior to forming protons, along with studying the impact of hydroxide on the system (or how to remove or divert it). Theoretically, this should be minimal, if detected at all, but adds another layer of complexity to the problem.

References.

1. Mistry, H., Varela, A. S., Kühl, S., Strasser, P. & Cuenya, B. R. Nanostructured electrocatalysts with tunable activity and selectivity. *Nat. Rev. Mater.* 16009 (2016). doi:10.1038/natrevmats.2016.9

2. Tang, W. *et al.* The importance of surface morphology in controlling the selectivity of polycrystalline copper for CO_2 electroreduction. *Phys. Chem. Chem. Phys.* **14,** 76–81 (2012).

Curriculum Vitae

Education

Johns Hopkins University

Philosophical Doctorate in Materials Science and Engineering Fall 2016

Thesis: *Tuning the Reaction Kinetics at the Catalyst/Electrolyte Interface: A New Design Space in Electrocatalysis*

Master of Science in Materials Science and Engineering Spring 2015

Syracuse University

Bachelor of Science *Cum Laude* in Chemical Engineering Spring 2011

Research Experience

Johns Hopkins University 2011 – 2016

Graduate Research Assistant – Erlebacher Group

- Employed electrochemistry to study catalysis on metal nanostructures and composites
- Synthesized ionic liquids for impregnation in porous metals
- Fabricated and tested multiple flow cell apparatus to study electroreduction reactions

Syracuse University 2009-2011

Undergraduate Research Assistant – Mather Research Group

- Synthesized and characterized liquid crystalline elastomers with a focus on chemorheology
- Participated with UNAM in Cuernavaca, Mexico studying cure kinetics

Mentoring Experience

STEM Achievement in Baltimore Elementary Schools (SABES) Mentor 2015-2016

Aims to improve STEM education through a NSF-funded collaboration between Johns Hopkins University and Baltimore City Schools. Volunteered as a mentor to elementary school aged students to assist in scientific and engineering based projects

Undergraduate Senior Design Mentor, Johns Hopkins University 2014-2015

Hugo Uvegi, "Controlling Reactivity of Sequential Hydrogen Oxidation and Evolution with Porous Metal Catalysts"

NSF Research Experience for Undergraduates Mentor, Johns Hopkins University 2012

Olivia Hentz, "Gold Templated Hollow Polymer Vesicles for Drug Delivery"

Publications

McCue, I., **Benn, E.**, Gaskey, B., & Erlebacher, J. "Dealloying and Dealloyed Materials." *Annual Review of Materials Research*, **46,** 1-24 (2016).

Benn, E., Uvegi, H. & Erlebacher, J. "Characterization of Nanoporous Metal-Ionic Liquid Composites for the Electrochemical Oxygen Reduction Reaction." *J. Electrochem. Soc.* **162,** H759–H766 (2015).

Conferences & Presentations

"*" denotes and invited presentation. Presenting authors are underlined.

E. Benn, J. Erlebacher, "Oxygen Reduction in Nanoporous Metals Under Proton Diffusion Limited Conditions," Electrochemical Society Spring Meeting, San Diego, California, June 1, 2016.

E. Benn, J. Erlebacher, "Oxygen Reduction Under Proton Diffusion Limited Conditions," Environment, Energy, Sustainability and Health Institute 2016 Symposium, Baltimore, Maryland, April 6, 2016. [Poster]

*J. Erlebacher**, E. Benn,** H. Uvegi, "Controlling Electrocatalysis in Nanoporous Metals," Materials Research Society Fall Meeting, Boston, Massachusetts, November 30, 2015

E. Benn, H. Uvegi, J. Erlebacher, "Characterization of Nanoporous Metal/Ionic Liquid Composites for Oxygen Reduction," Materials Research Society Fall Meeting, Boston, Massachusetts, December 1, 2014.

E. Benn, H. Uvegi, J. Erlebacher, "Nanoporous Metal/Ionic Liquid Composites for Electrocatalysis," Symposium on Nanoporous Materials by Alloy Corrosion, Lake Bostal, Germany, September 28, 2014. [Poster]

*J. Erlebacher, **E. Benn**, I. McCue, "Control of the Interface Mobility during Dealloying: New Systems and New Materials," Materials Research Society Fall Meeting, Boston, Massachusetts, December 5, 2013.

E. Benn, J. Erlebacher, "Application of Flow Cell Apparatus to Characterize np-Metal/IL Composites for ORR," Materials Research Society Fall Meeting, Boston, Massachusetts, December 3, 2013.

E. Benn, I. McCue, J. Erlebacher, "Stabilizing Porous Structures with Ternary Alloys," Gordon Research Conference in Thin Film and Crystal Growth, Biddeford, Main, July 9, 2013. [Poster]